Titre: Title:	Synchronous Machine Modeling Precision and Efficiency in Electromagnetic Transients
Auteur: Author:	Ulas Karaagac
Date:	2011
Type:	Mémoire ou thèse / Dissertation or Thesis
Référence: Citation:	Karaagac, U. (2011). Synchronous Machine Modeling Precision and Efficiency in Electromagnetic Transients [Thèse de doctorat, École Polytechnique de Montréal]. PolyPublie. https://publications.polymtl.ca/692/

UNIVERSITÉ DE MONTRÉAL

SYNCHRONOUS MACHINE MODELING PRECISION AND EFFICIENCY IN ELECTROMAGNETIC TRANSIENTS

ULAS KARAAGAC
DÉPARTEMENT DE GÉNIE ÉLECTRIQUE
ÉCOLE POLYTECHNIQUE DE MONTRÉAL

THÈSE PRÉSENTÉE EN VUE DE L'OBTENTION
DU DIPLÔME DE PHILOSOPHIAE DOCTOR (Ph.D.)
(GÉNIE ÉLECTRIQUE)
NOVEMBRE 2011

UNIVERSITÉ DE MONTRÉAL

ÉCOLE POLYTECHNIQUE DE MONTRÉAL

Cette thèse intitulée

SYNCHRONOUS MACHINE MODELING PRECISION AND EFFICIENCY IN ELECTROMAGNETIC TRANSIENTS

présentée par : KARAAGAC Ulas
en vue de l'obtention du diplôme de : Philosophiae Doctor
a été dûment acceptée par le jury d'examen constitué de :

M. KOCAR Ilhan, Ph.D., président
M. MAHSEREDJIAN Jean, Ph.D., membre et directeur de recherche
M. GAGNON Richard, Ph.D., membre
M. LAGACÉ Pierre Jean, Ph.D., membre

ACKNOWLEDGEMENTS

I would like to express my deepest gratitude to my supervisor Prof. Jean Mahseredjian for his guidance, encouragement, patience, support and especially friendship. His innovative and questioning approach, his broad knowledge and his real life experience in Power Systems discipline helped me to establish a solid understanding and vision. I learned a lot from him about how to think different and to be creative. I think this is the most important asset that one can gain from a Ph.D. program.

Special thanks goes to colleagues working in Planning Department of Turkish Transmission Company for providing practical cases used in this study.

Greatest appreciation is reserved for my wife, Asli for her patience, support and encouragement.

Finally, I would like to express special thanks to my parents Yunus and Kezban for their endless love and support.

RÉSUMÉ

L'objectif principal de cette thèse est l'élaboration d'une méthode de modélisation de la machine synchrone plus performante et plus précise, et des algorithmes pour le calcul et la solution des transitoires électromagnétiques. Le pas d'intégration numérique est un facteur clef pour ces aspects. La possibilité d'utiliser des pas plus grands permet d'augmenter la vitesse des calculs et donc d'étendre le champ d'application des méthodes de type électromagnétique.

Cette thèse propose quatre modèles de façon à améliorer la précision du modèle dq0 classique tout en maintenant son efficacité. Trois de ces modèles utilisent le dq0 avec une précision accrue de la modélisation. Parmi les modèles précis se retrouve le dq0 avec des pas d'intégration intermédiaires. L'efficacité est maintenue par la restriction du modèle à l'usage durant des intervalles transitoires, là où la précision du modèle classique dq0 diminue. Ces modèles fournissent une modélisation précise tout en maintenant la vitesse du dq0 classique. Cependant, ils sont conçus spécialement pour les cas typiques d'étude de stabilité transitoire de réseau, et leur précision se détériore quand l'exactitude du modèle est nécessaire pour une grande partie de l'intervalle de simulation complète. Le meilleur modèle nommé PD-dq0 est obtenu en appliquant la transformation de ''Park'' aux équations discrétisées dans le domaine des phase.

Les études d'évaluation de la précision et de l'efficacité démontrent que le modèle PD-dq0 est supérieur aux autres modèles proposés dans la littérature.

L'analyse de précision est effectuée avec les contraintes de précision du réseau environnant. Donc, ce travail contribue également à une meilleure évaluation de la précision numérique et de l'efficacité des engins de simulation étudiés.

La thèse se termine par des analyses au niveau des méthodes d'implémentation des équations de machine synchrone dans les équations de réseau et des solveurs de matrices

creuses. Les analyses permettent de déduire des améliorations de performance numérique selon les choix de modèle et de solution par matrices creuses.

ABSTRACT

The main objective of this dissertation is the establishment of more efficient and more precise synchronous machine modeling approaches and solution algorithms for the computation of electromagnetic transients (EMT). Numerical integration time step size is a key factor in both aspects. The capability to use larger time steps in EMT-type simulation methods also contributes to the extension of such methods into the efficient simulation of electromechanical transients.

In this thesis, four new models are proposed in order to improve the precision of the classical dq0 model while maintaining its efficiency. Three of them use the classical dq0 model with increased accuracy. The most accurate models are: dq0 with internal intermediate time step usage, phase-domain and voltage behind reactance. Efficiency is maintained by restricting the accurate model usage to the transient intervals where the precision of the classical dq0 formulation decreases. This approach provides accuracy while maintaining classical dq0 computational speed. However, these three models are designed for typical transient stability cases and their performance deteriorates when the accurate model usage is needed for a large portion of the complete simulation interval. The last forth model proposed in this thesis is obtained by applying Park's transformation to the discretized equations of the phase-domain model. This model maintains the precision of the phase-domain model and eliminates its computational inefficiencies through a constant admittance matrix. Unlike the first three models, its efficiency does not change with simulated system and phenomenon. Precision and efficiency assessment studies demonstrate that this model is superior in both aspects and should be chosen for the computation of both electromagnetic and electromechanical transients in the same computational framework.

The models proposed in this thesis are compared for practical cases and conditions. Precision analysis is performed within the accuracy constraints of the surrounding network and numerical efficiency assessment analysis accounts for the utilized sparse

matrix solver and refactorization scheme. Hence, this work also contributes to better assessment of both numerical precision and efficiency for researched machine models in this thesis and in the recent literature.

This thesis also proposes two new synchronous machine representations for Modified-Augmented-Nodal-Analysis (MANA) formulation. In the first formulation, a machine Thevenin equivalent equation is inserted directly into the main network equations (MNE) using MANA. The second representation is proposed for phase-domain and voltage behind reactance models. In this representation all machine equations are inserted into the MNEs, thus eliminating the requirement of interfacing circuits. Although these formulations do not improve simulation speed, they demonstrate the modeling flexibility achievable through MANA and allow to verify performance hypothesis based on partial factorization.

TABLE OF CONTENTS

LIST OF TABLES

LIST OF FIGURES

LIST of NOTATION and ABBREVIATIONS

(1.1)	Equation 1.1
[1]	Reference 1
$\mathbf{A_n}$	Linear Augmented Network Matrix in MANA formulation
$\mathbf{b_n}$	Vector of known currents and voltages in MANA formulation
$\mathbf{D_m}$	Tridiagonal matrix of damping coefficients
$\mathbf{i_{dq0}}$	Vector of stator currents in dq0 variables
$\mathbf{i_n}$	Vector of current sources in NA formulation
$\mathbf{i_r}$	Vector of rotor currents
$\mathbf{i_s}$	Vector of stator currents in phase variables
$\mathbf{J_m}$	Diagonal matrix of moments of inertia
$\mathbf{K_m}$	Tridiagonal matrix of stiffness coefficients
$\mathbf{L}$	Lower triangular matrix
$\mathbf{L''_{abc}}(\theta)$	Subtransient inductance matrix
$\mathbf{L_{dq0rs}}$	Rotor-stator inductance after Park's transformation
$\mathbf{L_{dq0sr}}$	Stator-rotor inductance after Park's transformation
$\mathbf{L_{dq0ss}}$	Stator-stator inductance after Park's transformation
$\mathbf{L_{rr}}$	Rotor-rotor inductance
$\mathbf{L_{rs}}(\theta)$	Rotor-stator inductance
$\mathbf{L_{sr}}(\theta)$	Stator-rotor inductance
$\mathbf{L_{ss}}(\theta)$	Stator-stator inductance
$\boldsymbol{\lambda}_{\mathbf{dq0}}$	Vector of stator flux linkages in dq0 variables
$\boldsymbol{\lambda}_{\mathbf{r}}$	Vector of rotor flux linkages
$\boldsymbol{\lambda}_{\mathbf{s}}$	Vector of rotor flux linkages in phase variables

p	d/dt
P	Number of poles
$\mathbf{P}(\theta)$	Park's transformation matrix
$\mathbf{P_C}$	Column permutation matrix
$\mathbf{P_R}$	Row permutation matrix
$\mathbf{R}$	Scaling matrix
$\mathbf{R_r}$	Diagonal rotor resistance matrix
$\mathbf{R_s}$	Diagonal stator resistance matrix
$\mathbf{T_a}$	Vector of torques
T_{mach}	Electromagnetic torque of the machine
θ	Angle between magnetic d-axis and magnetic phase a-axis in electrical rad
$\boldsymbol{\theta}_\mathbf{m}$	Vector of angular positions in rad
$\mathbf{u}$	Vector of speed voltages
$\mathbf{U}$	Upper triangular matrix
$\mathbf{v''_{abc}}$	Vector of subtransient voltages
$\mathbf{v_{dq0}}$	Vector of stator voltages in dq0 variables
$\mathbf{v_n}$	Vector of node voltages in NA formulation
$\mathbf{v_r}$	Vector of rotor voltages
$\mathbf{v_s}$	Vector of stator voltages in phase variables
ω	Rotor angular speed, in electrical rad/s
$\boldsymbol{\omega}_\mathbf{m}$	Vector of speeds in rad
$\mathbf{x_n}$	Vector of unknown currents and voltages in MNA formulation
$\mathbf{Y_n}$	Network Admittance Matrix in NA formulation

AMD	Approximate Minimum Degree
ATP	Alternative Transient Programs
BTF	Block Triangular Factorization
COLAMD	Column Approximate Minimum Degree
CPU	Central Processing Unit
EBA	Backward Euler Integration Method
EMT	Electromagnetic Transients
EMTP	Electromagnetic Transients Program
EMTP-RV	Electromagnetic Transients Program Restructured Version
FACT	Flexible AC Transmission
HPP	Hydraulic Power Plant
HVDC	High-Voltage Direct-Current
IITS	Internal Intermediate Time Step
MatEMTP	Transient Analysis Program in MATLAB M-files
MANA	Modified-Augmented-Nodal-Analysis
MNA	Modified Nodal Analysis
MNE	Main Network Equations
MMD	Multiple Minimum Degree
NA	Nodal Analysis
NE	Norton Equivalent
PD	Phase-Domain
SSR	Subsynchronous Resonance
TE	Thevenin Equivalent
TPP	Thermal Power Plant
TRAP	Trapezoidal Integration Method
VBR	Voltage-Behind-Reactance

CHAPTER 1.

INTRODUCTION

Simulation of electromagnetic transients in modern power systems is widely used for the determination of component ratings such as insulation levels and energy absorption capabilities, in the design and optimization process, for testing control and protection systems and for analyzing power system performance in general [1], [2]. In order to simulate electromagnetic transients, various simulation tools have been developed. These simulation tools are called EMTP-type programs and can be categorized as nodal (or modified-nodal or modified-augmented-nodal) equation based and state variable (state-space) based simulators. Contrary to nodal equations, the automatic formulation of state-space equations is significantly more time consuming and requires the computation of the network topological proper-tree. Large scale system simulation software packages are based on nodal equations. The list of packages (EMT or EMTP type programs) includes: EMTP-RV [3], EMTP96 [4], ATP/EMTP [5] and PSCAD/EMTDC [6]. EMTP96 was abandoned after the development of EMTP-RV. ATP is based on the original code of EMTP [4] which evolved to become EMTP96. EMTP-RV is a more recent software and the only one using MANA formulation. The SimPowerSystems software included in the Simulink environment uses state-space formulation [7].

Due to the increased in speed of modern computers and recent improvements in numerical methods, EMT type programs can now be used for studying transient stability (electromechanical transients) or even small signal stability problems, although such studies are traditionally performed using transient stability (stability-type) programs [1], [2]. In transient stability programs, the energy exchange between generators and other dynamic equipments is assumed to take place while the electric network is remaining at system frequency (quasi-steady state approach using fundamental frequency

representation), i.e. the electromagnetic transients are totally ignored during computation of electromechanical transients. This assumption enables the utilization of large simulation time steps (typically 1 to 8 ms for 60 Hz systems), hence provides much better computational speeds when compared to EMT type programs. On the other hand, the stability type method assumptions may lead to significantly inaccurate simulation results. In addition, the fundamental frequency phasor modeling techniques can not directly represent the faster transients characterizing the power electronic based equipments such as HVDC and FACTS components. Therefore, the EMT type programs are becoming indispensable also for simulating electromechanical transients in power systems.

Synchronous machines are essential components in all power systems. They form the principle source of electric energy and provide reactive power required by the transmission network. Moreover, many large industrial loads are driven by synchronous machines. Therefore, accurate modeling and simulation of synchronous machines is indispensable in EMTP type programs. Numerous machine models and solution procedures have been proposed in the literature. Although these models are based on the lumped-parameter coupled electric circuit approach and remain equivalent in continuous time domain, the numerical properties of these models differ when their equations are discretized by utilizing a particular integration method. Hence, the machine models and solution procedures have significant influence on simulation precision and speed. Moreover, depending on the simulated phenomenon and the system model, the machine model or its solution procedure might become a limiting factor that imposes very small integration time steps and causes reduced simulation speeds.

This dissertation presents new modeling approaches and solution procedures for synchronous machines in the computation of electromagnetic transients. The proposed modeling approaches and solution procedures improve computational efficiency significantly while maintaining precision. In addition to simple infinite bus analysis, the proposed modeling approaches and solution procedures are also compared for more

sophisticated and practical cases. This dissertation also studies sparse matrix solver and refactorization schemes in relation with machine models. Computational speed remains the main target in all studies.

1.1. Background

1.1.1. Power System Network Equations in EMTP-type Programs

The nodal equation based power system network model has been widely used in EMTP-type programs. The main system of *symmetric* equations for an n node system is given by

$$\mathbf{Y_n}\ \mathbf{v_n} = \mathbf{i_n} \tag{1.1}$$

Equation (1.1) is referred to as the standard nodal analysis (NA) formulation in the literature and it is based on the assumption that the admittance matrix model exists for all network components. In (1.1), $\mathbf{Y_n}$ is the admittance matrix, $\mathbf{v_n}$ is the vector of node voltages and $\mathbf{i_n}$ is the vector of current sources combined with history current sources for the trapezoidal integration method. Since there are usually voltage sources (known node voltages) in the simulated power system model, (1.1) must be partitioned to keep only the unknown voltages on the left hand side

$$\mathbf{Y'_n}\ \mathbf{v'_n} = \mathbf{i'_n} - \mathbf{Y_s}\ \mathbf{v_s} \tag{1.2}$$

In (1.2), $\mathbf{Y'_n}$ is related only to unknown node voltages $\mathbf{v'_n}$, $\mathbf{i'_n}$ holds the sum of currents entering nodes with unknown voltage, and $\mathbf{Y_s} \in \mathbf{Y_n}$ relates to known voltages $\mathbf{v_s}$. It should be noted that $\mathbf{v_n} = \left[\mathbf{v'_n} \quad \mathbf{v_s}\right]^T$. Despite its formulation efficiency, (1.2) has several important limitations. One of the important disadvantage of this formulation is the inability to incorporate ungrounded voltage sources and has been corrected in [8] by using modified-nodal analysis (MNA) formulation.

The assumption of admittance model existence for every component is a significant limitation. (1.2) becomes a variable rank system to model the ideal switch operations which reduce the computational efficiency, especially when the number of switches and switching frequency become high. In addition, direct representation of the branch relations and the devices with voltage and current relations is not possible. These limitations can be eliminated by using Modified-Augmented-Nodal-Analysis (MANA) formulation as introduced in [9] and improved in [10] and [11]. In MANA formulation, (1.1) is augmented to include extra generic equations and the system of network equations becomes

$$\mathbf{A_n}\ \mathbf{x_n} = \mathbf{b_n} \tag{1.3}$$

In (1.3), $\mathbf{x_n}$ contains the unknown voltage and current quantities, $\mathbf{b_n}$ contains the known current and voltage quantities and $\mathbf{A_n}$ is the linear augmented network matrix ($\mathbf{Y_n} \in \mathbf{A_n}$).

For generic power systems, both $\mathbf{Y_n'}$ in (1.2) and $\mathbf{A_n}$ in (1.3) are sparse. Therefore, depending on used formulation in EMTP type program, the solution of (1.2) or (1.3) is obtained using sparse matrix methods and LU factorization [12]. It is common to use special ordering techniques to obtain sparser LU factors for better solution speed. $\mathbf{A_n}$ in (1.3) has a larger size compared to $\mathbf{Y_n'}$ in (1.2); however, using (1.3) instead of (1.2) does not cause a significant increase in simulation speed due to utilization of efficient sparse matrix solvers. As MANA formulation in (1.3) is superior over NA and MNA, this thesis considers MANA formulation.

Throughout this thesis the system of network equations given in (1.2) and (1.3) will be referred as main network equations (MNE); $\mathbf{Y_n'}$ in (1.2) and $\mathbf{A_n}$ in (1.3) will be referred as MNE coefficient matrices.

1.1.2. Synchronous Machine Modeling in EMT-Type Programs

In EMT-type programs, synchronous machines are modeled outside of the power system network and require a special interface in both NA and MANA formulations. Depending on the utilized machine model, the methods of interfacing machine models with the power system network can be classified into indirect and direct approaches [13].

1.1.2.1. Indirect Approaches

In indirect approaches, the classical dq0 model [14] for synchronous machine is interfaced with the power system network expressed in physical variables and phase coordinates. There are currently three different approaches used to interface the dq0-model of the machine with the power system network.

In the first approach [15], the machine is interfaced using a Norton equivalent in phase coordinates. The Norton resistance matrix is approximated to become time-independent and the Norton current sources result from predicted machine electrical and mechanical variables. Synchronous machine models SM module in EMTP-RV, Type-59 in EMTP96 (also ATP), fall into this category. In EMTP-RV it is optionally possible to iterate with MNE to achieve voltage convergence.

The second approach [16] is based on the compensation method in which the main network is represented as a Thevenin equivalent circuit and interfaced with the synchronous machine dq0 circuits. The universal machine model in ATP/EMTP is implemented using this method. The compensation method suffers, however, from topological limitations [17] and is not considered in this thesis.

In the third approach, used in PSCAD/EMTDC, the machine model is interfaced with the main network as a compensation current source and a special terminating resistance [18]. The Norton current source, that represents the machine, is calculated

using the previous time point terminal voltages of the machine. Hence one time-step delay exists in this approach and this approach is not considered in this thesis.

The key advantage of the first approach over the direct methods is utilization of constant admittance matrix at the expense of predicting certain electrical variables. This eliminates the time consuming refactoring of the MNE coefficient matrix at each solution time point and increases simulation speed. However, accumulation of prediction errors may cause numerical noise problems (in some cases) and even instability especially with large time steps. In order to improve the model stability, it is common to use damping resistances in parallel with model circuit inductances at the expense of reduced model accuracy [15], [19], [20], [21]. However, as illustrated in [21] and in this thesis, the error due to damping resistances is less noticeable at large time steps due to reduced overall accuracy.

1.1.2.2. Direct Approaches

The phase-domain (PD) model is in the original form of the coupled electric circuit in which the model is expressed in physical variables and phase coordinates [22], [23]. In this model, the machine circuits are directly inserted into the MNE, thus providing a simultaneous solution. It has been demonstrated that this approach improves numerical accuracy and stability [24]-[27]. However, due to the time variant self and mutual inductances of the PD model, it is required to update and refactor the MNE coefficient matrix at each solution time point at an increased computational cost. Type-58 in ATP/EMTP is implemented using this model [28].

The voltage-behind-reactance (VBR) machine model was introduced in [29] for the state variable approach and extended to nodal analysis in [26]. As in the PD model, the stator circuit is expressed in phase coordinates and directly inserted into the MNE in order to achieve a simultaneous solution. On the other hand, the rotor equations are expressed in dq-rotor reference. In [26] the analysis of PD and VBR models concludes that the VBR model has a better numerical accuracy and a lower computational cost

when compared to the PD model. However, as in the PD model, due to the time variant self and mutual inductances of the VBR model, it is needed to update and refactor the MNE coefficient matrix at each solution time point.

1.2. Motivation

Although numerous machine models and solution procedures have been proposed for EMTP type programs, their effect on simulation accuracy and speed has not been investigated in details. Analysis for the accuracy assessment of the machine models and solution methods have been presented in [26] for balanced and in [27] for unbalanced faults. In both studies, the accuracy of numerous machine models and solution methods are compared for various numerical integration time step size usage in order to make overall simulation efficiency evaluation. The numerical integration time step size is a key factor in both aspects. On the other hand, in both studies, the accuracy assessment is performed based on the results of machine terminal fault simulations in a simple single-machine infinite bus system which includes only the fault period. In normal practice, it is necessary to simulate faults on transmission facilities. Moreover, the system simulation should also include the fault removal and continue until stability assessment becomes possible. As the presented results in [26] and [27] totally ignore the effect of reduced precision in the surrounding network due to large time step usage, these results are not sufficient to conclude on modeling performance. Therefore, a better assessment of numerical precision for researched machine models is required.

While studying electromechanical transients, such as transient stability or subsynchronous resonance, it is needed to model a large portion of the targeted power system since electromechanical transients include frequency perturbations. Depending on the power system model, the poor accuracy of classical dq0 model might force the utilization of a small numerical integration time step. This creates significant computing time problems for large scale cases and repetitive simulations. However, it can be shown that as the time step increases, the classical dq0 model introduces significant errors

especially in the DC component of armature currents following a discontinuity (fault condition) in the power network. For these types of studies, the simulation accuracy can be improved by switching to a more accurate model (PD or VBR) or a more accurate dq0 model solution procedure following a large disturbance in the network and switching back to classical dq0 model as the DC component of armature currents decays to small values. The more accurate solution for dq0 model can be obtained by implementing an internal intermediate (fractional) time step usage between two existing MNE solution time points at the expense of reduced simulation speed resulting from solving the machine equations more than once. For typical transients, the accurate model or solution procedure is expected to become active only for a small portion of the complete simulation interval. Hence this solution approach is expected to provide similar simulation accuracy with the accurate model or solution procedure while maintaining classical dq0 model like simulation speed.

Although all dq0, PD and VBR models are based on lumped-parameter coupled electric circuit approach and equivalent in continuous time domain, the numerical properties of these models differ when their equations are discretized. The inaccurate behavior of dq0 model at large time steps is resulting from its discretized equations. Therefore, the dq0 model can be reformulated by applying Park's transformation to the discretized equations of the PD model to maintain PD model like accuracy. By implementing a prediction-correction scheme, constant machine admittance matrix usage in MNE can be achieved to provide classical dq0 model like computation efficiency.

Unlike the classical dq0 model, the PD and VBR models need to update and refactor the MNE coefficient matrix at each solution time point. The increase in simulation time due to the usage of the PD model instead of the classical dq0 model is investigated in [24]. In this study, the simulation times are compared for the classical dq0 and PD models usage in ATP (Type-59 and Type-58 synchronous machine models, respectively) for the same time step usage. It should be noted that, ATP performs

complete refactorization at each solution time point. However, the increase in simulation time due to usage of PD or VBR models is expected to be affected by implemented refactorization schemes. In addition, the effect of the sparse matrix solver efficiency on simulation speed is expected to be different for PD and VBR models due to their refactorization requirements at each solution time point. Therefore, the comparisons between the models that use constant and time-varying MNE coefficient matrices should be done by considering these facts. On the other hand, partial refactorization schemes may create other matrix ordering problems and such schemes have not been tested and proven for large scale practical systems.

In both NA and MANA formulations, the machines are represented in MNE by modifying $\mathbf{Y_n}$ and $\mathbf{i_n}$ with their Norton equivalent circuits. On the other hand, MANA formulation does not require or force the admittance model usage. Power system network models in the MANA formulation can be augmented to include extra generic equations based on the machine equations and the nodal relations where the machine is connected. For example inserting Thevenin equivalent circuits of the machines into the MNE will eliminate the calculation of Norton equivalent circuits of the machines at each time step. With this formulation, the solution of the MNE will provide the machine stator currents in addition to the machine stator voltages; hence the calculation of machine stator currents following MNE solution will be also eliminated. When all machine electrical circuit equations are inserted into the MNE, the calculations to form the machine interfacing circuit for the MNE solution and the calculations to find machine electrical variables following the MNE solution will be completely eliminated. It should be noted that, such MANA formulations will increase the size of the MNE coefficient matrix, hence the MNE solution time. However, the increase in the MNE solution time might be less when compared to the time gained from the computations regarding machine equations, especially for efficient sparse matrix solvers.

1.3. Methodology

The methodology used in this thesis is to start by implementing the classical dq0, PD and VBR models. This work is followed by research on new solutions algorithms and modeling approaches. All models are implemented and tested through user-defined modeling facilities available in EMTP-RV [10]. In addition to simple single machine - infinite bus test cases, the machine model performances are also compared for actual practical and large scale cases. In all cases, precision analysis includes surrounding network constraints.

In all simulations, the reference solutions for precision comparisons are obtained from the contributed EMTP-RV software implementation of the PD model and $1\,\mu s$ simulation time step (Δt) [21]. It should be noted that in all simulated cases, all models converge to the reference solution with smaller simulation time step usage and the differences between the reference solutions become negligible for $\Delta t = 1\,\mu s$. The simulations are repeated for all models for different simulation time steps from $50\,\mu s$ to $1\,ms$. In order to evaluate the accuracy of different numerical solutions, the relative error between the reference solution trajectory (f) and the given numerical solution ($\tilde{f}$) is calculated using the 2-norm [30]:

$$\mathrm{e}\% = \left\| \tilde{f} - f \right\|_2 \Big/ \left\| f \right\|_2 \tag{1.4}$$

Simulation accuracy is directly related to the utilized machine model; hence EMTP-RV simulations are sufficient to conclude on model accuracy. On the other hand, as the MNE coefficient matrix is constant for indirect approaches and time-varying for direct approaches, the effect of the sparse matrix solver and implemented refactorization schemes on computational efficiency is different for these approaches. Therefore, EMTP-RV simulations are not sufficient to conclude on the computational efficiency of these models.

For a reasonable computational efficiency comparisons, PD, VBR and the most accurate and efficient models proposed in this thesis are implemented in MatEMTP (a transient analysis program in MATLAB M-files) [9] in addition to proposed MANA formulations and partial refactorization scheme. Three different sparse matrix solvers are used in MatEMTP in order to demonstrate its effect on simulation efficiency. These sparse matrix solvers are:

- LU factorization with approximate column minimum degree ordering (COLAMD) [31],[32];
- LU factorization with approximate minimum degree ordering (AMD) [33],[34];
- KLU Matrix-solve package [35].

All simulations are performed on a computer having a four-core CPU of 2.67 GHz and 4G RAM. Model computational efficiency evaluation is done based on the CPU timings of a practical case simulation. In order to correlate MatEMTP with EMTP-RV CPU timings, the total simulation time (t_{sim}) is decomposed as follows

$$t_{sim} = t_{ss} + t_{update-A\&b} + t_{refactor-MNE} + t_{solve-MNE} + t_{comp} \tag{1.5}$$

where

- t_{ss}: the CPU time for steady state solution, system component initialization and preparation for time-domain simulation,
- $t_{update-A\&b}$: the CPU time for updating $\mathbf{A_n}$ and $\mathbf{b_n}$ in (1.3),
- $t_{refactor-MNE}$: the CPU time for refactoring $\mathbf{A_n}$ in (1.3),
- $t_{solve-MNE}$: the CPU time for solving factorized version of (1.3),
- t_{comp}: the CPU time for updating network equivalents of each system component for MNE solution and solving their equations following MNE solution.

The reasoning behind the decomposition of t_{sim} into five parts is for correctly accounting for their different shares in total simulation time of EMTP-RV and

MatEMTP. Any conclusion made based on only the changes in total simulation time of MatEMTP will not be valid for EMTP-RV. Therefore, the changes in $t_{update-A\&b}$, $t_{refactor-MNE}$, $t_{solve-MNE}$ and t_{comp} in MatEMTP simulations are considered separately to estimate the possible EMTP-RV simulation times with the proposed MANA formulations, partial refactorization scheme for PD and VBR models, and different sparse matrix solver packages.

1.4.Summary of Results and Contributions

The overall contributions and results of this thesis are summarized below:

1. Assessment of Numerical Precision for Existing Machine Models: Unlike existing studies ([26] and [27]), the existing and proposed machine models are compared for more practical cases and conditions. Simulation results show that for a given simulation time step, PD or VBR model usage provides much better precision compared to the classical dq0 model. However, their usage instead of the classical dq0 model does not provide the improvement stated in [26] in practical cases due to the following reasons:

- For a given simulation time step, the classical dq0 model produces less error during fault conditions for the faults on transmission facilities compared to the faults at machine terminals due to large impedance between the fault and the machine terminals,
- Large time step usage causes reduced accuracy in the surrounding network solution and consequently the precisions for all models,
- Large time steps usage create initialization errors and discrepancies with the steady-state phasor solution. This obvious observation is reconfirmed to avoid erroneous statements made in some papers.

According to simulation results, PD and VBR models have similar precision for a given simulation time step. In some cases, they enable utilizing twice the time step of the classical dq0 model while maintaining simulation precision.

2. Discrete-Time dq0 Model with Internal Intermediate Time Step Usage (dq0-IITS): The classical dq0 model solution algorithm is modified by implementing an option for internal intermediate (fractional) time step usage between two existing main network solution time points. This approach improves precision at the expense of reduced simulation speed resulting from solving the machine equations more than once. However, internal intermediate time step usage is restricted to the transient intervals where the precision of the dq0 formulation decreases. As demonstrated in this thesis, when simulation time step is increased, the classical dq0 model introduces significant errors especially in the DC component of armature currents following a fault condition. The restriction of internal intermediate time step usage is achieved by implementing a network switching detection and machine terminal voltage monitoring algorithm for the startup of the transient (perturbation) interval and a field current monitoring algorithm for the decision process of moving back to normal time step after the perturbation interval. For a typical transient stability case, internal intermediate time step usage becomes active only for a small portion of the complete simulation interval. In addition, electromagnetic transients are local by nature, which limits the number of machines with intermediate time point solutions while simulating large scale systems. Therefore, the increase in simulation time is not significant. This solution approach provides similar accuracy with the PD and VBR models.

Similar to the classical dq0 model, this model may require damping resistances for some cases and for larger time-steps, but even with damping resistances it is still able to provide accuracy comparable to PD and VBR models and especially for balanced faults. It should be also noted that, the error due to damping resistances is less noticeable at large time steps due to reduced overall accuracy.

3. Combinations of Classical dq0 Model with PD and VBR Models (dq+PD and dq+VBR): The combinations of the classical dq0 approach with PD and VBR models are designed to improve the performances of the PD and VBR models respectively. Similar to dq0-IITS, the objective is to restrict the usage of PD or VBR modeling to the transient intervals where the precision of the classical dq0 formulation decreases while maintaining dq0 throughout the rest of the simulation. This is achieved by implementing network switching detection and a machine terminal voltage monitoring algorithm for the startup of the transient (perturbation) interval and a field current monitoring algorithm for the decision process of moving back to dq0 after the perturbation interval. For typical transient stability cases, this approach is as precise as the accurate PD and VBR models while maintaining classical dq0 model like simulation speed.

In the dq+PD and dq+VBR models, damping resistances are present only when the machines are using the classical dq0 model. It should be noted that, damping resistances produce high errors during fault conditions due to high armature currents. The effect of damping resistances on the accuracy of the dq+PD and dq+VBR models is not significant because these models move into the PD and VBR models respectively during fault duration.

4. Discrete Time PD-dq0 Model: Although the mathematical backgrounds of classical dq0 and PD models are equivalent in continuous time domain, the numerical properties of these models differ when their equations are discretized. As demonstrated in [21] and in this thesis, the inaccurate behavior of the classical dq0 model at larger time steps is related to its discretized equations. To combine the accuracy of the PD model with the efficiency of the dq0 model, this model is obtained by applying Park's transformation to the discretized equations of the PD model. As it emanates from the discretized PD model, it delivers an accuracy similar to the PD model. As for the classical dq0 model, a prediction-correction scheme is implemented for interfacing with MNE through a constant admittance matrix for computational efficiency. In short, this

model inherits precision and performance from the PD and dq0 models respectively. It is the best model delivered in this thesis.

Alike the classical dq0 model the PD-dq0 version may require damping resistances for correcting numerical stability problems in some cases with large time step usage. However, the error due to damping resistances is less noticeable at large time steps due to reduced overall accuracy.

The driving idea in the dq0-IITS, dq+PD and dq+VBR models is the usage of accurate models for the time intervals where the precision of the classical dq0 formulation decreases. These models are designed for typical transient stability cases where accurate model usage is needed for a small portion of the complete simulation interval. Depending on the simulated phenomenon and the surrounding system model, computational speeds of these models may deteriorate. Therefore, the PD-dq0 model is superior over the proposed dq0-IITS, dq+PD and dq+VBR models.

Although implementing partial refactorization scheme improves the computational efficiency of PD and VBR models significantly, their computational performance is still poor compared to the PD-dq0 model. Therefore, the PD-dq0 model is also superior over the existing machine models in the literature due to its high precision and computational performance. In addition, it offers the advantage of programming simplicity in existing classical dq0 model codes in EMT type programs.

5. Assessment of Numerical Efficiency for Machine Models: PD and VBR models are much less efficient due to time consuming updating and refactoring of the MNE coefficient matrix. In EMTP-RV, PD and VBR models require more than twice the computational time compared to the classical dq0 model for a given simulation time step. Hence, PD or VBR model usage does not provide any advantage in EMTP-RV while simulating practical cases. However, EMTP-RV uses a *complete* refactorization scheme and a sparse matrix solver that employs multiple minimum degree ordering (MMD) to obtain sparser LU factors [3]. In this thesis the implementation of partial

refactorization is demonstrated for various sparse matrix solvers and tested in MatEMTP for a practical case including several synchronous machines. Partial refactorization reduces MNE solution time by 38.7% in MatEMTP simulations for both PD and VBR model usage when LU factorization is used with AMD. By considering this improvement in MatEMTP, total simulation time in EMTP-RV is expected to reduce by 27.7% and 28.5% for PD and VBR model usage, respectively. With this improvement, both PD and VBR models become superior to the classical dq0 model due to their better precision. On the other hand, their computational performance is still very poor compared to the proposed PD-dq0 model.

It should be noted that large simulation time step usage is correlated with the simulated network model. For example, using more precise propagation delay based models for transmission lines instead of multi-phase pi-section models, impose a hard upper limit on simulation time step. Moreover, the usage of large simulation time steps may cause convergence problems in the iterative process with nonlinear devices or other drifts in precision. In such cases, not only the proposed PD-dq0 model, but also the classical dq0 model may be preferred due to its high computational efficiency if it provides acceptable precision.

This thesis also investigates the impact of the utilized sparse matrix solver on simulation efficiency for a typical EMT-type solution method. The machine models using constant and time-varying MNE coefficient matrices, partial and complete refactorization schemes are taken into account. The KLU sparse matrix solver provides the most efficient simulations in all cases, as expected. The improvement in simulation speed with the KLU sparse matrix solver usage instead of LU factorization with AMD, reduce the MNE solution time by 86.4% in MatEMTP simulations with the PD-dq0 model. By considering this improvement in MatEMTP, total simulation time of EMTP-RV is projected to reduce by 25.9%. On the other hand, the improvement in the MNE solution time with KLU usage is smaller in MatEMTP for PD and VBR models with partial refactorization schemes (around 43.5%). This improvement in MatEMTP implies

around 17.2% and 16.5% expected decrease in total simulation time of EMTP-RV for PD and VBR models, respectively. Although, KLU usage improves the simulation speed for all models, the computational difference between PD-dq0 and VBR (or PD) models is expected to become more significant in a typical EMT-type program.

6. Alternative Machine Representation in MNA: As MANA formulation does not require the admittance model for power system components; it enables different machine representations in the MNE. This thesis proposes two new machine representations in MANA formulation. In the first formulation, the Thevenin equivalents of the machines are inserted into the MNE to eliminate machine Norton equivalent calculations and machine stator current calculations following the MNE solution. In the second formulation, all machine equations are inserted into the MNE to eliminate interfacing circuit calculations and machine electrical variable calculations following the MNE solution. It should be noted that, this formulation introduces time dependent terms in the MNE coefficient matrix for the PD-dq0 model. As the advantage of constant MNE coefficient matrix usage disappears, this formulation is not suitable for the PD-dq0 model; hence it is proposed only for PD and VBR representations.

The above formulations are tested in MatEMTP with the KLU sparse matrix solver usage and partial refactorization scheme for PD and VBR models. The first formulation decreases the total simulation time of MatEMTP by 2.6%, 6.0% and 5.3% for PD-dq0, VBR and PD models respectively. However, detailed analysis shows that the possible decrease in EMTP-RV simulation time will be 1.5% for PD-dq0 and below 1% for both PD and VBR models with this formulation. The second formulation decreases the total simulation time of MatEMTP by 20.9% and 18.3% for VBR and PD models respectively. On the other hand, detailed analysis shows that this formulation may even reduce simulation efficiency when transposed into EMTP-RV.

Although proposed formulations are not expected to improve the efficiency of an EMT-type program, they demonstrate the flexibility of MANA.

1.5. About this Thesis

The work presented in this thesis is divided into following chapters:

- Chapter I, Introduction: Motivation, study methodology and important contributions are presented following a brief presentation of EMT-type programs and synchronous machine modelling approaches in the computation of electromagnetic transients.
- Chapter II: Synchronous Machine Equations: Mathematical modeling of the synchronous machine is presented in details.
- Chapter III: Discrete Time Synchronous Machine Models and Solution Procedures in EMTP-Type Programs: The proposed new synchronous machine models and solution procedures for the computation of electromagnetic transients are presented in addition to the existing models and solution procedures in the literature.
- Chapter IV: Studies for Numerical Precision – EMTP-RV Simulations: EMTP-RV simulation results are presented to compare both the precision and efficiency of the proposed models and the existing models in the literature.
- Chapter V: Complementary Studies for Numerical Efficiency Assessment: Partial refactorization implementation and proposed MANA formulations are presented for the direct machine modeling approaches. MatEMTP simulation results are presented for a reasonable efficiency comparison between direct and indirect modeling approaches that considers refactorization scheme, MANA formulation and applied sparse matrix solver.
- Chapter VI: Conclusion.

CHAPTER 2.

SYNCHRONOUS MACHINE EQUATIONS

2.1. Basic Equations for Electrical Part

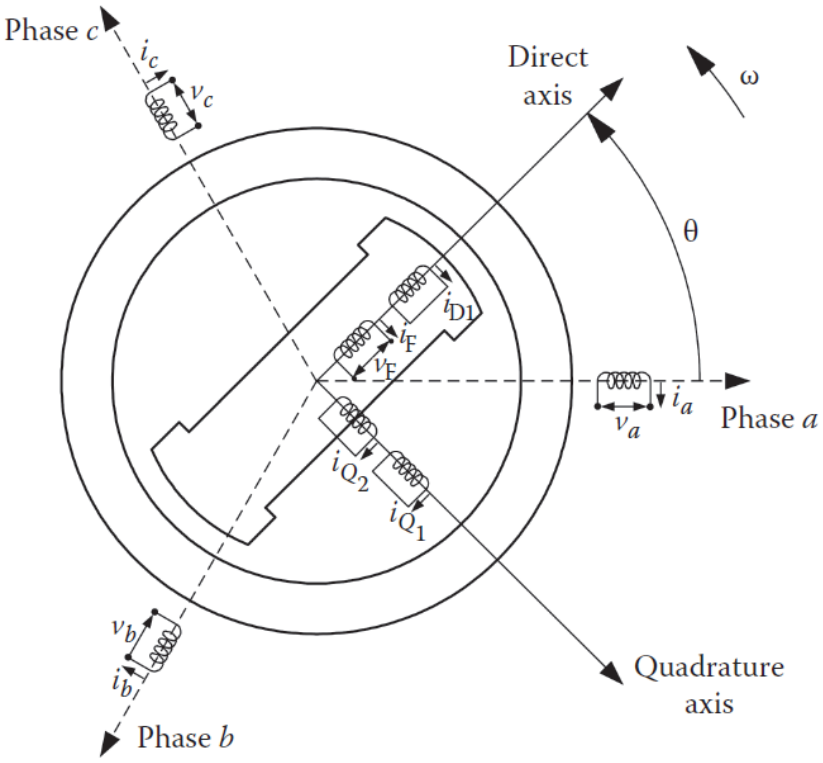

Figure 2.1 Stator and rotor circuits of a synchronous machine

Figure 2.1 illustrates the circuits involved in the analysis of a synchronous machine. The stator circuits are composed of three-phase armature windings and the rotor circuits are composed of the field and the damper windings. Although a large number of circuits are used to represent damper effects in machine design analysis, a limited number of circuits may be used in power system analysis depending on the type of rotor construction and the frequency range of interest. Usually the damper effects are represented with three damper windings: one located on d-axis, and other two located

on q-axis [36]. The rotor circuits have therefore three damper windings and the mathematical model of the machine is based on this assumption in this thesis.

In Figure 2.1, a, b and c are the stator phase windings; F is the field winding, D is the d-axis damper winding; Q_1 and Q_2 are the first and second q-axis damper windings; θ is the angle between magnetic d-axis and magnetic phase a-axis in electrical rad; ω is the rotor angular speed in electrical rad/s.

It should be noted that the electrical equations for one pole-pair machine are the same with the machines having more than one pole-pair except the rotor angular speed and the torque calculated for the mechanical part. The necessary conversion can be done as follows:

$$\omega_{mach} = \omega / (P/2) \tag{2.1}$$

$$T_{mach} = (P/2)\, T \tag{2.2}$$

where P is the number of poles; ω_{mach} and T_{mach} are the actual angular speed and electromagnetic torque values; ω and T are the angular speed and electromagnetic torque values for the 2-pole machine.

The following assumptions are made while developing the mathematical model of the synchronous machine [36]:

- The mmf in the air-gap has sinusoidal distribution and the space harmonics are neglected.
- The effect of stator slots on the rotor inductances is neglected; i.e., saliency is restricted to the rotor.
- The magnetic hysteresis is neglected.
- The magnetic saturation effects are neglected.

The omission of magnetic saturation effects is made to deal with linear coupled circuits and make superposition applicable in the derivation of the basic equations of the synchronous machine. However, saturation effects can be significant and the necessary corrections for accounting their effects will be discussed in Section 2.4.

The stator and rotor flux linkages can be written as

$$\begin{bmatrix} \boldsymbol{\lambda}_s \\ \boldsymbol{\lambda}_r \end{bmatrix} = \mathbf{L}(\theta) = \begin{bmatrix} \mathbf{L}_{ss}(\theta) & \mathbf{L}_{sr}(\theta) \\ \mathbf{L}_{rs}(\theta) & \mathbf{L}_{rr} \end{bmatrix} \begin{bmatrix} \mathbf{i}_s \\ \mathbf{i}_r \end{bmatrix} \tag{2.3}$$

The vectors $\mathbf{i}_s$ and $\boldsymbol{\lambda}_s$ denote the stator currents and flux linkages; the vectors $\mathbf{i}_r$ and $\boldsymbol{\lambda}_r$ denote the rotor currents and flux linkages. $\mathbf{L}_{ss}(\theta)$, $\mathbf{L}_{sr}(\theta)$, $\mathbf{L}_{rs}(\theta)$ and $\mathbf{L}_{rr}$ are the stator-stator, stator-rotor, rotor-stator and rotor-rotor inductances, respectively.

Stator-Stator Inductances: The variation of the permeance of magnetic flux path with the rotor position produces the second harmonic terms for both self and mutual inductances. The stator self and mutual inductances can be expressed as [36]:

$$\begin{aligned} \mathbf{L}_{ss}(\theta) = & \begin{bmatrix} L_{aa0} & L_{ab0} & L_{ab0} \\ L_{ab0} & L_{aa0} & L_{ab0} \\ L_{ab0} & L_{ab0} & L_{aa0} \end{bmatrix} \\ & + L_{aa2} \begin{bmatrix} \cos 2\theta & \cos(2\theta - 2\pi/3) & \cos(2\theta + 2\pi/3) \\ \cos(2\theta - 2\pi/3) & \cos(2\theta + 2\pi/3) & \cos 2\theta \\ \cos(2\theta + 2\pi/3) & \cos 2\theta & \cos(2\theta - 2\pi/3) \end{bmatrix} \end{aligned} \tag{2.4}$$

where L_{aa0} and L_{ab0} correspond to the constant part of the self inductance of each stator winding and mutual inductance between any two stator windings, respectively. L_{aa2} is the maximum value of the second harmonic term for both the self inductance of each stator winding and the mutual inductance between any two stator windings.

Stator-Rotor Inductances: The variation of the mutual inductance is due to the relative motions of the windings. The stator-rotor mutual inductances can be expressed as

$$\mathbf{L_{sr}}(\theta)=\begin{bmatrix} L_{aF}\cos\theta & L_{aD}\cos\theta & L_{aQ1}\sin\theta & L_{aQ2}\sin\theta \\ L_{aF}\cos\left(\theta-\frac{2\pi}{3}\right) & L_{aD}\cos\left(\theta-\frac{2\pi}{3}\right) & L_{aQ1}\sin\left(\theta-\frac{2\pi}{3}\right) & L_{aQ2}\sin\left(\theta-\frac{2\pi}{3}\right) \\ L_{aF}\cos\left(\theta+\frac{2\pi}{3}\right) & L_{aD}\cos\left(\theta+\frac{2\pi}{3}\right) & L_{aQ1}\sin\left(\theta+\frac{2\pi}{3}\right) & L_{aQ2}\sin\left(\theta+\frac{2\pi}{3}\right) \end{bmatrix} \tag{2.5}$$

where L_{aF}, L_{aD}, L_{aQ1}, L_{aQ2} are the maximum values of the mutual inductances between stator phase windings (a, b, c) and the F, D, Q_1, Q_2 windings, respectively.

Rotor-Stator Inductances: As $L_{ij}=L_{ji}$ for $i=a,b,c$ and $j=F,D,Q_1,Q_2$, the rotor-stator mutual inductances can be expressed as

$$\mathbf{L_{rs}}(\theta)=\mathbf{L_{sr}^{T}}(\theta) \tag{2.6}$$

Rotor-Rotor Inductances: The self inductances of the rotor circuit and the mutual inductances between each other do not change with the rotor position. The constant rotor-rotor inductance matrix can be written as

$$\mathbf{L_{rr}}=\begin{bmatrix} L_{FF} & L_{FD} & 0 & 0 \\ L_{FD} & L_{DD} & 0 & 0 \\ 0 & 0 & L_{Q1Q1} & L_{Q1Q2} \\ 0 & 0 & L_{Q1Q2} & L_{Q2Q2} \end{bmatrix} \tag{2.7}$$

where L_{FF}, L_{DD}, L_{Q1Q1} and L_{Q2Q2} are the self inductances of the windings F, D, Q_1 and Q_2, respectively. L_{FD} is the mutual inductance between F and D windings; L_{Q1Q2} is the mutual inductance between Q_1, Q_2 windings.

The voltage equations for the stator and rotor windings are

$$\begin{bmatrix} \mathbf{v_s} \\ \mathbf{v_r} \end{bmatrix} = -\begin{bmatrix} \mathbf{R_s} & \mathbf{0} \\ \mathbf{0} & \mathbf{R_r} \end{bmatrix}\begin{bmatrix} \mathbf{i_s} \\ \mathbf{i_r} \end{bmatrix} - p\begin{bmatrix} \boldsymbol{\lambda_s} \\ \boldsymbol{\lambda_r} \end{bmatrix} \tag{2.8}$$

The vector $\mathbf{v_s}$ denotes the stator voltages and the vector $\mathbf{v_r}$ denotes the rotor voltages. It should be noted that, only the field voltage v_F in $\mathbf{v_r}$ is non-zero. $\mathbf{R_s}$ and $\mathbf{R_r}$ are constant diagonal matrices containing the stator and rotor resistances, i.e.

$$\mathbf{R_s} = diag\left(r_a, r_a, r_a\right) \tag{2.9}$$

$$\mathbf{R_r} = diag\left(r_F, r_D, r_{Q1}, r_{Q2}\right) \tag{2.10}$$

where r_a, r_F, r_D, r_{Q1} and r_{Q2} are the resistances of the stator, F, D, Q_1 and Q_2 windings, respectively.

Generator convention is used while expressing the voltage equations; that is, the currents are assumed to be leaving the winding at the terminals and the terminal voltages are assumed to be the voltage drops in the direction of currents. The electromagnetic torque expression can be found from the co-energy function as below [36]:

$$T_{mach} = -\frac{P}{4}\left[\mathbf{i_s}^T \frac{\partial \mathbf{L_{ss}}(\theta)}{\partial \theta}\mathbf{i_s} + 2\mathbf{i_s}^T \frac{\partial \mathbf{L_{sr}}(\theta)}{\partial \theta}\mathbf{i_r}\right] \tag{2.11}$$

2.2. Park Transformation

Equations (2.3), (2.8) and (2.11) completely describe the electrical behavior of the synchronous machine. However, these equations can be solved numerically and they are not suitable for analytical solution due to time varying inductances. The time-invariant set of machine equations can be obtained through Park Transformation [14]. The new fictitious quantities are obtained from the projection of the actual stator variables along

three axes, which are the direct axis of the rotor winding (d-axis), quadrature axis (q-axis) and the stationary axis. In other words, all the stator quantities are transformed into new fictitious (dq0) variables in which the reference frame rotates with the rotor. Thus, by definition

$$\mathbf{f_s} = \mathbf{P}(\theta)\,\mathbf{f_{dq0}} \tag{2.12}$$

where $\mathbf{f_s}$ are the stator phase quantities that can be either voltages, currents or flux linkages of the stator windings and $\mathbf{f_{dq0}}$ are new fictitious quantities. The park transformation matrix $\mathbf{P}(\theta)$ is given by [36]:

$$\mathbf{P}(\theta) = \begin{bmatrix} k_d\cos\theta & k_q\sin\theta & k_0 \\ k_d\cos(\theta-2\pi/3) & k_q\sin(\theta-2\pi/3) & k_0 \\ k_d\cos(\theta+2\pi/3) & k_q\sin(\theta+2\pi/3) & k_0 \end{bmatrix} \tag{2.13}$$

The constants k_d, k_q and k_0 are arbitrary and their values may be chosen to simplify the numerical coefficients in performance equations. Power invariant transformation (i.e., $\mathbf{P}(\theta)^{-1} = \mathbf{P}(\theta)^{T}$) can be obtained by choosing $k_d = \sqrt{2/3}$, $k_q = \sqrt{2/3}$ and $k_0 = \sqrt{1/3}$ [36]. The major advantage of this transformation is that, all the transformed mutual inductances are reciprocal. The flux linkages in terms of dq0 variables are given by

$$\begin{bmatrix} \boldsymbol{\lambda}_{\mathbf{dq0}} \\ \boldsymbol{\lambda}_{\mathbf{r}} \end{bmatrix} = \mathbf{L}_{\mathbf{dq0}} \begin{bmatrix} \mathbf{i}_{\mathbf{dq0}} \\ \mathbf{i}_{\mathbf{r}} \end{bmatrix} = \begin{bmatrix} \mathbf{L}_{\mathbf{dq0ss}} & \mathbf{L}_{\mathbf{dq0sr}} \\ \mathbf{L}_{\mathbf{dq0rs}} & \mathbf{L}_{\mathbf{rr}} \end{bmatrix} \begin{bmatrix} \mathbf{i}_{\mathbf{dq0}} \\ \mathbf{i}_{\mathbf{r}} \end{bmatrix} \tag{2.14}$$

Here the vectors $\mathbf{i_{dqo}}$ and $\boldsymbol{\lambda}_{\mathbf{dqo}}$ denote the stator currents and flux linkages in dq0 variables respectively. The inductance matrix $\mathbf{L_{dq0}}$ is constant due to Park's transformation and given by

$$\mathbf{L_{dq0ss}} = \mathbf{P}(\theta)^{-1}\,\mathbf{L_{ss}}(\theta)\,\mathbf{P}(\theta) = diag\left(L_d, L_q, L_0\right)$$
$$= \begin{bmatrix} L_{aa0} - L_{ab0} + (3/2)L_{aa2} & 0 & 0 \\ 0 & L_{aa0} - L_{ab0} - (3/2)L_{aa2} & 0 \\ 0 & 0 & L_{aa0} + 2L_{ab0} \end{bmatrix} \tag{2.15}$$

$$\mathbf{L_{dq0sr}} = \mathbf{P}(\theta)^{-1}\,\mathbf{L_{sr}}(\theta) = \begin{bmatrix} L_{dF} & L_{dD} & 0 & 0 \\ 0 & 0 & L_{qQ1} & L_{qQ2} \\ 0 & 0 & 0 & 0 \end{bmatrix}$$
$$= \begin{bmatrix} \sqrt{3/2}\,L_{aF} & \sqrt{3/2}\,L_{aD} & 0 & 0 \\ 0 & 0 & \sqrt{3/2}\,L_{aQ1} & \sqrt{3/2}\,L_{aQ2} \\ 0 & 0 & 0 & 0 \end{bmatrix} \tag{2.16}$$

$$\mathbf{L_{dq0rs}} = \mathbf{L_{rs}}(\theta)\,\mathbf{P}(\theta) = \left(\mathbf{P}(\theta)^{-1}\,\mathbf{L_{sr}}(\theta)\right)^{T} = \mathbf{L}_{\mathbf{dq0sr}}^{T} \tag{2.17}$$

It should be noted that, the fictitious d winding is aligned with the d-axis and the fictitious q winding is aligned with the q-axis as illustrated in Figure 2.2. Hence, there is no coupling between the fictitious d (q) winding and the rotor windings on q (d)-axis.

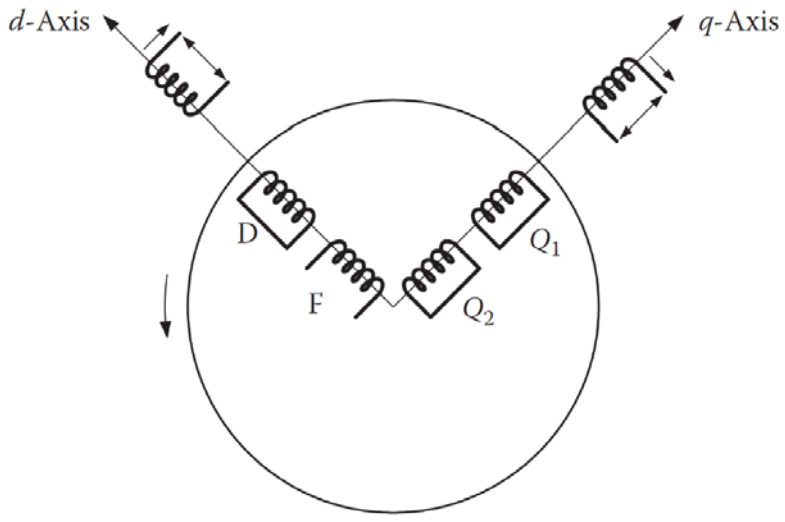

Figure 2.2 Synchronous machine with rotating armature windings

The rotor structure quantities can modified (rescaled) by changing the number of turns in the rotor structure windings to provide $N_d : N_F : N_D$ = 1:1:1 and $N_q : N_{Q1} : N_{Q2}$ = 1:1:1. This provides equal mutual inductances, i.e. $L_{dF} = L_{dD}$ and $L_{qQ1} = L_{qQ2}$. After rescaling the rotor structure, d and q-axis equivalent circuits representing the flux-current relationship will be as illustrated in Figure 2.3 and Figure 2.4, respectively [36]. In these figures λ_d, λ_F, λ_D, λ_q, λ_{Q1} and λ_{Q2} are flux linkages; i_d, i_F, i_D, i_q, i_{Q1} and i_{Q2} are the currents of the d, F, D, q, Q_1, Q_2 windings, respectively. L_{al} is the stator leakage inductance and L_{Fl}, L_{Dl}, L_{Q1l}, L_{Q2l} are the leakage inductances of the F, D, Q_1, Q_2 windings, respectively. L_{FDl} is the leakage inductance that represents the flux linking both F and D windings, but not d winding. L_{ad} $(= L_{dF} = L_{dD})$ and L_{aq} $(= L_{qQ1} = L_{qQ2})$ are the mutual inductances on d and q-axis respectively.

The inductance L_{FDl} is usually omitted. This may be reasonable due to the fact that the damper windings are near the air-gap and the flux linking the damper circuit is nearly equal to that linking the armature. However, this approach is not valid especially for the short-pitched damper circuits and solid rotor iron paths [37].

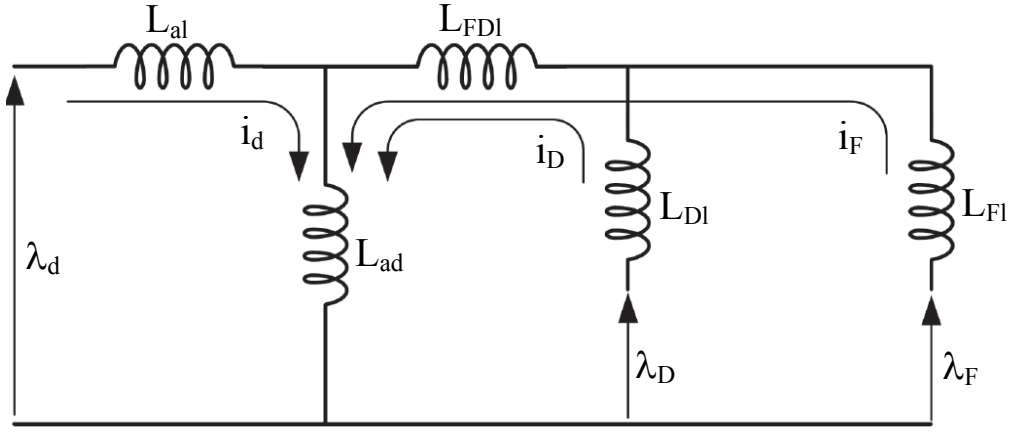

Figure 2.3 d-axis equivalent circuit illustrating flux-current relationship

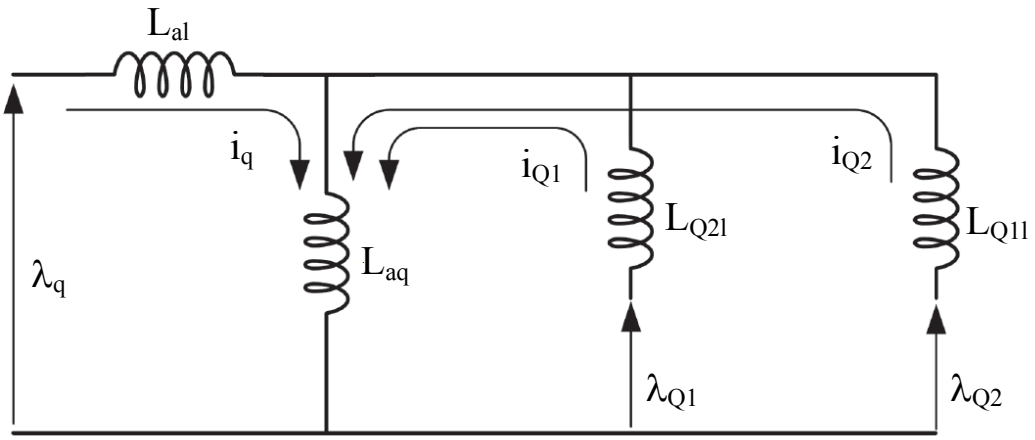

Figure 2.4 q-axis equivalent circuit illustrating flux-current relationship

The voltage equations in terms of dq0 variables are now given by

$$\begin{bmatrix} \mathbf{v_{dqo}} \\ \mathbf{v_r} \end{bmatrix} = -\begin{bmatrix} \mathbf{R_s} & \mathbf{0} \\ \mathbf{0} & \mathbf{R_r} \end{bmatrix}\begin{bmatrix} \mathbf{i_{dqo}} \\ \mathbf{i_r} \end{bmatrix} - p\begin{bmatrix} \boldsymbol{\lambda}_{\mathbf{dqo}} \\ \boldsymbol{\lambda}_{\mathbf{r}} \end{bmatrix} + \begin{bmatrix} \mathbf{u} \\ \mathbf{0} \end{bmatrix} \tag{2.18}$$

where the vector $\mathbf{v_{dqo}}$ denotes the stator voltages in dq0 variables and the vector $\mathbf{u}$ contains speed voltages resulting from the transformation of the reference frame from stationary to rotating,

$$\mathbf{u} = \begin{bmatrix} u_d & u_q & 0 \end{bmatrix}^T = \begin{bmatrix} -\omega\lambda_q & \omega\lambda_d & 0 \end{bmatrix}^T \tag{2.19}$$

The electromagnetic torque is found from

$$T_{mach} = \frac{P}{2}\left(\lambda_{ad}\, i_q - \lambda_{aq}\, i_d\right) \tag{2.20}$$

where λ_{ad} and λ_{aq} are the d and q-axis magnetizing flux linkages [36].

$$\lambda_{ad} = L_{ad}\left(i_d + i_F + i_D\right) \tag{2.21}$$

$$\lambda_{aq} = L_{aq}\left(i_q + i_{Q1} + i_{Q2}\right) \tag{2.22}$$

2.3. Voltage-Behind-Reactance (VBR) Formulation

The VBR formulation decouples the synchronous machine model into a stator subsystem with variables in phase coordinates and into a rotor subsystem with variables in dq coordinates [29]. This formulation assumes all d-axis rotor circuits are linked through a single inductance represented by L_{ad}, i.e. the inductance L_{FDl} in Figure 2.3 is omitted. From (2.18), stator voltage equations can be written as

$$v_d = -r_a\, i_d - p\lambda_d - \omega\, \lambda_q \tag{2.23}$$

$$v_q = -r_a\, i_q - p\lambda_q + \omega\, \lambda_d \tag{2.24}$$

$$v_0 = -r_a\, i_0 - p\lambda_0 \tag{2.25}$$

and rotor voltage equations can be written as

$$v_j = -r_j\, i_j - p\lambda_j;\;\; j = F, D, Q_1, Q_2 \tag{2.26}$$

where r_j denotes the rotor winding resistances; and v_j, i_j and λ_j denote the rotor winding voltages, currents and flux linkages respectively.

By assuming d-axis rotor circuits are linked through a single inductance represented by L_{ad}, the stator and rotor flux linkages can be written as below:

$$\lambda_d = \lambda_{ad} + L_{al}\, i_d \tag{2.27}$$

$$\lambda_q = \lambda_{aq} + L_{al}\, i_q \tag{2.28}$$

$$\lambda_j = \lambda_{ad} + L_{jl}\, i_j;\;\; j = F, D \tag{2.29}$$

$$\lambda_j = \lambda_{aq} + L_{jl}\, i_j;\;\; j = Q_1, Q_2 \tag{2.30}$$

where L_{jl} denotes the leakage inductance of the rotor windings.

Solving (2.27) - (2.30) for currents and substituting into (2.21) and (2.22) yields, after some algebraic manipulations

$$\lambda_{ad} = L''_{ad}\left(i_d + \lambda_F / L_{Fl} + \lambda_D / L_{Dl} \right) \tag{2.31}$$

$$\lambda_{aq} = L''_{aq}\left(i_q + \lambda_{Q1} / L_{Q1l} + \lambda_{Q2} / L_{Q2l} \right) \tag{2.32}$$

where

$$L''_{ad} = \left(1/L_{ad} + 1/L_{Fl} + 1/L_{Dl} \right)^{-1} \tag{2.33}$$

$$L''_{aq} = \left(1/L_{aq} + 1/L_{Q1l} + 1/L_{Q2l} \right)^{-1} \tag{2.34}$$

By substituting (2.31) into (2.27) and (2.32) into (2.28), the stator flux linkages can be expressed as

$$\lambda_d = L''_d\, i_d + \lambda''_d \tag{2.35}$$

$$\lambda_q = L''_q\, i_q + \lambda''_q \tag{2.36}$$

where double primes are used to denote subtransient quantities. The subtransient inductances L''_d and L''_q are given by

$$L''_d = L_{al} + L''_{ad} \tag{2.37}$$

$$L''_q = L_{al} + L''_{aq} \tag{2.38}$$

and the subtransient flux linkages, λ''_d and λ''_q are given by

$$\lambda''_d = L''_{ad}\left(\lambda_F / L_{Fl} + \lambda_D / L_{Dl} \right) \tag{2.39}$$

$$\lambda_q'' = L_{aq}''\left(\lambda_{Q1}/L_{Q1l} + \lambda_{Q2}/L_{Q2l} \right) \tag{2.40}$$

By substituting (2.35) and (2.36) into (2.23) and (2.24), the stator voltage equations can be written as

$$v_d = -r_a\, i_d - L_d''\, pi_d - p\lambda_d'' - \omega\, L_q''\, i_q - \omega\, \lambda_q'' \tag{2.41}$$

$$v_q = -r_a\, i_q - L_q''\, pi_q - p\lambda_q'' + \omega\, L_d''\, i_d + \omega\, \lambda_d'' \tag{2.42}$$

The terms $p\lambda_d''$ and $p\lambda_q''$ in (2.41) and (2.42) can be obtained by taking the derivatives of (2.39) and (2.40). Expressions of the derivatives of the rotor flux linkages can be obtained by manipulating the rotor flux linkage equations (2.29) and (2.30) using

$$i_j = \left(\lambda_j - \lambda_{ad}\right)/L_{jl}\,;\;\; j = F, D \tag{2.43}$$

$$i_j = \left(\lambda_j - \lambda_{aq}\right)/L_{jl}\,;\;\; j = Q_1, Q_2 \tag{2.44}$$

for the rotor currents. By substituting the resulting expressions into (2.41) and (2.42), and after algebraic manipulations, the VBR stator equations are obtained as

$$v_d = -r_a\, i_d - L_d''\, pi_d - \omega\, L_q''\, i_q + v_d'' \tag{2.45}$$

$$v_q = -r_a\, i_q - L_q''\, pi_q + \omega\, L_d''\, i_d + v_q'' \tag{2.46}$$

where

$$\begin{aligned} v_d'' = &-\left(\frac{r_F}{L_{Fl}^2} + \frac{r_D}{L_{Dl}^2} \right) L_{ad}''^2\, i_d - \left[\frac{L_{ad}''\, r_F}{L_{Fl}^2}\left(\frac{L_{ad}''}{L_{Fl}} - 1 \right) + \frac{L_{ad}''^2\, r_D}{L_{Dl}^2\, L_{Fl}} \right] \lambda_F \\ &- \left[\frac{L_{ad}''^2\, r_F}{L_{Dl}\, L_{Fl}^2} + \frac{L_{ad}''\, r_D}{L_{Dl}^2}\left(\frac{L_{ad}''}{L_{Dl}} - 1 \right) \right] \lambda_D - \omega \frac{L_{aq}''}{L_{Q1l}} \lambda_{Q1} - \omega \frac{L_{aq}''}{L_{Q2l}} \lambda_{Q2} - \frac{L_{ad}''}{L_{Fl}} v_F \end{aligned} \tag{2.47}$$

$$v_q'' = -\left(\frac{r_{Q2}}{L_{Q2l}^2}+\frac{r_{Q1}}{L_{Q1l}^2}\right)L_{aq}''^2\, i_q - \left[\frac{L_{aq}''\, r_{Q1}}{L_{Q1l}^2}\left(\frac{L_{aq}''}{L_{Q1l}}-1\right)+\frac{L_{aq}''^2\, r_{Q2}}{L_{Q2l}^2\, L_{Q1l}}\right]\lambda_{Q1}$$
$$-\left[\frac{L_{aq}''^2\, r_{Q1}}{L_{Q2l}\, L_{Q1l}^2}+\frac{L_{aq}''\, r_{Q2}}{L_{Q2l}^2}\left(\frac{L_{aq}''}{L_{Q2l}}-1\right)\right]\lambda_{Q2}+\omega\frac{L_{ad}''}{L_{Fl}}\lambda_F+\omega\frac{L_{ad}''}{L_{Dl}}\lambda_D \tag{2.48}$$

The final form of the stator voltage equations is obtained by applying Park's transformation to (2.45), (2.46) and (2.25),

$$\mathbf{v_s} = -\mathbf{R_s i_s} - p\left[\mathbf{L''_{abc}}(\theta)\,\mathbf{i_s}\right] + \mathbf{v''_{abc}} \tag{2.49}$$

where $\mathbf{L''_{abc}}(\theta)$ and $\mathbf{v''_{abc}}$ are the subtransient inductance matrix and voltages respectively [28]. The subtransient voltages are given by

$$\mathbf{v''_{abc}} = \mathbf{P}(\theta)\begin{bmatrix} v_d'' & v_q'' & 0\end{bmatrix}^T \tag{2.50}$$

The subtransient inductance matrix $\mathbf{L''_{abc}}(\theta)$ is given by

$$\mathbf{L''_{abc}}(\theta) = \begin{bmatrix} L_{aa0}'' & L_{ab0}'' & L_{ab0}'' \\ L_{ab0}'' & L_{aa0}'' & L_{ab0}'' \\ L_{ab0}'' & L_{ab0}'' & L_{aa0}'' \end{bmatrix}$$
$$+L_{aa2}''\begin{bmatrix} \cos 2\theta & \cos(2\theta-2\pi/3) & \cos(2\theta+2\pi/3) \\ \cos(2\theta-2\pi/3) & \cos(2\theta+2\pi/3) & \cos 2\theta \\ \cos(2\theta+2\pi/3) & \cos 2\theta & \cos(2\theta-2\pi/3) \end{bmatrix} \tag{2.51}$$

where

$$L_{aa0}'' = L_{al} + \left(L_{ad}'' + L_{aq}'' + \left(L_0 - L_{al}\right)\right)\Big/3 \tag{2.52}$$

$$L_{ab0}'' = \left(2\left(L_0 - L_{al}\right) - L_{ad}'' - L_{aq}''\right)\Big/6 \tag{2.53}$$

$$L''_{aa2} = \left(L''_{ad} - L''_{aq}\right)/3 \tag{2.54}$$

The stator equations are given by (2.49). From (2.26), (2.43) and (2.44), the rotor state equations can be written as

$$p\lambda_j = -\left(r_j / L_{jl}\right)\left(\lambda_j - \lambda_{ad}\right) + v_j; \;\; j = F, D \tag{2.55}$$

$$p\lambda_j = -\left(r_j / L_{jl}\right)\left(\lambda_j - \lambda_{aq}\right); \;\; j = Q1, Q2 \tag{2.56}$$

In [29], the q-axis is assumed to be leading the d-axis by $90°$ and motor convention is used for the voltage equations while deriving the VBR formulation. In addition, zero sequence inductance L_0 is assumed to be equal to stator leakage inductance L_{al} while expressing the subtransient inductance matrix $\mathbf{L''_{abc}}(\theta)$.

Finally, (2.20) can be used for finding the electromagnetic torque.

As illustrated in this chapter, dq0, PD and VBR models can be derived from each other, i.e. all they are all equivalent in continuous time domain. However, the model parameters for dq0, PD or VBR cannot be directly determined from test/field measurements. The parameters usually provided by the manufacturer are obtained by means of standardized procedures and they need to be converted to model parameters. Appendix I summarizes the techniques used to obtain dq0 model parameters from the different type of data sets.

2.4. Magnetic Saturation

In the derivation of the basic equations of the synchronous machine, magnetic saturation effects are neglected in order to deal with linear coupled circuits and make superposition applicable. However, saturation effects are significant and their effects should be taken into account in power system analysis. In the representation of the magnetic saturation, the following assumptions are usually made [36], [38]:

- The leakage fluxes are considered to be independent of saturation; i.e., only d and q-axis mutual inductances L_{ad} and L_{aq} are saturable.
- The contribution of the leakage fluxes on the iron saturation is neglected; i.e., saturation is determined by the air- gap flux linkage.
- The sinusoidal distribution of the magnetic field over the face of the pole is considered to be unaffected by saturation, hence, d and q-axes remain uncoupled.

For solid-rotor machines, the saturation relationship between the resultant (total) air-gap flux (λ_T) and the magnetomotive force under loaded conditions is considered to be the same as at no-load conditions. With this assumption, a single saturation curve (i.e., open-circuit saturation curve) is sufficient to characterize this phenomenon [36]. The saturation function can be written as

$$\lambda_T = f\left(\lambda_{Tu}\right) = f\left(\sqrt{\lambda_{adu}^2 + \lambda_{aqu}^2}\right) \tag{2.57}$$

$$\lambda_{adu} = L_{adu}\left(i_d + i_F + i_D\right) \tag{2.58}$$

$$\lambda_{aqu} = L_{aqu}\left(i_q + i_{Q1} + i_{Q2}\right) \tag{2.59}$$

where λ_{Tu} is the unsaturated air-gap flux, λ_{adu} and λ_{aqu} are the unsaturated values of d and q-axis magnetizing flux linkages, L_{adu} and L_{aqu} are the unsaturated values of mutual inductances L_{ad} and L_{aq}.

The total air-gap flux λ_T is subjected to saturation and the saturated values of d and q-axis magnetizing flux linkages (λ_{ad} and λ_{aq}) can be found from their unsaturated values (λ_{adu} and λ_{aqu}) by reducing them with the ratio value as illustrated in Figure 2.5.

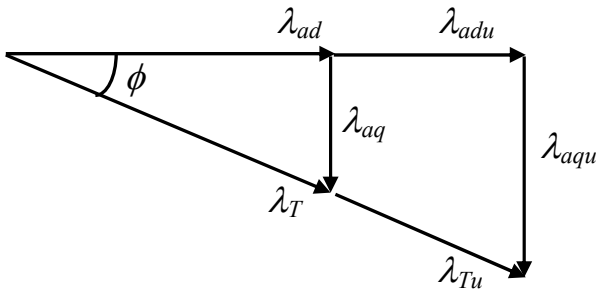

Figure 2.5 Saturated and unsaturated mutual fluxes

In EMT type programs, the magnetic saturation characteristic is usually represented by using a piecewise-linear approximation [3]-[6] as illustrated in Figure 2.6. With piecewise-linear approximation, the simplicity and structure of the magnetically linear machine model is partly preserved, and the iterative solution of saturation function with the machine equations and MNE is avoided.

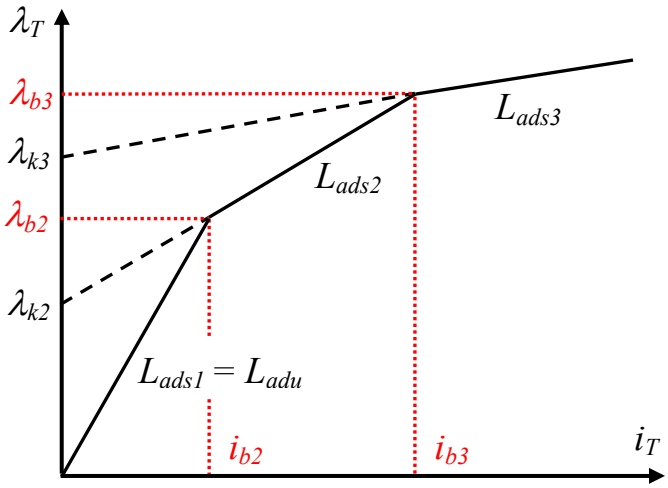

Figure 2.6 Magnetic saturation characteristic (piecewise-linear approximation)

The saturation may be represented by nonlinear functions such as high order polynomials [23], [39] or arctangent functions [40] that may be fitted into the measured saturation data at the expense of forcing an iterative solution of the saturation function with the machine equations and MNE. However, piecewise-linear approximation can include arbitrary number of piecewise-linear segments in order to approach the smooth saturation characteristic with any desirable accuracy.

For the j^{th} operating segment on the saturation curve (see Figure 2.6), λ_T can be written as below

$$\lambda_T = \lambda_{kj} + b_j \lambda_{Tu} = \lambda_{kj} + b_j L_{adu} i_T \tag{2.60}$$

where λ_{kj} is the zero current (residual) flux (see Figure 2.6) , b_j is the saturation factor

$$b_j = L_{adsj} / L_{adu} \tag{2.61}$$

and i_T is defined as

$$i_T = \sqrt{\left(i_d + i_F + i_D\right)^2 + \left(\frac{L_{aqu}}{L_{adu}}\right)^2 \left(i_q + i_{Q1} + i_{Q2}\right)^2} \tag{2.62}$$

The boundaries for the j^{th} operating segment are λ_{bj} and $\lambda_{b(j+1)}$ on λ_T -axis and i_{bj} and $i_{b(j+1)}$ on i_T -axis (see Figure 2.6).

After defining the saturation based on total air-gap flux, it can be separated into d and q -axis as follows

$$\lambda_{ad} = \lambda_{kdj} + b_j \lambda_{adu} = \lambda_{kj} \cos(\phi) + b_j \lambda_{adu} \tag{2.63}$$

$$\lambda_{aq} = \lambda_{kqj} + b_j \lambda_{aqu} = \lambda_{kj} \sin(\phi) + b_j \lambda_{aqu} \tag{2.64}$$

where

$$\phi = \tan^{-1}\left(\lambda_{aqu} / \lambda_{adu}\right) = \tan^{-1}\left(\lambda_{aq} / \lambda_{ad}\right) \tag{2.65}$$

The saturated values of L_{ad} and L_{aq} become

$$L_{ad} = b_j L_{adu} \ , \quad L_{aq} = b_j L_{aqu} \tag{2.66}$$

In case of salient-pole machines, the path for q-axis flux is largely in air and does not vary significantly due to the saturation of the iron path. Therefore, it is usually necessary to adjust only λ_{ad} [36].

$$\lambda_{ad} = f\left(\lambda_{adu}\right) = \lambda_{kj} + b_j \lambda_{adu} \tag{2.67}$$

$$L_{ad} = b_j L_{adu}\ , \quad L_{aq} = L_{aqu} \tag{2.68}$$

$$\lambda_{kdj} = \lambda_{kj}\ , \quad \lambda_{kqj} = 0 \tag{2.69}$$

2.4.1. dq0 Model Equations with Magnetic Saturation

The time-invariant set of equations (2.14), (2.18) and (2.20) completely describes the electrical behavior of the synchronous machine and is called dq0 model in literature. When magnetic saturation is taken into account based on the piecewise-linear approximation described above, for the *j*th operating segment on saturation curve the flux linkages in (2.14) becomes

$$\begin{bmatrix} \boldsymbol{\lambda}_{\mathbf{dqo}} \\ \boldsymbol{\lambda}_{\mathbf{r}} \end{bmatrix} = \mathbf{L}_{\mathbf{dqo}} \begin{bmatrix} \mathbf{i}_{\mathbf{dqo}} \\ \mathbf{i}_{\mathbf{r}} \end{bmatrix} + \begin{bmatrix} \boldsymbol{\lambda}_{\mathbf{dqok}} \\ \boldsymbol{\lambda}_{\mathbf{rk}} \end{bmatrix} \tag{2.70}$$

where

$$\boldsymbol{\lambda}_{\mathbf{dqok}} = \begin{bmatrix} \lambda_{kdj} & \lambda_{kqj} & 0 \end{bmatrix}^T \tag{2.71}$$

$$\boldsymbol{\lambda}_{\mathbf{rk}} = \begin{bmatrix} \lambda_{kdj} & \lambda_{kdj} & \lambda_{kqj} & \lambda_{kqj} \end{bmatrix}^T \tag{2.72}$$

The inductance matrix $\mathbf{L}_{\mathbf{dqo}}$ should be calculated with saturated values of the mutual inductances L_{ad} and L_{aq}, i.e.

$$\mathbf{L_{dq0ss}} = diag\left(L_{al} + d_j\, L_{adu},\, L_{al} + q_j\, L_{aqu},\, L_0\right) \tag{2.73}$$

$$\mathbf{L_{dq0sr}} = \begin{bmatrix} d_j\, L_{adu} & d_j\, L_{adu} & 0 & 0 \\ 0 & 0 & q_j\, L_{aqu} & q_j\, L_{aqu} \\ 0 & 0 & 0 & 0 \end{bmatrix} \tag{2.74}$$

$$\mathbf{L_{rr}} = \begin{bmatrix} L_{Fl} + L_{FDl} & L_{FDl} & 0 & 0 \\ L_{FDl} & L_{Dl} + L_{FDl} & 0 & 0 \\ 0 & 0 & L_{Q1l} & 0 \\ 0 & 0 & 0 & L_{Q2l} \end{bmatrix} + \begin{bmatrix} d_j\, L_{adu} & d_j\, L_{adu} & 0 & 0 \\ d_j\, L_{adu} & d_j\, L_{adu} & 0 & 0 \\ 0 & 0 & q_j\, L_{aqu} & q_j\, L_{aqu} \\ 0 & 0 & q_j\, L_{aqu} & q_j\, L_{aqu} \end{bmatrix} \tag{2.75}$$

In (2.73) - (2.75), $d_j = q_j = b_j$ for solid-rotor machines; $d_j = b_j$ and $q_j = 0$ for salient pole machines.

2.4.2. PD Model Equations with Magnetic Saturation

The set of equations (2.3), (2.8) and (2.11) completely describe the electrical behavior of the synchronous machine and are used for the Phase-Domain (PD) model in literature. Although PD model enables inclusion of magnetic saturation while retaining the physical picture of the actual machine [23], the magnetic saturation representation is implemented in this thesis based on the dq0 variables [38]. For j^{th} operating segment on the saturation curve, the flux linkages in (2.3) becomes

$$\begin{bmatrix} \boldsymbol{\lambda}_\mathbf{s} \\ \boldsymbol{\lambda}_\mathbf{r} \end{bmatrix} = \mathbf{L}(\theta) \begin{bmatrix} \mathbf{i}_\mathbf{s} \\ \mathbf{i}_\mathbf{r} \end{bmatrix} + \begin{bmatrix} \boldsymbol{\lambda}_\mathbf{sk} \\ \boldsymbol{\lambda}_\mathbf{rk} \end{bmatrix} \tag{2.76}$$

where

$$\boldsymbol{\lambda}_\mathbf{sk} = \mathbf{P}(\theta)\boldsymbol{\lambda}_\mathbf{dqok} \tag{2.77}$$

$\mathbf{L}(\theta)$ should be calculated based on the saturated values of the mutual inductances L_{ad} and L_{aq}. The L_{aa0}, L_{ab0} and L_{aa2} terms in the $\mathbf{L_{ss}}(\theta)$ matrix (see (2.15)) become

$$L_{aa0} = L_{al} + \left(d_j \, L_{adu} + q_j \, L_{aqu} + \left(L_0 - L_{al} \right) \right) \Big/ 3 \tag{2.78}$$

$$L_{ab0} = \left(2 \left(L_0 - L_{al} \right) - d_j \, L_{adu} - q_j \, L_{aqu} \right) \Big/ 3 \tag{2.79}$$

$$L_{aa2} = \left(d_j \, L_{adu} - q_j \, L_{aqu} \right) \Big/ 3 \tag{2.80}$$

As the rotor structure quantities are rescaled, $N_d : N_F : N_D$ = 1:1:1 and $N_q : N_{Q1} : N_{Q2}$ = 1:1:1 (i.e. $N_a : N_F : N_D = \sqrt{2/3}$:1:1 and $N_a : N_{Q1} : N_{Q2} = \sqrt{2/3}$:1:1), L_{aF}, L_{aD}, L_{aQ1} and L_{aQ2} terms in $\mathbf{L_{sr}}(\theta)$ and $\mathbf{L_{rs}}(\theta)$ (see (2.16) and (2.17)); become

$$L_{aF} = L_{aD} = \sqrt{2/3} \, d_j \, L_{adu} \tag{2.81}$$

$$L_{aQ1} = L_{aQ2} = \sqrt{2/3} \, q_j \, L_{aqu} \tag{2.82}$$

2.4.3. VBR Model Equations with Magnetic Saturation

The set of equations (2.49), (2.55), (2.56) and (2.11) completely describe the electrical behavior of the synchronous machine for the Voltage-Behind-Reactance (VBR) model [29]. By considering the magnetic saturation, for the j^{th} operating segment on the saturation curve, the v_d'' and v_q'' terms in the subtransient voltages (see (2.50), (2.47) and (2.48)) become

$$
\begin{aligned}
v_d'' = &-\left(\frac{r_F}{L_{Fl}^2}+\frac{r_D}{L_{Dl}^2}\right)L_{ad}''^2\, i_d - \left[\frac{L_{ad}''\, r_F}{L_{Fl}^2}\left(\frac{L_{ad}''}{L_{Fl}}-1\right)+\frac{L_{ad}''^2\, r_D}{L_{Dl}^2\, L_{Fl}}\right]\lambda_F \\
&-\left[\frac{L_{ad}''^2\, r_F}{L_{Dl}\, L_{Fl}^2}+\frac{L_{ad}''\, r_D}{L_{Dl}^2}\left(\frac{L_{ad}''}{L_{Dl}}-1\right)\right]\lambda_D - \left(\frac{r_F}{L_{Fl}^2}+\frac{r_D}{L_{Dl}^2}\right)\frac{L_{ad}''^2}{L_{ad}}\lambda_{kdj} - \frac{L_{ad}''}{L_{ad}}\, p\lambda_{kdj} \\
&-\omega\frac{L_{aq}''}{L_{Q1l}}\lambda_{Q1} - \omega\frac{L_{aq}''}{L_{Q2l}}\lambda_{Q2} - \omega\frac{L_{aq}''}{L_{aq}}\lambda_{kqj} - \frac{L_{ad}''}{L_{Fl}}v_F
\end{aligned}
\tag{2.83}
$$

$$
\begin{aligned}
v_q'' = &-\left(\frac{r_{Q2}}{L_{Q2l}^2}+\frac{r_{Q1}}{L_{Q1l}^2}\right)L_{aq}''^2\, i_q - \left[\frac{L_{aq}''\, r_{Q1}}{L_{Q1l}^2}\left(\frac{L_{aq}''}{L_{Q1l}}-1\right)+\frac{L_{aq}''^2\, r_{Q2}}{L_{Q2l}^2\, L_{Q1l}}\right]\lambda_{Q1} \\
&-\left[\frac{L_{aq}''^2\, r_{Q1}}{L_{Q2l}\, L_{Q1l}^2}+\frac{L_{aq}''\, r_{Q2}}{L_{Q2l}^2}\left(\frac{L_{aq}''}{L_{Q2l}}-1\right)\right]\lambda_{Q2} - \left(\frac{r_{Q2}}{L_{Q2l}^2}+\frac{r_{Q1}}{L_{Q1l}^2}\right)\frac{L_{aq}''^2}{L_{aq}}\lambda_{kqj} \\
&-\frac{L_{aq}''}{L_{aq}}\, p\lambda_{kqj} + \omega\frac{L_{ad}''}{L_{Fl}}\lambda_F + \omega\frac{L_{ad}''}{L_{Dl}}\lambda_D + \omega\frac{L_{ad}''}{L_{ad}}\lambda_{kdj}
\end{aligned}
\tag{2.84}
$$

The expressions for d and q-axis magnetizing flux linkages (λ_{ad} and λ_{aq}) given in (2.31) and (2.32) become

$$\lambda_{ad} = L_{ad}''\left(i_d + \lambda_F / L_{Fl} + \lambda_D / L_{Dl} + \lambda_{kdj} / L_{ad}\right) \tag{2.85}$$

$$\lambda_{aq} = L_{aq}''\left(i_q + \lambda_{Q1} / L_{Q1l} + \lambda_{Q2} / L_{Q2l} + \lambda_{kqj} / L_{aq}\right) \tag{2.86}$$

The L_{ad}'' and L_{aq}'' terms in d and q-axis magnetizing flux linkage (λ_{ad} and λ_{aq}) expressions (see (2.85) and (2.86)), d and q-axis subtransient voltage (v_d'' and v_q'') expressions (see (2.83) and (2.84)) and the subtransient inductance matrix $\mathbf{L''_{abc}}(\theta)$ expression (see (2.51) - (2.54)) should be calculated with saturated values of the d and q-axis mutual inductances L_{ad} ($= d_j\, L_{adu}$) and L_{aq} ($= q_j\, L_{aqu}$).

2.5. Basic Equations for Mechanical Part

The turbine - generator rotor has a complex mechanical structure consisting of several rotors with different sizes connected by shafts of finite stiffness. Although a continuum model of the rotor is required to account for the complete range of torsional oscillations, a simple lumped multimass model is adequate for studying problems related to torsional oscillations [41]. In this approach, each major rotor element is considered to be a rigid mass connected to adjacent elements by mass less shafts with a single equivalent torsional stiffness constant. Figure 2.7 illustrates the structure of a typical multimass model for a generator driven by a tandem compound steam turbine. The six torsional masses represent the rotors of the exciter, the generator, two low pressure (LP) turbine sections, the intermediate pressure (IP) turbine section and the high pressure (HP) turbine section.

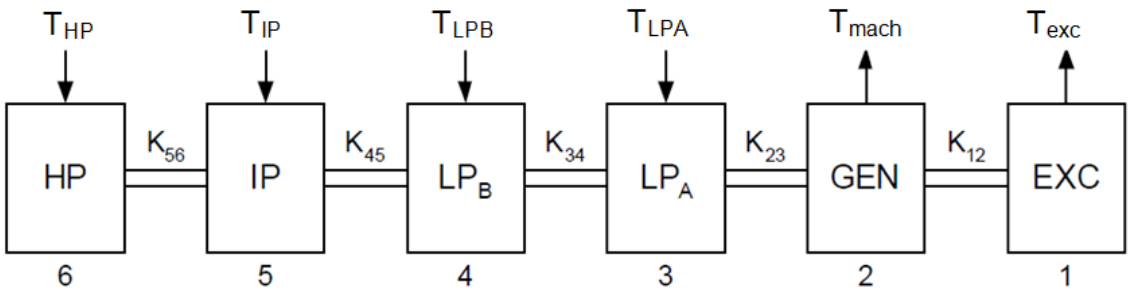

Figure 2.7 Structure of a typical lumped multimass system

This lumped multimass model has the torsional modes in the frequency range of interest. The mechanical subsystem equations can be written as [36]

$$p\,\boldsymbol{\theta}_{\mathbf{m}} = \boldsymbol{\omega}_{\mathbf{m}} \tag{2.87}$$

$$\mathbf{J}_{\mathbf{m}}\, p\,\boldsymbol{\omega}_{\mathbf{m}} + \mathbf{D}_{\mathbf{m}}\,\boldsymbol{\omega}_{\mathbf{m}} + \mathbf{K}_{\mathbf{m}}\,\boldsymbol{\theta}_{\mathbf{m}} = \mathbf{T}_{\mathbf{a}} \tag{2.88}$$

where the subscript m designates mechanical quantities, $\mathbf{J}_{\mathbf{m}}$ is the diagonal matrix of moments of inertia, $\boldsymbol{\omega}_{\mathbf{m}}$ is the vector of speeds, $\boldsymbol{\theta}_{\mathbf{m}}$ is the vector of angular positions,

$\mathbf{D_m}$ and $\mathbf{K_m}$ are the tridiagonal matrices of damping and stiffness coefficients respectively and the vector of torques is given by

$$\mathbf{T_a} = \begin{bmatrix} T_{m1} & \cdots & T_{mi} & -T_{mach} & -T_{exc} \end{bmatrix}^T \tag{2.89}$$

where T_{mi} is the mechanical torque of i^{th} turbine section, T_{mach} and T_{exc} are the electromagnetic machine and exciter torques, respectively. The exciter torque is found from

$$T_{exc} = v_F \; i_F / \omega_{mach} \tag{2.90}$$

In the analysis of power system dynamics, it is a common practice to assume the turbine-generator rotor to be made up of a single mass. In that case both electromagnetic machine torque and mechanical input torque is assumed to be acting on a single mass representing the turbine-generator rotor. For the single mass representation, (2.87) and (2.88) becomes

$$p \; \theta_{mach} = \omega_{mach} \tag{2.91}$$

$$J_m \; p \; \omega_{mach} + D_m \; \omega_{mach} = T_a = T_m - T_{mach} \tag{2.92}$$

where J_m is the total moment of inertia and D_m is damping coefficient.

CHAPTER 3.

DISCRETE-TIME SYNCHRONOUS MACHINE MODELS AND SOLUTION PROCEDURES IN EMT-TYPE PROGRAMS

In EMT-type programs, the solution approach is based on discretizing the differential equations for each circuit component using a particular integration rule. The implicit trapezoidal rule (TRAP) is widely used for discretization followed by the formulation of the MNE. The numerical oscillations of this rule, due to detectable discontinuities, are eliminated using the Backward Euler method (EBA) [3]. The Backward Euler method is used with halved integration time step ($\Delta t / 2$) for two steps (Δt period) as illustrated in Figure 3.1.

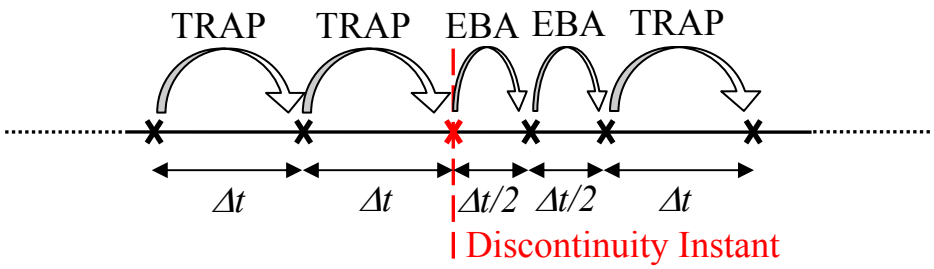

Figure 3.1 Solution following a discontinuity

Numerical solutions for synchronous machine models are obtained from their discretized equations. As NA formulation requires the admittance model for each circuit component, the Norton equivalent circuit is formed for each machine from its discretized equations to interface with the power system network. The Norton equivalent circuits of the machines are inserted into the MNE by modifying $\mathbf{Y_n}$ and $\mathbf{i_n}$ in order to obtain the solution at each time step. Although MANA formulation may provide alternative synchronous machine representations for MNE, the same representation with NA is used here in the MANA solution approach.

3.1. Discrete-Time Mechanical Part Model

By applying the trapezoidal integration rule, the discretized versions of (2.87) and (2.88) can be written as

$$\boldsymbol{\theta}_{\mathbf{m}} = \hat{\boldsymbol{\theta}}_{\mathbf{m}} + k\left(\boldsymbol{\omega}_{\mathbf{m}} + \hat{\boldsymbol{\omega}}_{\mathbf{m}}\right) \tag{3.1}$$

$$\left(\mathbf{J}_{\mathbf{m}} + k\,\mathbf{D}_{\mathbf{m}} + k^2\,\mathbf{K}_{\mathbf{m}}\right)\boldsymbol{\omega}_{\mathbf{m}} = k\,\mathbf{T}_{\mathbf{a}} + \mathbf{h}_{\mathbf{m}} \tag{3.2}$$

where

$$\mathbf{h}_{\mathbf{m}} = \left(\mathbf{J}_{\mathbf{m}} - k\,\mathbf{D}_{\mathbf{m}} - k^2\,\mathbf{K}_{\mathbf{m}}\right)\hat{\boldsymbol{\omega}}_{\mathbf{m}} - 2k\,\mathbf{K}_{\mathbf{m}}\,\hat{\boldsymbol{\theta}}_{\mathbf{m}} + k\,\hat{\mathbf{T}}_{\mathbf{a}} \tag{3.3}$$

and $k = \Delta t / 2$. In the above equations and hereinafter, the hatted variables are available from the previous solution time point.

T_{mach} and T_{exc} in $\mathbf{T_a}$ provide the direct link with the electrical part. Hence, solution of electrical part should be available for solving (3.2). In case the mechanical power input P_{mi} for each turbine i is provided, the torque on each mass i is calculated by using predicted speed ω_{mi}

$$T_{mi} = P_{mi} / \omega_{mi} \tag{3.4}$$

where ω_{mi} is predicted with linear extrapolation, i.e.

$$\omega_{mi}\left(t + \Delta t\right) = 2\,\omega_{mi}\left(t\right) - \omega_{mi}\left(t - \Delta t\right) \tag{3.5}$$

In all machine models, there is also an indirect link through θ (and ω for dq0 and VBR models). The calculation of the Norton equivalent circuit for the MNE and the solution for electrical variables are achieved using the predicted θ and ω values. ω is

predicted with linear extrapolation and θ is calculated by solving the equation of motion using ω

$$\omega(t+\Delta t) = 2\,\omega(t) - \omega(t-\Delta t) \tag{3.6}$$

$$\theta(t+\Delta t) = \theta(t) + k\left(\omega(t+\Delta t) + \omega(t)\right) \tag{3.7}$$

Following a discontinuity, the Backward Euler method is used with halved integration time step ($\Delta t/2$) for two steps (Δt period). For this simulation period, (3.1) and (3.3) becomes

$$\boldsymbol{\theta}_{\mathbf{m}} = \hat{\boldsymbol{\theta}}_{\mathbf{m}} + k\,\boldsymbol{\omega}_{\mathbf{m}} \tag{3.8}$$

$$\mathbf{h}_{\mathbf{m}} = k\,\mathbf{J}_{\mathbf{m}}\,\hat{\boldsymbol{\omega}}_{\mathbf{m}} - k\,\mathbf{K}_{\mathbf{m}}\,\hat{\boldsymbol{\theta}}_{\mathbf{m}} \tag{3.9}$$

Due to the Backward Euler method with $\Delta t/2$, the uniform spacing along time axis is disturbed as illustrated in Figure 3.1. Therefore, the linear predictor formulas given in (3.5) and (3.6) should be modified depending on the solution method for the next time point and the solution method for the previous time point (see Appendix II).

In single mass representation of the turbine-generator rotor, discretized version of (2.91) and (2.92) are used instead of discretized version of (2.87) and (2.88).

3.2. Discrete-Time dq0 Model

The dq0 model is interfaced with the power system network as a Norton Equivalent (NE) in phase coordinates and contains both predicted electrical and mechanical variables. Accumulation of prediction errors may cause numerical noise problems (in some cases) and even instability especially with large time steps. In order to improve the model stability, it is common to use damping resistances in parallel with

model circuit inductances [15], [19], [20], [21]. The reciprocal of the damping factor is defined for a given inductance L and integration time step Δt as

$$\alpha = \left(R_p - 2L/\Delta t\right)\Big/\left(R_p + 2L/\Delta t\right) \tag{3.10}$$

where R_p is the damping resistance. For $\alpha = 1$ there is no damping and critical damping is achieved with $\alpha = 0$. Default values can be used to guarantee model stability, but the highest precision is achieved when R_p is infinity.

By applying the trapezoidal integration rule with (2.70), the discretized version of (2.8) is written as

$$\begin{bmatrix} \mathbf{v_{dqo}} \\ \mathbf{v_r} \end{bmatrix} = -\begin{bmatrix} \mathbf{R_{dq0ss}} & \mathbf{R_{dq0sr}} \\ \mathbf{R_{dq0rs}} & \mathbf{R_{rr}} \end{bmatrix}\begin{bmatrix} \mathbf{i_{dqo}} \\ \mathbf{i_r} \end{bmatrix} - k'\begin{bmatrix} \boldsymbol{\lambda}_{\mathbf{dqok}} \\ \boldsymbol{\lambda}_{\mathbf{rk}} \end{bmatrix} + \begin{bmatrix} \mathbf{u} \\ \mathbf{0} \end{bmatrix} + \begin{bmatrix} \mathbf{h_{dq0s}} \\ \mathbf{h_{dq0r}} \end{bmatrix} \tag{3.11}$$

where

$$\begin{bmatrix} \mathbf{R_{dq0ss}} & \mathbf{R_{dq0sr}} \\ \mathbf{R_{dq0rs}} & \mathbf{R_{rr}} \end{bmatrix} = \begin{bmatrix} \mathbf{R_s} + k'\,\mathbf{L_{dq0ss}} & k'\,\mathbf{L_{dq0sr}} \\ k'\,\mathbf{L_{dq0rs}} & \mathbf{R_r} + k'\,\mathbf{L_{rr}} \end{bmatrix} \tag{3.12}$$

$$\mathbf{h_{dq0s}} = -\alpha\ \mathbf{R_s}\ \hat{\mathbf{i}}_{\mathbf{dq0}} + k'\hat{\boldsymbol{\lambda}}_{\mathbf{dq0}} + \alpha\ \hat{\mathbf{u}} - \alpha\ \hat{\mathbf{v}}_{\mathbf{dq0}} \tag{3.13}$$

$$\mathbf{h_{dq0r}} = -\alpha\ \mathbf{R_r}\ \hat{\mathbf{i}}_{\mathbf{r}} + k'\hat{\boldsymbol{\lambda}}_{\mathbf{r}} - \alpha\ \hat{\mathbf{v}}_{\mathbf{r}} \tag{3.14}$$

and $k' = \left(1+\alpha\right)/\Delta t$.

It is possible to reduce (3.11) into

$$\mathbf{v_{dq0}} = -\mathbf{R_{dq0}}\ \mathbf{i_{dq0}} + \mathbf{e_{dq0}} \tag{3.15}$$

where

$$\mathbf{R_{dq0}} = diag(R_d, R_q, R_0) = \mathbf{R_{dq0ss}} - \mathbf{R_{dq0sr}}\,\mathbf{R_{rr}^{-1}}\,\mathbf{R_{dq0rs}} \tag{3.16}$$

$$\mathbf{e_{dq0}} = \begin{bmatrix} e_d & e_q & e_0 \end{bmatrix}^T = \mathbf{u} - k'\boldsymbol{\lambda}_{\mathbf{dq0k}} - \mathbf{R_{dq0sr}}\mathbf{R_{rr}^{-1}}\left[\mathbf{h_{dq0r}} - \mathbf{v_r} - k'\boldsymbol{\lambda}_{\mathbf{rk}}\right] + \mathbf{h_{dq0s}}$$

(3.17)

The Thevenin equivalent (TE) formed by (3.15) is transformed back to phase coordinates for interfacing with the MNE, using the Park's transformation matrix $\mathbf{P}(\theta)$. This implies the prediction of the machine position angle θ (see (3.6) and (3.7)).

The back transformation of the resistance matrix (given in (3.16)) into phase coordinates produces a time dependent and unsymmetric resistance matrix. The time dependent condition must be avoided since it requires time consuming refactoring of the MNE coefficient matrix. This is achieved by averaging the resistances [15] in (3.16) and by adjusting the Thevenin voltages given in (3.17) to give

$$\mathbf{R_{dq0}} = diag\left(\left(R_d + R_q\right)/2, \left(R_d + R_q\right)/2, R_0\right) \tag{3.18}$$

$$\mathbf{e_{dq0}} = \begin{bmatrix} e_d - \dfrac{R_d - R_q}{2} i_d & e_q - \dfrac{R_q - R_d}{2} i_q & e_0 \end{bmatrix}^T \tag{3.19}$$

In order to form the TE in (3.15), the following electrical variables must be predicted (see (3.17) and (3.19)):

- Fictitious d and q winding currents (i_d and i_q),
- Speed voltages u_d and u_q (see (2.19)),
- Field voltage v_F in $\mathbf{v_r}$,
- Residual flux values λ_{kdj} and λ_{kqj} (see (2.71) and (2.72)) for solid-rotor machines.

The field voltage v_F is set to $\hat{v}_F$. The electrical variables λ_{ad}, λ_{aq}, i_d, i_q, u_d and u_q are obtained with linear three-point prediction with smoothing [15], [19], [20] as illustrated in Figure 3.2, i.e.

$$f\left(t+\Delta t\right)=1.25\,f\left(t\right)+0.5\,f\left(t-\Delta t\right)-0.75\,f\left(t-2\Delta t\right) \tag{3.20}$$

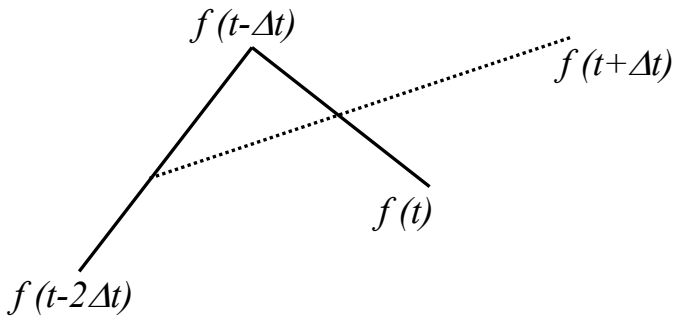

Figure 3.2 Linear three-point prediction with smoothing

The residual flux values λ_{kdj} and λ_{kqj} are calculated from the predicted magnetizing flux values λ_{ad} and λ_{aq}. From (2.63) - (2.65), it can be written as

$$\lambda_{kdj}=\lambda_{kj}\frac{\lambda_{ad}}{\lambda_T},\quad \lambda_{kqj}=\lambda_{kj}\frac{\lambda_{aq}}{\lambda_T} \tag{3.21}$$

In the solid-rotor case, the λ_T is subjected to saturation. As the projection of λ_{kj} on d - and q -axis varies with the angle ϕ, it is required to predict λ_{kdj} and λ_{kqj}. In the salient pole case only λ_{ad} is subject to saturation and the predictions of λ_{kdj} and λ_{kqj} are not required ($\lambda_{kdj}=\lambda_{kj}$, $\lambda_{kqj}=0$).

The Norton equivalents (NE) of the machines are obtained from the TE in (3.15) are inserted into the MNE after transforming back to phase coordinates.

The solution of the MNE gives the stator voltages in phase variables $\mathbf{v_s}$ and the stator voltages in dq0 variables $\mathbf{v_{dqo}}$ can be found using (2.12). The stator currents in dq0 variables $\mathbf{i_{dqo}}$ can be found using (3.15) and $\mathbf{v_{dqo}}$ obtained from the MNE solution

$$\mathbf{i_{dq0}} = \mathbf{G_{dq0}}\left(\mathbf{e_{dq0}} - \mathbf{v_{dq0}}\right) = \mathbf{R_{dq0}}^{-1}\left(\mathbf{e_{dq0}} - \mathbf{v_{dq0}}\right) \tag{3.22}$$

From (3.11), the rotor currents $\mathbf{i_r}$ can be found as

$$\mathbf{i_r} = \mathbf{R_{rr}^{-1}}\left(-\mathbf{R_{dq0rs}}\,\mathbf{i_{dqo}} - k'\,\boldsymbol{\lambda}_{\mathbf{rk}} - \mathbf{v_r} + \mathbf{h_{dq0r}}\right) \tag{3.23}$$

In the solid rotor case, $\boldsymbol{\lambda}_{\mathbf{rk}}$ in (3.23) contains predicted saturation dependent variables λ_{kdj} and λ_{kqj}. Therefore, (3.23) is solved using an iterative approach with the equations in (3.21). This iterative solution process provides corrected values for λ_{kdj} and λ_{kqj} and the rotor currents $\mathbf{i_r}$. The magnetizing flux linkages λ_{ad} and λ_{aq} can be found using (2.63) and (2.64) respectively. The flux linkages ($\boldsymbol{\lambda}_{\mathbf{dqo}}$ and $\boldsymbol{\lambda}_{\mathbf{r}}$) and speed voltages can be found by using (2.70) and (2.19) respectively. In salient pole case, $\boldsymbol{\lambda}_{\mathbf{rk}}$ does not contain predicted values for λ_{kdj} and λ_{kqj}, hence the solution of (3.23) does not require iteration.

It is also possible to obtain a direct solution by solving the first and second rows of (3.11) for magnetizing fluxes λ_{ad} and λ_{aq} [42], i.e.

$$\begin{bmatrix} k' & \omega \\ -\omega & k' \end{bmatrix}\begin{bmatrix} \lambda_{ad} \\ \lambda_{aq} \end{bmatrix} = \begin{bmatrix} \left(r_a + k'\,L_{al}\right)i_d - \omega\,L_{al}\,i_q - v_d + h_d \\ \left(r_a + k'\,L_{al}\right)i_q + \omega\,L_{al}\,i_d - v_q + h_q \end{bmatrix} \tag{3.24}$$

where

$$h_d = \left(-\alpha\,r_a + k'\,L_{al}\right)\hat{i}_d + \hat{\lambda}_{ad} + \alpha\left(u_d - v_d\right) \tag{3.25}$$

$$h_q = \left(-\alpha\, r_a + k'\, L_{al}\right)\hat{i}_q + \hat{\lambda}_{aq} + \alpha\left(u_q - v_q\right) \tag{3.26}$$

As the magnetizing flux linkages λ_{ad} and λ_{aq} are found by using (3.24), (3.23) can be used for the rotor currents without iterations after finding the corrected values for λ_{kdj} and λ_{kqj} from (3.21). This solution approach improves the simulation speed for the solid rotor machine.

The sequence of calculation steps is briefly described below. The solution at $t - \Delta t$ is known and the solution at t is to be found:

1. predict ω and θ (see (3.6) and (3.7)) to calculate $\mathbf{P}(\theta)$;
2. predict electrical variables to calculate $\mathbf{e_{dq0}}$ (see (3.17) and (3.19)) and build the TE in (3.15);
3. solve the MNE to find $\mathbf{v_s}$;
4. find $\mathbf{v_{dqo}}$ from $\mathbf{v_s}$ using (2.12) and use (3.22) for stator currents $\mathbf{i_{dqo}}$;
5. find magnetizing flux linkages λ_{ad} and λ_{aq} from (3.24) and use (3.21) for correcting λ_{kdj} and λ_{kqj};
6. use (3.23) for rotor currents, (2.70) for flux linkages and (2.19) for speed voltages;
7. check for the machine operating segment on saturation curve, if the operating segment needs to change
   - update $\mathbf{L_{dq0}}$ with updated L_{ad} and L_{aq} values (see (2.73) - (2.75)),
   - update λ_{kdj} and λ_{kqj} with updated λ_{kj} value (see (3.21)),

- recalculate magnetizing flux linkages λ_{ad} and λ_{aq} using (2.63) and (2.64), flux linkages using (2.70) with the calculated rotor currents for the new operating segment,
- switch solution method to Backward Euler for the next time step;

8. find electromagnetic torque using (2.20) and solve the mechanical equations (3.1) and (3.2) to find $\boldsymbol{\theta}_{\mathbf{m}}$ and $\boldsymbol{\omega}_{\mathbf{m}}$;

9. compare predicted and corrected ω ($= pp\ \omega_{mach}$), repeat the steps 4 to 9 if no convergence;

10. return to step 1 for the next time point solution.

The above solution procedure is for the solid rotor machine. In the salient pole case, the solution procedure does not contain prediction and correction of λ_{kdj} and λ_{kqj} values (see steps 2 and 5).

In step 7, the operating segment on the saturation curve is found by comparing total air-gap flux λ_T (if solid rotor machine) with the boundary values of each operating segment on λ_T-axis (λ_{bj} and $\lambda_{b(j+1)}$ for j^{th} operating segment, see Figure 2.6). Let a solid rotor machine operate on the j^{th} operating segment. If calculated λ_T value in step 5 is in between the boundary values of the j^{th} operating segment ($\lambda_{bj} < \lambda_T < \lambda_{b(j+1)}$), there is no segment change. If λ_T is greater than $\lambda_{b(j+1)}$, λ_T is recalculated using (2.60) for the $(j+1)^{\text{th}}$ operating segment and compared with $\lambda_{b(j+2)}$, i.e. the upper boundary value of the $(j+1)^{\text{th}}$ operating segment. This will continue until $(j+k)^{\text{th}}$ operating segment if it satisfies $\lambda_{b(j+k)} < \lambda_T < \lambda_{b(j+k+1)}$. If λ_T is smaller than λ_{bj}, λ_T is recalculated for the $(j-1)^{\text{th}}$ operating segment and compared with $\lambda_{b(j-1)}$, i.e. the lower boundary value of the $(j-1)^{\text{th}}$ operating segment. This will continue until the $(j-k)^{\text{th}}$ operating segment if it

satisfies $\lambda_{b(j-k)} < \lambda_T < \lambda_{b(j-k+1)}$. In the salient pole case only d-axis magnetizing flux λ_{ad} is subject to saturation; hence the same procedure is utilized for λ_{ad} instead of λ_T.

It should be noted that the stator currents in phase variables ($\mathbf{i_s}$) are also calculated in step 4 to provide these values to the user as output signals for possible usage in controls.

The Backward Euler method is equivalent to the damped trapezoidal rule with critical damping, hence by setting $\alpha = 0$ the discretized version of machine equations with the Backward Euler method is obtained. However, as the simulation time step is reduced to $\Delta t/2$ during the Backward Euler solution, k' in equations (3.11) - (3.19) becomes $2/\Delta t$.

Due to the Backward Euler method with $\Delta t/2$, the uniform spacing along time axis is disturbed as illustrated in Figure 3.1. Therefore, the predictor formula given in (3.20) should be modified depending on the solution method for the next time point and the methods used for the last two solutions (see Appendix II).

The accuracy of the dq0 model can be improved through an optional iterative scheme with the MNE before advancing to the next time point. The TE is updated for voltage convergence through an iterative process [10], [43] that includes all other nonlinear devices and machines connected through the main network. This approach also eliminates the accumulation of prediction errors and provides desired model stability. Although a Newton method is used, the computational time is increased.

3.3. Discrete-Time PD Model

By applying the trapezoidal integration rule with (2.76), the discretized version of (2.8) is written as

$$\begin{bmatrix} \mathbf{v_s} \\ \mathbf{v_r} \end{bmatrix} = -\begin{bmatrix} \mathbf{R_{ss}}(\theta) & \mathbf{R_{sr}}(\theta) \\ \mathbf{R_{rs}}(\theta) & \mathbf{R_{rr}} \end{bmatrix} \begin{bmatrix} \mathbf{i_s} \\ \mathbf{i_r} \end{bmatrix} - k \begin{bmatrix} \boldsymbol{\lambda}_{\mathbf{sk}} \\ \boldsymbol{\lambda}_{\mathbf{rk}} \end{bmatrix} + \begin{bmatrix} \mathbf{h_s} \\ \mathbf{h_r} \end{bmatrix} \tag{3.27}$$

where

$$\begin{bmatrix} \mathbf{R_{ss}}(\theta) & \mathbf{R_{sr}}(\theta) \\ \mathbf{R_{rs}}(\theta) & \mathbf{R_{rr}} \end{bmatrix} = \begin{bmatrix} \mathbf{R_s} + k\,\mathbf{L_{ss}}(\theta) & k\,\mathbf{L_{sr}}(\theta) \\ k\,\mathbf{L_{rs}}(\theta) & \mathbf{R_r} + k\,\mathbf{L_{rr}} \end{bmatrix} \tag{3.28}$$

$$\mathbf{h_s} = -\,\mathbf{R_s}\,\hat{\mathbf{i}}_\mathbf{s} + k\,\hat{\boldsymbol{\lambda}}_\mathbf{s} - \hat{\mathbf{v}}_\mathbf{s} \tag{3.29}$$

$$\mathbf{h_r} = -\,\mathbf{R_r}\,\hat{\mathbf{i}}_\mathbf{r} + k\,\hat{\boldsymbol{\lambda}}_\mathbf{r} - \hat{\mathbf{v}}_\mathbf{r} \tag{3.30}$$

For the Backward Euler solution with $\Delta t/2$ time step, (3.29) and (3.30) become

$$\mathbf{h_s} = k\,\hat{\boldsymbol{\lambda}}_\mathbf{s} \tag{3.31}$$

$$\mathbf{h_r} = k\,\hat{\boldsymbol{\lambda}}_\mathbf{r} \tag{3.32}$$

Matrix reduction is applied to (3.27) to obtain the TE equation

$$\mathbf{v_s} = -\mathbf{R}_\mathbf{abc}^\mathbf{PD}\,\mathbf{i_s} + \mathbf{e}_\mathbf{abc}^\mathbf{PD} \tag{3.33}$$

where

$$\mathbf{R}_\mathbf{abc}^\mathbf{PD} = \mathbf{R_{ss}}(\theta) - \mathbf{R_{sr}}(\theta)\,\mathbf{R}_\mathbf{rr}^{-1}\,\mathbf{R_{rs}}(\theta) \tag{3.34}$$

$$\mathbf{e}_\mathbf{abc}^\mathbf{PD} = -k\,\boldsymbol{\lambda}_\mathbf{sk} + \mathbf{h_s} - \mathbf{R_{sr}}(\theta)\,\mathbf{R}_\mathbf{rr}^{-1}\left(\mathbf{h_r} - k\,\boldsymbol{\lambda}_\mathbf{rk} - \mathbf{v_r}\right) \tag{3.35}$$

It is assumed that $v_F = \hat{v}_F$, thus $\mathbf{v_r} = \hat{\mathbf{v}}_\mathbf{r}$. The matrix $\mathbf{L}(\theta)$ is calculated by predicting θ (see (3.6) and (3.7)). The residual flux vectors $\boldsymbol{\lambda}_\mathbf{sk}$ and $\boldsymbol{\lambda}_\mathbf{rk}$ in (3.35) can be calculated from d and q-axis residual flux values λ_{kdj} and λ_{kqj} (see (2.71), (2.72)

and (2.77)). Similar to the dq0 model λ_{kdj} and λ_{kqj} values are obtained from predicted magnetizing flux values λ_{ad} and λ_{aq} (see (3.21)) for solid rotor machines. In the salient pole case the predictions of λ_{kdj} and λ_{kqj} are not required ($\lambda_{kdj} = \lambda_{kj}$, $\lambda_{kqj} = 0$). The NE obtained from the TE given in (3.33) is included directly into the MNE. Since $\mathbf{R}_{\mathbf{abc}}^{\mathbf{PD}}$ is continuously changing, it is required to refactor the MNE at each solution time point.

The solution of the MNE gives the stator voltages in phase variables $\mathbf{v_s}$ and stator currents $\mathbf{i_s}$ can be found using (3.33), i.e.

$$\mathbf{i_s} = \mathbf{G}_{\mathbf{abc}}^{\mathbf{PD}} \left(\mathbf{e}_{\mathbf{abc}}^{\mathbf{PD}} - \mathbf{v_s} \right) = \left(\mathbf{R}_{\mathbf{abc}}^{\mathbf{PD}} \right)^{-1} \left(\mathbf{e}_{\mathbf{abc}}^{\mathbf{PD}} - \mathbf{v_s} \right) \tag{3.36}$$

From (3.27), the rotor currents $\mathbf{i_r}$ can be found as

$$\mathbf{i_r} = \mathbf{R}_{\mathbf{rr}}^{-1} \left(-\mathbf{R}_{\mathbf{rs}} \left(\theta \right) \mathbf{i_s} - k' \, \boldsymbol{\lambda}_{\mathbf{rk}} - \mathbf{v_r} + \mathbf{h_r} \right) \tag{3.37}$$

In the solid rotor case, $\boldsymbol{\lambda}_{\mathbf{rk}}$ in (3.37) contains predicted saturation dependent variables λ_{kdj} and λ_{kqj}. Therefore, (3.37) is solved using an iterative approach with (3.21). For the calculation of λ_{ad} and λ_{aq}, $\mathbf{i_{dqo}}$ is calculated from $\mathbf{i_s}$ using (2.12). This iterative solution process provides corrected values for λ_{kdj} and λ_{kqj} and the rotor currents $\mathbf{i_r}$. The magnetizing flux linkages λ_{ad} and λ_{aq} can be found using (2.63) and (2.64) respectively. The flux linkages can be found using (2.76). In the salient pole case, $\boldsymbol{\lambda}_{\mathbf{rk}}$ does not contain predicted values for λ_{kdj} and λ_{kqj}, hence rotor currents are obtained without iterations.

The sequence of calculation steps is briefly described below:

1. predict ω and θ (see (3.6) and (3.7)) to calculate $\mathbf{P}\left(\theta\right)$ and $\mathbf{L}\left(\theta\right)$;

2. predict λ_{kdj} and λ_{kqj} to find $\boldsymbol{\lambda}_{\mathbf{sk}}$ and $\boldsymbol{\lambda}_{\mathbf{rk}}$ (see (2.71), (2.72) and (2.77)) and build the TE in (3.33);

3. refactorize and solve the MNE to find $\mathbf{v}_{\mathbf{s}}$;

4. find stator currents $\mathbf{i}_{\mathbf{s}}$ using (3.36) and use (2.12) for $\mathbf{i}_{\mathbf{dq0}}$;

5. find rotor currents using (3.37);

6. find λ_{ad} using (2.63) and λ_{aq} using (2.64) for correcting λ_{kdj} and λ_{kqj}, hence $\boldsymbol{\lambda}_{\mathbf{sk}}$ and $\boldsymbol{\lambda}_{\mathbf{rk}}$ (see (2.71), (2.72) and (2.77));

7. compare predicted and corrected values for λ_{kdj} and λ_{kqj}, repeat step 5 to 7 with corrected $\boldsymbol{\lambda}_{\mathbf{sk}}$ and if no convergence;

8. check for the machine operating segment on saturation curve, if the operating segment needs to change
   - update L_{ad}, L_{aq} and all related terms in $\mathbf{L}(\theta)$ (L_{aa0}, L_{ab0} and L_{aa2} terms in $\mathbf{L}_{\mathbf{ss}}(\theta)$; L_{aF}, L_{aD}, L_{aQ1} and L_{aQ2} terms in $\mathbf{L}_{\mathbf{sr}}(\theta)$ and $\mathbf{L}_{\mathbf{rs}}(\theta)$, L_{FF}, L_{FD}, L_{DD}, L_{Q1Q1}, L_{Q1Q2}, L_{Q2Q2} terms in $\mathbf{L}_{\mathbf{rr}}$),
   - update λ_{kdj} and λ_{kqj}, hence $\boldsymbol{\lambda}_{\mathbf{sk}}$ and $\boldsymbol{\lambda}_{\mathbf{rk}}$ with updated λ_{kj} value,
   - recalculate magnetizing flux linkages (λ_{ad} and λ_{aq}) with the calculated rotor currents for the new operating segment,
   - switch solution method to Backward Euler for the next time step;

9. find flux linkages using (2.76);

10. find electromagnetic torque using (2.20) and solve the mechanical equations (3.1) and (3.2) to find $\boldsymbol{\theta}_{\mathbf{m}}$ and $\boldsymbol{\omega}_{\mathbf{m}}$;

11. return to step 1 for the next time point solution.

The above solution procedure is for the solid rotor machine. In the salient pole case, the solution procedure does not contain prediction and correction of λ_{kdj} and λ_{kqj}.

The magnetic saturation representation is the same as with the dq0 model, hence in step 8 the operating segment on the saturation curve is found with the same procedure utilized in the dq0 model. λ_{ad}, λ_{aq} and $\mathbf{i_{dq0}}$ are available at each solution time point for magnetic saturation representation. Therefore, the electromagnetic torque equation (2.20) is used instead of complex torque expression given in (2.11). In addition, the stator voltages in dq0 variables ($\mathbf{v_{dq0}}$) are also calculated in step-4 to provide these values to the user as output signals for possible usage in controls.

Unlike the dq0 model, the PD model NE circuit does not contain predicted stator currents. Hence, the PD model is expected to provide desired model stability without damping resistance usage.

3.4. Discrete-Time VBR Model

By applying the trapezoidal integration rule, the discretized version of (2.49) is written as

$$\mathbf{v_s} = -\left(\mathbf{R_s} + k\,\mathbf{L''_{abc}}\left(\theta\right)\right)\mathbf{i_s} + \mathbf{v''_{abc}} + \mathbf{h_{VBRs}} \tag{3.38}$$

where

$$\mathbf{h_{VBRs}} = \left(-\mathbf{R_s} + k\,\mathbf{L''_{abc}}\left(\hat{\theta}\right)\right)\hat{\mathbf{i}}_\mathbf{s} + \hat{\mathbf{v}}''_\mathbf{abc} - \hat{\mathbf{v}}_\mathbf{s} \tag{3.39}$$

For the Backward Euler solution with $\Delta t/2$ time step, (3.39) becomes

$$\mathbf{h_{VBRs}} = k\,\mathbf{L''_{abc}}\left(\hat{\theta}\right)\hat{\mathbf{i}}_\mathbf{s} \tag{3.40}$$

In order to interface the VBR model with the external network, $\mathbf{v''_{abc}}$ must be expressed in terms of $\mathbf{i_s}$. This is achieved by discretizing the rotor state equations (2.55) and (2.56)) and solving for the rotor subsystem output variables. After some algebraic manipulations,

$$\boldsymbol{\lambda}_{\mathbf{r}} = \mathbf{B_I}\ \mathbf{i_{dq}} + \mathbf{B}_{\boldsymbol{\lambda}\mathbf{k}}\ \boldsymbol{\lambda}_{\mathbf{dqk}} + \mathbf{b_{VF}}\ v_F + \mathbf{h_{VBR\lambda}} \tag{3.41}$$

where

$$\mathbf{h_{VBR\lambda}} = \mathbf{A}_{\boldsymbol{\lambda}}\ \hat{\boldsymbol{\lambda}}_{\mathbf{r}} + \mathbf{B_I}\ \hat{\mathbf{i}}_{\mathbf{dq}} + \mathbf{B}_{\boldsymbol{\lambda}\mathbf{k}}\ \hat{\boldsymbol{\lambda}}_{\mathbf{dqk}} + \mathbf{b_{VF}}\ \hat{v}_F \tag{3.42}$$

$$\mathbf{i_{dq}} = \begin{bmatrix} i_d & i_q \end{bmatrix}^T \tag{3.43}$$

$$\boldsymbol{\lambda}_{\mathbf{dqk}} = \begin{bmatrix} \lambda_{kdj} & \lambda_{kqj} \end{bmatrix}^T \tag{3.44}$$

Here, the matrices $\mathbf{A}_{\boldsymbol{\lambda}}$, $\mathbf{B_I}$, $\mathbf{B}_{\boldsymbol{\lambda}\mathbf{k}}$ and $\mathbf{b_{VF}}$, are constant due to dq transformation (see Appendix III). For the Backward Euler solution with $\Delta t/2$ time step, the history term given in (3.42) should be modified in addition to the constant matrices $\mathbf{A}_{\boldsymbol{\lambda}}$, $\mathbf{B_I}$, $\mathbf{B}_{\boldsymbol{\lambda}\mathbf{k}}$ and $\mathbf{b_{VF}}$ in (3.41) as illustrated in Appendix III.

After manipulating (2.83) and (2.84), and using

$$p\,\boldsymbol{\lambda}_{\mathbf{dqk}} = \left(\boldsymbol{\lambda}_{\mathbf{dqk}} - \hat{\boldsymbol{\lambda}}_{\mathbf{dqk}}\right) \Big/ \Delta t \tag{3.45}$$

the subtransient voltages in dq variables can be written as

$$\mathbf{v''_{dq}} = \begin{bmatrix} v''_d & v''_q \end{bmatrix}^T = -\mathbf{K_I}\ \mathbf{i_{dq}} - \mathbf{K}_{\boldsymbol{\lambda}}(\omega)\,\boldsymbol{\lambda}_{\mathbf{r}} - \mathbf{K}_{\boldsymbol{\lambda}\mathbf{k}}(\omega)\,\boldsymbol{\lambda}_{\mathbf{dqk}} - \mathbf{K}_{\mathbf{p}\boldsymbol{\lambda}\mathbf{k}}\left(\boldsymbol{\lambda}_{\mathbf{dqk}} - \hat{\boldsymbol{\lambda}}_{\mathbf{dqk}}\right) - \mathbf{k_{VF}}\ v_F$$

(3.46)

By substituting (3.41) into (3.46) $\mathbf{v''_{dq}}$ is be expressed in terms of $\mathbf{i_{dq}}$, v_F, λ_{kdj} and λ_{kqj} and the history terms $\hat{\boldsymbol{\lambda}}_{\mathbf{r}}$, $\hat{\mathbf{i}}_{\mathbf{dq}}$, $\hat{v}_F$, $\hat{\lambda}_{kdj}$, and $\hat{\lambda}_{kqj}$. By using predicted values of λ_{kdj} and λ_{kqj} and assuming $v_F = \hat{v}_F$, $\mathbf{v''_{dq}}$ can be expressed as

$$\mathbf{v''_{dq}} = -\left(\mathbf{K_I} + \mathbf{K_\lambda}(\omega)\mathbf{B_I}\right)\mathbf{i_{dq}} + \mathbf{h_{VBRr}} \tag{3.47}$$

where

$$\begin{aligned}\mathbf{h_{VBRr}} = &-\left(\mathbf{K_{\lambda k}}(\omega) + \mathbf{K_{p\lambda k}} + \mathbf{K_\lambda}(\omega)\mathbf{B_{\lambda k}}\right)\boldsymbol{\lambda}_{\mathbf{dqk}} + \mathbf{K_{p\lambda k}}\hat{\boldsymbol{\lambda}}_{\mathbf{dqk}} \\ &-\left(\mathbf{k_{VF}} + \mathbf{K_\lambda}(\omega)\mathbf{b_{VF}}\right)v_F - \mathbf{K_\lambda}(\omega)\mathbf{h_{VBR\lambda}}\end{aligned} \tag{3.48}$$

The matrices $\mathbf{K_\lambda}(\omega)$ and $\mathbf{K_{\lambda k}}(\omega)$ depend on the rotor speed ω (see Appendix III) and the source $\mathbf{h_{VBRr}}$ contains v_F, λ_{kdj} and λ_{kqj} and the history terms $\hat{\boldsymbol{\lambda}}_{\mathbf{r}}$, $\hat{\mathbf{i}}_{\mathbf{dq}}$, $\hat{v}_F$, $\hat{\lambda}_{kdj}$ and $\hat{\lambda}_{kqj}$. By transforming $\mathbf{v''_{dq}}$ into phase coordinates and substituting into (3.38), the TE can be found as

$$\mathbf{v_s} = -\mathbf{R}_{\mathbf{abc}}^{\mathbf{VBR}}\,\mathbf{i_s} + \mathbf{e}_{\mathbf{abc}}^{\mathbf{VBR}} \tag{3.49}$$

where

$$\mathbf{R}_{\mathbf{abc}}^{\mathbf{VBR}} = \mathbf{R_s} + \tilde{\mathbf{P}}(\theta)\left(\mathbf{K_I} + \mathbf{K_\lambda}(\omega)\mathbf{B_I}\right)\tilde{\mathbf{P}}^T(\theta) + k\,\mathbf{L''_{abc}}(\theta) \tag{3.50}$$

$$\mathbf{e}_{\mathbf{abc}}^{\mathbf{VBR}} = \tilde{\mathbf{P}}(\theta)\mathbf{h_{VBRr}} + \mathbf{h_{VBRs}} \tag{3.51}$$

In the above equations, $\tilde{\mathbf{P}}(\theta)$ is a submatrix of $\mathbf{P}(\theta)$ and given by

$$\tilde{\mathbf{P}}(\theta) = \sqrt{2/3}\begin{bmatrix} \cos\theta & \sin\theta \\ \cos(\theta - 2\pi/3) & \sin(\theta - 2\pi/3) \\ \cos(\theta + 2\pi/3) & \sin(\theta + 2\pi/3) \end{bmatrix} \tag{3.52}$$

The matrices $\tilde{\mathbf{P}}(\theta)$, $\mathbf{L}''_{\mathbf{abc}}(\theta)$ and the matrix $\mathbf{K}_{\boldsymbol{\lambda}}(\omega)$ in (3.50) are calculated using predicted θ and ω values (see (3.6) and (3.7)). The residual flux values λ_{kdj} and λ_{kqj} are obtained from predicted magnetizing flux values λ_{ad} and λ_{aq} (see (3.21)) for solid rotor machines. In the salient pole case predictions of λ_{kdj} and λ_{kqj} are not required ($\lambda_{kdj} = \lambda_{kj}$, $\lambda_{kqj} = 0$).

The NE obtained from the TE given in (3.49) can be inserted into the MNE. The Thevenin resistance matrix $\mathbf{R}_{\mathbf{abc}}^{\mathbf{VBR}}$ is time dependent and unsymmetric, hence it requires refactoring the MNE at each solution time point.

The solution of the MNE gives the stator voltages in phase variables $\mathbf{v_s}$ and the stator currents in phase variables $\mathbf{i_s}$ can be found using (3.49), i.e.

$$\mathbf{i_s} = \mathbf{G}_{\mathbf{abc}}^{\mathbf{VBR}} \left(\mathbf{e}_{\mathbf{abc}}^{\mathbf{VBR}} - \mathbf{v_s} \right) = \left(\mathbf{R}_{\mathbf{abc}}^{\mathbf{VBR}} \right)^{-1} \left(\mathbf{e}_{\mathbf{abc}}^{\mathbf{VBR}} - \mathbf{v_s} \right) \tag{3.53}$$

The stator currents in dq0 variables $\mathbf{i_{dq0}}$ can be obtained from $\mathbf{i_s}$ using (2.12). In the solid rotor case, (3.41) contains predicted saturation dependent variables λ_{kdj} and λ_{kqj}. Therefore, (3.41) is solved using an iterative approach with (2.85), (2.86) and (3.21). This iterative solution process provides corrected values for λ_{kdj} and λ_{kqj}, the magnetizing flux linkages λ_{ad} and λ_{aq}, and rotor flux linkages $\boldsymbol{\lambda_r}$. The rotor currents can be found by using (2.43) and (2.44). In the salient pole case, (3.41) does not contain predicted values for λ_{kdj} and λ_{kqj}, hence a direct solution is possible.

The sequence of calculation steps is briefly described below:

1. predict ω and θ to calculate $\mathbf{P}(\theta)$, $\mathbf{L}''_{\mathbf{abc}}(\theta)$, $\mathbf{K}_{\boldsymbol{\lambda}}(\omega)$ and $\mathbf{K}_{\boldsymbol{\lambda}\mathbf{k}}(\omega)$;

2. predict λ_{kdj} and λ_{kqj} to build the TE in (3.49);

3. refactorize and solve the MNE to find $\mathbf{v_s}$;

4. find stator currents $\mathbf{i_s}$ using (3.53) and $\mathbf{i_{dq0}}$ using (2.12);

5. find rotor flux linkages $\boldsymbol{\lambda}_\mathbf{r}$ using (3.41);

6. find magnetizing flux linkages (λ_{ad} and λ_{aq}) using (2.85) and (2.86), use (3.21) for correcting λ_{kdj} and λ_{kqj} values;

7. compare predicted and corrected λ_{kdj} and λ_{kqj} values, repeat steps 5-7 if no convergence;

8. find rotor currents using (2.43) and (2.44);

9. calculate $\mathbf{v''_{abc}}$ by transforming $\mathbf{v''_{dq}}$ (see (3.46)) into phase coordinates;

10. check for the machine operating segment on saturation curve, if the operating segment needs to change
    - update L_{ad}, L_{aq} to recalculate L''_{ad} and L''_{aq} ((2.85) and (2.86)); recalculate L''_{aa0}, L''_{ab0} and L''_{aa2} terms in $\mathbf{L''_{abc}}(\theta)$; the matrices $\mathbf{K_\lambda}(\omega)$, $\mathbf{K_I}$, $\mathbf{K_{\lambda k}}(\omega)$, $\mathbf{K_{p\lambda k}}$, $\mathbf{k_{VF}}$, $\mathbf{A_\lambda}$, $\mathbf{B_I}$ and $\mathbf{B_{\lambda k}}$ (see Appendix III);
    - update λ_{kdj} and λ_{kqj} with updated λ_{kj} value,
    - recalculate λ_{ad} and λ_{aq} using (2.63) and (2.64) with the calculated rotor currents for the new operating segment,
    - recalculate $\boldsymbol{\lambda}_\mathbf{r}$ using (2.29) and (2.30),
    - switch solution method to Backward Euler for the next time point;

11. find electromagnetic torque using (2.20) and solve the mechanical equations (3.1) and (3.2) to find $\boldsymbol{\theta}_{\mathbf{m}}$ and $\boldsymbol{\omega}_{\mathbf{m}}$;

12. return to step 1 for the next time point solution.

The above solution procedure is for solid rotor machines. In the salient pole case, the solution procedure does not contain prediction and correction of λ_{kdj} and λ_{kqj}. The operating segment on the saturation curve is found (in step 10) with the same procedure utilized in the dq0 model. Similar to the PD model, the stator voltages in dq0 variables ($\mathbf{v}_{\mathbf{dq0}}$) are also calculated in step-4 to provide these values to the user as output signal for possible usage in controls.

Similar to the PD model, the VBR model NE circuit does not contain predicted stator currents. Hence, the VBR model is expected to provide desired model stability without damping resistance usage.

3.5. Discrete-Time dq0 Model with Internal Intermediate Time Step Usage (dq0-IITS Model)

Although dq0, PD and VBR models are based on the lumped-parameter coupled electric circuit approach and equivalent in continuous time domain, the numerical properties of these models differ when their equations are discretized. As illustrated in [21], when the simulation time step increases, the dq0 model introduces significant errors especially in the DC component of armature currents following a fault condition. Unlike the general belief, the inaccurate behavior of the dq0 model at large time steps is resulting from its discretized equations, not the accumulation of prediction errors.

In order to reduce this error, the solution steps 4 to 9 in the dq0 solution algorithm are modified by implementing an option for internal intermediate (fractional) time step Δt_i usage between two existing main network solution time points $t_x - \Delta t$ and t_x. The

stator voltages $\mathbf{v_{dq0}}$ (found from $\mathbf{v_s}$ available from MNE solution) are linearly interpolated for the intermediate time points. The machine electrical and mechanical equations are solved at each intermediate time point. The solution for currents at the i^{th} intermediate time point is found by rearranging equation (3.11) after expressing the speed voltages $\mathbf{u}$ in terms $\mathbf{i_{dq0}}$ and $\mathbf{i_r}$.

$$\begin{bmatrix} \mathbf{i_{dqo}} \\ \mathbf{i_r} \end{bmatrix} = \tilde{\mathbf{G}}_{\mathbf{dqo}}(\omega) \begin{bmatrix} \tilde{\mathbf{h}}_{\mathbf{dq0s}} - \mathbf{v_{dqo}} - \tilde{k}\,\boldsymbol{\lambda}_{\mathbf{dqok}} \\ \tilde{\mathbf{h}}_{\mathbf{dq0r}} - \mathbf{v_r} - \tilde{k}\,\boldsymbol{\lambda}_{\mathbf{rk}} \end{bmatrix} \tag{3.54}$$

where

$$\mathbf{G_{dqo}}(\omega) = \begin{bmatrix} \mathbf{R_s} + \omega\,\mathbf{K_{ss}} + \tilde{k}\,\mathbf{L_{dq0ss}} & \omega\,\mathbf{K_{sr}} + \tilde{k}\,\mathbf{L_{dq0sr}} \\ \tilde{k}\,\mathbf{L_{dq0rs}} & \mathbf{R_r} + \tilde{k}\,\mathbf{L_{rr}} \end{bmatrix}^{-1} \tag{3.55}$$

$$\mathbf{K_{ss}} = \begin{bmatrix} 0 & 1 & 0 \\ -1 & 0 & 0 \\ 0 & 0 & 0 \end{bmatrix} \mathbf{L_{dq0ss}}; \quad \mathbf{K_{sr}} = \begin{bmatrix} 0 & 1 & 0 \\ -1 & 0 & 0 \\ 0 & 0 & 0 \end{bmatrix} \mathbf{L_{dq0sr}} \tag{3.56}$$

$$\tilde{\mathbf{h}}_{\mathbf{dq0s}} = -\alpha\,\mathbf{R_s}\,\hat{\mathbf{i}}_{\mathbf{dq0}} + \tilde{k}\,\hat{\boldsymbol{\lambda}}_{\mathbf{dq0}} + \alpha\,\hat{\mathbf{u}} - \alpha\,\hat{\mathbf{v}}_{\mathbf{dq0}} \tag{3.57}$$

$$\tilde{\mathbf{h}}_{\mathbf{dq0r}} = -\alpha\,\mathbf{R_r}\,\hat{\mathbf{i}}_{\mathbf{r}} + \tilde{k}\,\hat{\boldsymbol{\lambda}}_{\mathbf{r}} - \alpha\,\hat{\mathbf{v}}_{\mathbf{r}} \tag{3.58}$$

and $\tilde{k} = (1+\alpha)/\Delta t_i$.

In (3.54), the stator voltages $\mathbf{v_{dq0}}$ are linearly interpolated for the intermediate time points and the history terms ($\tilde{\mathbf{h}}_{\mathbf{dq0s}}$ and $\tilde{\mathbf{h}}_{\mathbf{dq0r}}$) are updated after each intermediate time step solution. In the solid rotor case, $\boldsymbol{\lambda}_{\mathbf{dqok}}$ and $\boldsymbol{\lambda}_{\mathbf{rk}}$ in (3.54) contains predicted saturation dependent variables λ_{kdj} and λ_{kqj}. Therefore, (3.54) is solved using an iterative approach with (2.63), (2.64) and (3.21). This iterative solution process provides

corrected values for λ_{kdj} and λ_{kqj} and the machine currents ($\mathbf{i_{dqo}}$, $\mathbf{i_r}$). The flux linkages ($\boldsymbol{\lambda}_{\mathbf{dqo}}$ and $\boldsymbol{\lambda}_{\mathbf{r}}$) and speed voltages can be found using (2.70) and (2.19) respectively. $\mathbf{G_{dqo}}(\omega)$ (see (3.55)) is calculated from the predicted value of ω. After the solution of (3.54), the electromagnetic torque is calculated using (2.20) to solve the mechanical equations (3.1) and (3.2). The final solution of (3.54) at the time point t_x for stator currents will differ from the one found from the network solution, but this difference is negligible. The new TE is calculated with higher precision at t_x for the next solution at $t_x + \Delta t$.

The sequence of calculation steps for intermediate time step solution is briefly described below. The solution at $t - \Delta t_i$ is known and the solution at t is to be found:

1. predict ω to calculate $\mathbf{G_{dqo}}(\omega)$;
2. predict λ_{kdj} and λ_{kqj} for $\boldsymbol{\lambda}_{\mathbf{dqok}}$ and $\boldsymbol{\lambda}_{\mathbf{rk}}$ (see (2.71) and (2.72));
3. find $\mathbf{i_{dq0}}$ and $\mathbf{i_r}$ using (3.54);
4. find λ_{ad} and λ_{aq} using (2.63) and (2.64), use (3.21) for correcting λ_{kdj} and λ_{kqj} values;
5. compare predicted and corrected λ_{kdj} and λ_{kqj} values, repeat steps 3-5 if no convergence;
6. check for the machine operating segment on saturation curve, if the operating segment needs to change
   - update $\mathbf{L_{dq0}}$ with updated L_{ad} and L_{aq} values (see (2.73) - (2.75)),
   - update λ_{kdj} and λ_{kqj} with updated λ_{kj} value using (3.21),

- switch solution method to Backward Euler for the next time step;

7. find electromagnetic torque using (2.20) and solve the mechanical equations ((3.1) and (3.2) with $k = \Delta t_i / 2$) to find $\boldsymbol{\theta}_{\mathbf{m}}$ and $\boldsymbol{\omega}_{\mathbf{m}}$;

8. return to step 1 for the next time point solution.

It should be noted that when the Backward Euler method is used with $\Delta t_i / 2$ for intermediate integration time steps (Δt_i period), α and $\tilde{k}$ are set to zero and $2/\Delta t_i$, respectively.

In all machine models, operating segment changes on the saturation curve cause jumps in machine operating conditions. When large time steps are used, a jump may take place far from the knee point and produce significant errors. This approach enables operating segment change within $t_x - \Delta t$ and t_x due to intermediate time step usage. However, the MNE solution, hence stator voltage values for t_x are obtained for the previous operating segment on the saturation curve. Therefore, this model also suffers from the simulation errors resulting from the jumps in machine operating conditions.

With internal intermediate time step Δt_i usage implementation, the sequence of calculation steps for the discrete time dq0 model given in Section 3.2 becomes:

1. predict ω and θ (see (3.6) and (3.7)) to calculate $\mathbf{P}(\theta)$;

2. predict electrical variables to calculate $\mathbf{e}_{\mathbf{dq0}}$ (see (3.17) and (3.19)) and build the TE in (3.15);

3. solve the MNE to find $\mathbf{v}_{\mathbf{s}}$;

4. find $\mathbf{v}_{\mathbf{dqo}}$ from $\mathbf{v}_{\mathbf{s}}$ using (2.12);

5. solve machine electrical and mechanical equations with intermediate time step Δt_i (see solution procedure above) using linearly interpolated $\mathbf{v_{dq0}}$ values for each intermediate time point;

6. find stator and rotor flux linkages ($\boldsymbol{\lambda}_{\mathbf{dqo}}$ and $\boldsymbol{\lambda}_{\mathbf{r}}$) using (2.70);

7. if the operating segment changes in step 5, switch solution method to Backward Euler for the next time step;

8. return to step 1 for the next time point solution.

It should be noted that intermediate time step is not used with the Backward Euler solution.

Internal intermediate time step usage improves the accuracy of the dq0 model at the expense of solving machine equations more than once at each simulation time step. However, internal intermediate time step usage can be restricted to the transient intervals where the precision of dq0 formulation decreases. This is achieved by implementing network switching detection and machine terminal voltage monitoring algorithm for the startup of the transient (perturbation) interval and field current monitoring algorithm for the decision process of moving back to dq0 model after the perturbation interval.

The intermediate time step usage decision mechanism is triggered automatically and maintained for a user specified time interval (t_{V-mon}) after the detection of a network switching (fault, or other discontinuity) in the main network at $t = t_{sw}$. The machine terminal voltages are then continuously monitored for the specified time interval $\left[t_{sw}, \left(t_{sw} + t_{V-mon}\right)\right]$ and intermediate time step usage is triggered only for machines with voltage excursions above a predefined tolerance, i.e.

$$\left| \frac{\max\left(\Delta V_t\right)}{V_t(t_{sw} - \Delta t)} - 1 \right| > \Delta V_{t-tol} \tag{3.59}$$

where

$$V_t = \sqrt{v_d^2 + v_q^2} \tag{3.60}$$

and ΔV_{t-tol} is the maximum change in machine terminal voltage V_t during terminal voltage monitoring time interval.

The selection of ΔV_{t-tol} and t_{V-mon} are very important for the efficiency of this model. Very low values of ΔV_{t-tol} may cause triggering intermediate time step usage unnecessarily following a small transient. On the other hand very high values of ΔV_{t-tol} may cause normal time step Δt usage although the precision of the dq0 formulation decreases. Such cases can be expected during unbalanced fault conditions while using very high values of ΔV_{t-tol}. It is experimentally found that 5% tolerance value provides acceptable performance.

The selection of t_{V-mon} becomes important when simulating large scale systems. A fault condition affects the machine terminal voltage with a time delay depending on the electrical distance between the fault and the machine. As illustrated in this thesis, the dq0 model produces higher errors as the electrical distance between the fault and the machine reduces. Therefore, t_{V-mon} should be sufficiently long for accumulation of sufficient numerical data and also sufficiently short to avoid unnecessarily triggering intermediate time step usage for machines where the precision of the dq0 formulation is sufficient. It is experimentally found that acceptable performance can obtained when t_{V-mon} is selected between 2 to 5 ms.

The decision for moving back to normal time step Δt is based on the maximum change in the field current i_F within last fundamental cycle period t_{fc} with intermediate time step usage.

$$\left| \frac{\max\left(\Delta i_F\right)}{i_F(t-t_{fc})} - 1 \right| < \Delta i_{F-tol} \tag{3.61}$$

where $\max\left(\Delta i_F\right)$ is maximum change in field current within fundamental cycle period moving window, i.e. $\left[t-t_{fc}, t\right]$.

The idea behind monitoring field current is the fact that, DC armature current components induce fundamental AC frequency field current component. It should be noted that, the large changes in field current magnitude within one fundamental cycle period is mainly due to either presence of DC armature current components or presence of very high value negative and zero sequence components in armature currents during unbalanced faults. Hence, monitoring only the maximum change in field currents is sufficient to determine the transient intervals where the precision of dq0 formulation is expected to decrease.

In [21], the decision for moving back to the main Δt is based on estimating field current AC and DC components and comparing the AC over DC ratio to a predefined tolerance. The possible decision errors are avoided by checking the frequency and field current harmonics. However, the proposed decision mechanism in this thesis is easier to implement and it is also experimentally found that the proposed decision mechanism provides similar performance. The solution algorithm for dq0-ITS model is summarized in Figure 3.3.

In [21], the intermediate time step usage option is triggered automatically and maintained for half fundamental frequency cycle (t_{hc}), after the detection of a network switching (fault, for example) in the main network. The machine field current is then continuously monitored and intermediate time steps are maintained only for machines with current excursions above a predefined tolerance. This approach causes unnecessarily intermediate time step usage for half fundamental frequency cycle period for the machines that are not affected from the transient resulting from network

switching. Moreover, computational speed of this approach will deteriorate when the network encounters repetitive switching events such as for power electronics models. However, the proposed approach determines intermediate time step usage based on the maximum machine terminal voltage change due to network switching. Hence intermediate time step usage is triggered only for the machines affected from the transient resulting from network switching. The proposed approach is also expected to eliminate the efficiency problem resulting from repetitive switching events for power electronics models.

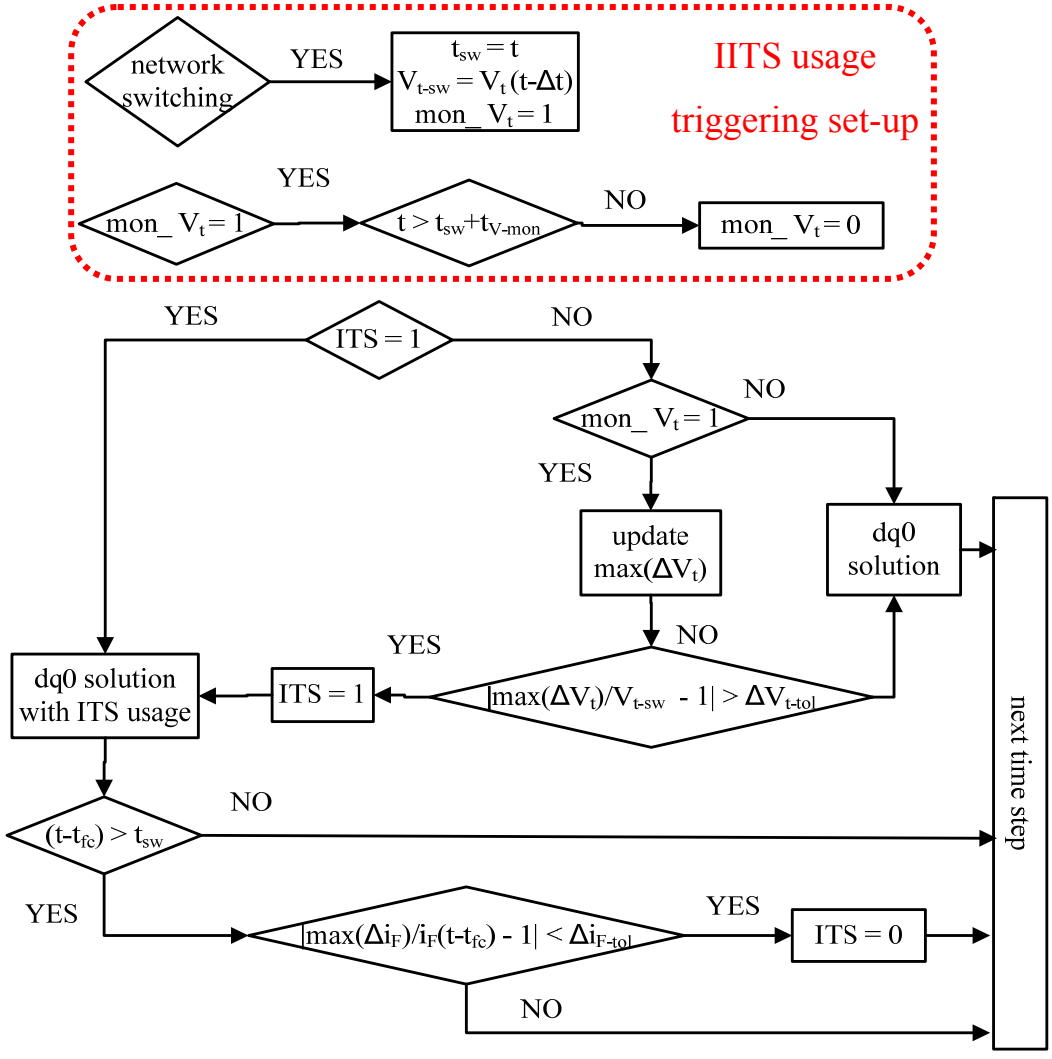

Figure 3.3 Solution algorithm for dq0-IITS model

This solution approach is expected to increase the accuracy of the dq0 model at the expense of solving some of the machine equations more than once. However, electromagnetic transients are local in character, and only a limited number of machines are expected to be solved with smaller time step following a disturbance when a very large scale network is simulated. Moreover, in a typical transient stability case, intermediate time step usage is expected to become active only for a small portion of the complete simulation interval. Therefore, this approach is expected to increase the computational speed significantly especially when simulating very large scale systems.

3.6. Combinations of dq0 Model with PD and VBR Models (dq+PD and dq+VBR Models)

The combinations of dq0 models with PD and VBR models (dq+PD and dq+VBR) are designed to improve the performances of PD and VBR models respectively. Similar to dq0-ITS model, the objective is to restrict the usage of PD or VBR modeling to the transient intervals where the precision of dq0 formulation decreases while maintaining dq0 throughout the rest of the simulation. It requires the implementation of network switching detection and machine terminal voltage monitoring algorithm for the startup of the transient (perturbation) interval and field current monitoring algorithm for the decision process of moving back to dq0 after the perturbation interval.

This approach proposes to switch all machine models to PD (or VBR) modeling from dq0 if any machine is subjected to a voltage excursion above a predefined tolerance after the detection of a network switching (see (3.59)). The field currents of the perturbed machines are monitored to make the decision for switching back to dq0. The decision mechanism is similar to dq0-ITS. All machine models are switched back to dq0 when the maximum change in field current is smaller than a predefined tolerance for all monitored machines within fundamental cycle period moving window, i.e. $\left[t - t_{fc}, t\right]$ (see (3.61)).

In case of a network switching detection during PD (or VBR) model usage, only the previously unmonitored machines are controlled for a large terminal voltage deviation and added to the list of monitored machines if necessary. The solution algorithm for the PD+dq0 model is summarized in Figure 3.4.

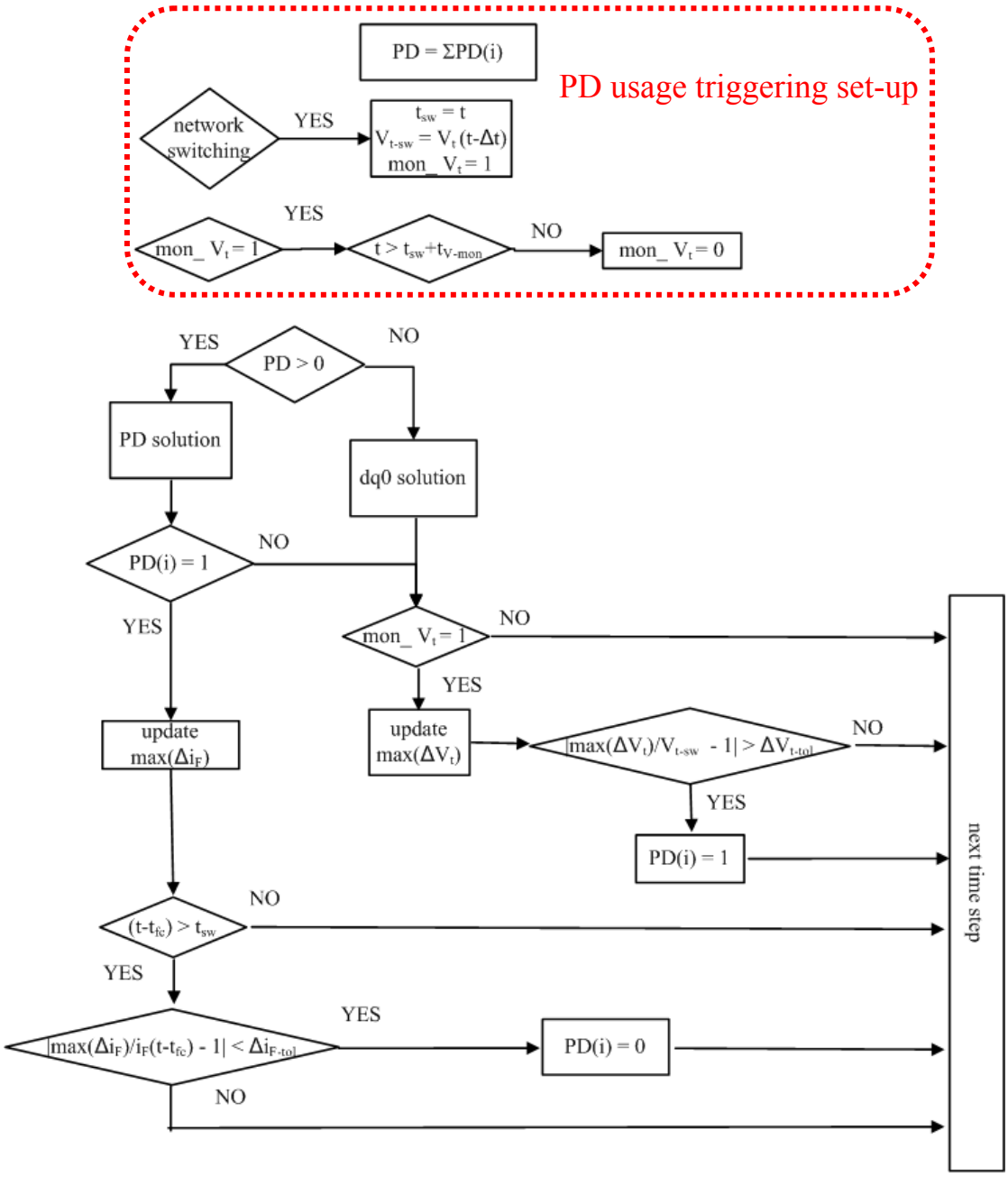

Figure 3.4 Solution algorithm for dq0-PD model

For typical transients, the PD (or VBR) model is expected to become active only for a small portion of the complete simulation interval. Hence, this approach is expected to provide PD (or VBR) model accuracy while maintaining dq0 computational speed.

3.7. Discrete Time PD-dq0 Model

This model combines the accuracy of the PD model with the efficiency of the dq0 model. It is obtained by applying Park's transformation to the discretized equations of the PD model, hence provides PD model like precision. Similar to the dq0 model, a prediction-correction scheme is implemented for interfacing with MNE through a constant admittance matrix found from the TE circuit of the machine. Constant admittance matrix usage eliminates the time consuming refactoring of the MNE coefficient matrix, hence provides dq0 model like computational efficiency.

Similar to the dq0 model, this model also contains predicted stator currents for interfacing with MNE through a constant admittance matrix. Therefore, damping resistance usage might be required in some cases to provide the desired model stability. With damped trapezoidal integration rule, discretized equations for the PD model given in (3.27) - (3.30) become

$$\begin{bmatrix} \mathbf{v_s} \\ \mathbf{v_r} \end{bmatrix} = -\begin{bmatrix} \mathbf{R_{ss}}(\theta) & \mathbf{R_{sr}}(\theta) \\ \mathbf{R_{rs}}(\theta) & \mathbf{R_{rr}} \end{bmatrix} \begin{bmatrix} \mathbf{i_s} \\ \mathbf{i_r} \end{bmatrix} - k' \begin{bmatrix} \boldsymbol{\lambda}_{\mathbf{sk}} \\ \boldsymbol{\lambda}_{\mathbf{rk}} \end{bmatrix} + \begin{bmatrix} \mathbf{h_s} \\ \mathbf{h_r} \end{bmatrix} \tag{3.62}$$

where

$$\begin{bmatrix} \mathbf{R_{ss}}(\theta) & \mathbf{R_{sr}}(\theta) \\ \mathbf{R_{rs}}(\theta) & \mathbf{R_{rr}} \end{bmatrix} = \begin{bmatrix} \mathbf{R_s} + k' \mathbf{L_{ss}}(\theta) & k' \mathbf{L_{sr}}(\theta) \\ k' \mathbf{L_{rs}}(\theta) & \mathbf{R_r} + k' \mathbf{L_{rr}} \end{bmatrix} \tag{3.63}$$

$$\mathbf{h_s} = -\alpha \, \mathbf{R_s} \, \hat{\mathbf{i}}_\mathbf{s} + k' \hat{\boldsymbol{\lambda}}_\mathbf{s} - \alpha \, \hat{\mathbf{v}}_\mathbf{s} \tag{3.64}$$

$$\mathbf{h_r} = -\alpha \, \mathbf{R_r} \, \hat{\mathbf{i}}_\mathbf{r} + k' \hat{\boldsymbol{\lambda}}_\mathbf{r} - \alpha \, \hat{\mathbf{v}}_\mathbf{r} \tag{3.65}$$

For the Backward Euler solution with $\Delta t/2$ simulation time step, α and k' in equations (3.62)-(3.65) are set to zero and $2/\Delta t$ respectively. By applying Park's transformation to (3.62) (see (2.12)),

$$\begin{bmatrix} \mathbf{v_{dqo}} \\ \mathbf{v_r} \end{bmatrix} = -\begin{bmatrix} \mathbf{R_{dq0ss}} & \mathbf{R_{dq0sr}} \\ \mathbf{R_{dq0rs}} & \mathbf{R_{rr}} \end{bmatrix} \begin{bmatrix} \mathbf{i_{dqo}} \\ \mathbf{i_r} \end{bmatrix} - k' \begin{bmatrix} \boldsymbol{\lambda}_{\mathbf{dqok}} \\ \boldsymbol{\lambda}_{\mathbf{rk}} \end{bmatrix} + \begin{bmatrix} \mathbf{P}^{-1}(\theta)\,\mathbf{h_s} \\ \mathbf{h_r} \end{bmatrix} \qquad (3.66)$$

The resulting resistance matrix in (3.66) is time independent as the resistance matrix of the discrete dq0 model given in (3.11). Unlike the discretized equation (3.11) of the dq0 model, the stator history terms in (3.66) given by (3.64) are functions of past phase variables ($\hat{\mathbf{v}}_\mathbf{s}$, $\hat{\mathbf{i}}_\mathbf{s}$ and $\hat{\boldsymbol{\lambda}}_\mathbf{s}$). Contrary to the discrete dq0 model, (3.66) allows to avoid past and present speed voltages $\mathbf{u}$ and maintain increased accuracy over the dq0 model.

Matrix reduction is applied to (3.66) for finding the TE formulation of (3.15). The $\mathbf{R_{dq0}}$ matrix remains the same as in (3.16). The Thevenin voltages become

$$\mathbf{e_{dq0}} = \mathbf{R_{dqosr}}\,\mathbf{R_{rr}^{-1}}\left(k'\,\boldsymbol{\lambda}_{\mathbf{rk}} + \mathbf{v_r} - \mathbf{h_r}\right) - k'\,\boldsymbol{\lambda}_{\mathbf{dqok}} + \mathbf{P}^{-1}(\theta)\mathbf{h_s} \qquad (3.67)$$

In order to insert a time independent and symmetric admittance matrix into the MNE, the Thevenin resistance matrix given in equation (3.18) is also applied to this model. The $\mathbf{e_{dq0}}$ voltages in (3.67) are adjusted through equation (3.19) with the predicted fictitious d and q-axis winding currents.

According to (3.64), the history term $\mathbf{h_s}$ in (3.66) and (3.67) is a function of $\hat{\mathbf{v}}_\mathbf{s}$, $\hat{\mathbf{i}}_\mathbf{s}$ and $\hat{\boldsymbol{\lambda}}_\mathbf{s}$. $\hat{\mathbf{v}}_\mathbf{s}$ is available from the solution of MNE. The vectors $\hat{\mathbf{i}}_\mathbf{s}$ and $\hat{\boldsymbol{\lambda}}_\mathbf{s}$ can be calculated from $\hat{\mathbf{i}}_\mathbf{dq0}$ and $\hat{\boldsymbol{\lambda}}_\mathbf{dq0}$ respectively, using the park's transformation matrix $\mathbf{P}(\theta)$.

The NE of the machines obtained from TE in (3.15) are inserted into the MNE after transforming back to phase coordinates. The solution of the MNE gives the stator voltages in phase variables $\mathbf{v_s}$. The stator voltages in dq0 variables $\mathbf{v_{dqo}}$ can be found using (2.12). The stator currents in dq0 variables $\mathbf{i_{dqo}}$ can be found using (3.22). From (3.62), the rotor currents $\mathbf{i_r}$ can be found as

$$\mathbf{i_r} = \mathbf{R_{rr}^{-1}}\left(-\mathbf{R_{dq0rs}}\,\mathbf{i_{dqo}} - k'\,\boldsymbol{\lambda}_{\mathbf{rk}} - \mathbf{v_r} + \mathbf{h_r}\right) \tag{3.68}$$

In solid rotor case, $\boldsymbol{\lambda}_{\mathbf{rk}}$ in (3.68) contains predicted saturation dependent variables λ_{kdj} and λ_{kqj}. Therefore, (3.68) is solved using an iterative approach with (3.21). This iterative solution process provides corrected values for λ_{kdj} and λ_{kqj} and the rotor currents $\mathbf{i_r}$. In the salient pole case, $\boldsymbol{\lambda}_{\mathbf{rk}}$ does not contain predicted values for λ_{kdj} and λ_{kqj}, hence calculation of rotor currents does not require iterations. After calculation of $\mathbf{i_r}$, λ_{kdj} and λ_{kqj}, the flux linkages ($\boldsymbol{\lambda}_{\mathbf{dqo}}$ and $\boldsymbol{\lambda}_{\mathbf{r}}$) can be found by using (2.70). The stator currents and flux linkages in phase variables ($\mathbf{i_s}$ and $\boldsymbol{\lambda}_{\mathbf{s}}$) can be calculated from $\mathbf{i_{dqo}}$ and $\boldsymbol{\lambda}_{\mathbf{dqo}}$ using (2.12).

The sequence of calculation steps is briefly described below:

1. predict ω and θ (see (3.6) and (3.7)) to calculate $\mathbf{P}(\theta)$;
2. predict electrical variables to calculate $\mathbf{e_{dq0}}$ (see (3.67) and (3.19)) and build the TE in (3.15);
3. solve the MNE to find $\mathbf{v_s}$;
4. find $\mathbf{v_{dqo}}$ from $\mathbf{v_s}$ using (2.12) and use (3.22) for stator currents $\mathbf{i_{dqo}}$;

5. find rotor currents using (3.68);

6. find λ_{ad} and λ_{aq} using (2.63) and (2.64), use (3.21) for correcting λ_{kdj} and λ_{kqj};

7. compare predicted and corrected values for λ_{kdj} and λ_{kqj}, repeat step 5 to 7 with corrected $\boldsymbol{\lambda}_{\mathbf{rk}}$ and if no convergence;

8. check for the machine operating segment on saturation curve, if the operating segment needs to change
   - update $\mathbf{L}_{\mathbf{dq0}}$ with updated L_{ad} and L_{aq} values (see (2.73) - (2.75))
   - update λ_{kdj} and λ_{kqj} with updated λ_{kj} value (see (3.21)),
   - recalculate λ_{ad} and λ_{aq} using (2.63) and (2.64),
   - switch solution method to Backward Euler for the next time step;

9. find $\boldsymbol{\lambda}_{\mathbf{dqo}}$ and $\boldsymbol{\lambda}_{\mathbf{r}}$ using (2.70);

10. find stator currents and flux linkages in phase variables ($\mathbf{i}_{\mathbf{s}}$ and $\boldsymbol{\lambda}_{\mathbf{s}}$) from $\mathbf{i}_{\mathbf{dqo}}$ and $\boldsymbol{\lambda}_{\mathbf{dqo}}$ using (2.12); find electromagnetic torque using (2.20) and solve the mechanical equations (3.1) and (3.2) to find $\boldsymbol{\theta}_{\mathbf{m}}$ and $\boldsymbol{\omega}_{\mathbf{m}}$;

11. compare predicted and corrected ω, repeat the steps 4-9 if no convergence;

12. return to step 1 for the next time point solution.

The above solution procedure is for solid rotor machine. In the salient pole case, the solution procedure does not contain prediction and correction of λ_{kdj} and λ_{kqj}. Hence, prediction of λ_{kdj} and λ_{kqj} is not performed in step 2, and steps 6 and 7 does

not exist. The operating segment on the saturation curve is found (in step 8) with the same procedure as in the dq0 model.

CHAPTER 4.

STUDIES FOR NUMERICAL PRECISION – EMTP-RV SIMULATIONS

The models presented in CHAPTER 3 are implemented and tested through user-defined modeling facilities in EMTP-RV with automatic initialization from load-flow and steady-state solutions. In order to study the effect of machine models on simulation accuracy, balanced and unbalanced faults are simulated first in a simple single-machine infinite bus system and then for practical case studies with several synchronous machines. The first practical case is a typical transient stability case and the second practical case is used to determine the potential for subsynchronous resonance (SSR) transient torque amplification.

It should be emphasized that numerical errors depend on simulation time step, the simulated network, fault location, fault type, and fault occurrence and clearing timings. That is why several tests must be performed before concluding on the precision of a given model.

The reference solutions for precision comparisons are obtained with PD model and $1\,\mu s$ simulation time step (Δt) [21]. The simulations are repeated for all models for the simulation time steps $50\,\mu s$-$1\,ms$. In order to evaluate the accuracy of different numerical solutions, the relative error between the reference solution trajectory (f) and the given numerical solution ($\tilde{f}$) is calculated using the 2-norm as explained in Section 1.3.

Although electromechanical transients are studied in all cases, the relative error is calculated not only for the electrical torque but also for the machine armature currents. It should be noted that, the errors in armature currents are different for each phase and the

highest is presented in this thesis. In order to demonstrate the effects of power system model on machine modeling precision, the errors in armature currents are also presented for simple single-machine infinite bus cases in addition to the errors in electrical torque.

In the classical dq0, PD-dq0, dq0-IITS, dq+PD and dq+VBR models, $\alpha = 1$ (zero damping) unless the opposite is stated. The effect of damping resistances on the simulation accuracy is investigated only for the practical transient stability case study.

4.1.Single Machine - Infinite Bus System

The single line diagram of the studied system is shown in Figure 4.1 with the related load-flow constraints. F1 and F2 are the fault switches. CB1 and CB2 are the line circuit breakers that operate to clear the applied fault. The simulated fault cases are summarized in Table 4.1. In all cases the fault is applied at 0.02 s, the line circuit breakers CB1 and CB2 operate with 200 ms (testing purposes) delay following the fault. The simulation interval is 1s. The system data can be found in Appendix IV. It should be noted that, this case has been created from a practical network. Although it is a single machine case, it is more practical than the one used in [26]. Machine controls and network effects are included for the assessment of numerical accuracy.

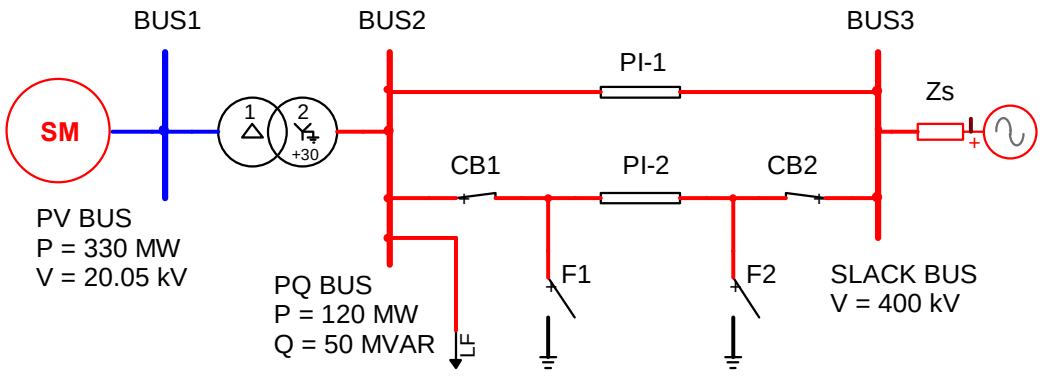

Figure 4.1 Single line diagram of the simple single-machine system

Table 4.1 Single Machine - Infinite Bus Cases

Test Case	Fault Location	Fault Type	Machine Saturation	Transmission Line Model	Transformer Saturation
C1	F1	3-ph	Not modeled	Multi-phase PI Section	Not modeled
C2	F2	3-ph	Not modeled	Multi-phase PI Section	Not modeled
C3	F1	1-ph	Not modeled	Multi-phase PI Section	Not modeled
C4	F1	3-ph	Modeled	Multi-phase PI Section	Not modeled
C5	F1	3-ph	Modeled	Distributed Parameter	Not modeled
C6	F1	3-ph	Modeled	Distributed Parameter	Modeled

4.1.1. Test Case C1

The maximum errors in machine armature currents for dq0, dq0 with network iterative scheme (dq0-IT) and dq0-IITS are presented in Table 4.2. The relative tolerance value for dq0-IT is 10^{-6}. The parameters for intermediate time step usage in the dq0-IITS model are $\Delta V_{t-tol} = 5\%$, $t_{V-mon} = 3\,s$ and $\Delta i_{F-tol} = 10\%$. Although the accumulated prediction errors of dq0 are eliminated in dq0-IT, the improvement in accuracy is not significant. Therefore, dq0 is more efficient compared to dq0-IT, due to its lower computational cost. However, dq0-IT eliminates the requirement of damping resistances and can consequently provide stability and precision. dq0-IT has been used here to demonstrate the prediction qualities of dq0 and abandoned for the following tests.

Table 4.2 Error e%, Armature Currents, Test Case C1

Δt	dq0	dq0-IT	dq0-IITS ($\Delta t_i = \Delta t/2$)	dq0-IITS ($\Delta t_i = \Delta t/4$)	dq0-IITS ($\Delta t_i = \Delta t/8$)
50μs	0.0315	0.0315	0.0171	0.0144	0.0138
100μs	0.1264	0.1264	0.0663	0.0493	0.0460
200μs	0.5120	0.509	0.1742	0.1411	0.1313
500μs	3.6715	3.6694	1.1201	0.8613	0.8048
1000μs	13.6521	13.6232	4.8911	2.6812	2.2485

The reference solution waveform for the phase-a current is shown in Figure 4.2. The differences between the reference solution and the solutions with $\Delta t = 500\mu s$ for dq0, PD, VBR, dq0-IITS ($\Delta t_i = \Delta t/8$), dq+PD, dq+VBR, PD-dq0 are presented in

Figure 4.3. The solution for dq0 is also shown with $\Delta t = 200\mu s$. The waveforms of dq+PD and PD-dq0 models are superimposed with the PD model. The waveform with the dq+VBR model is also practically undistinguishable from VBR model. This is also confirmed in Table 4.3. It should be noted that, the tolerance values for dq+PD and dq+VBR models are the same as with the dq0-IITS model.

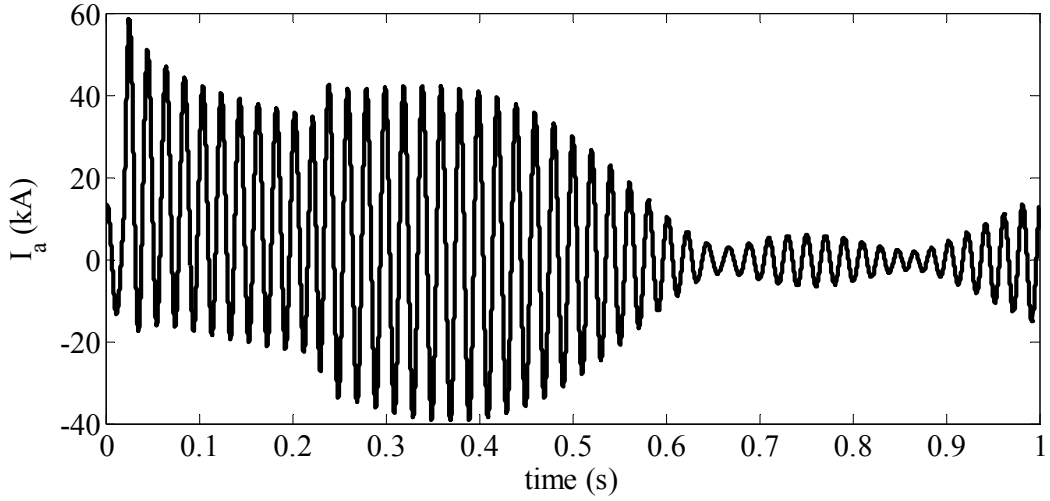

Figure 4.2 Reference waveform for phase-a current, Test Case C1

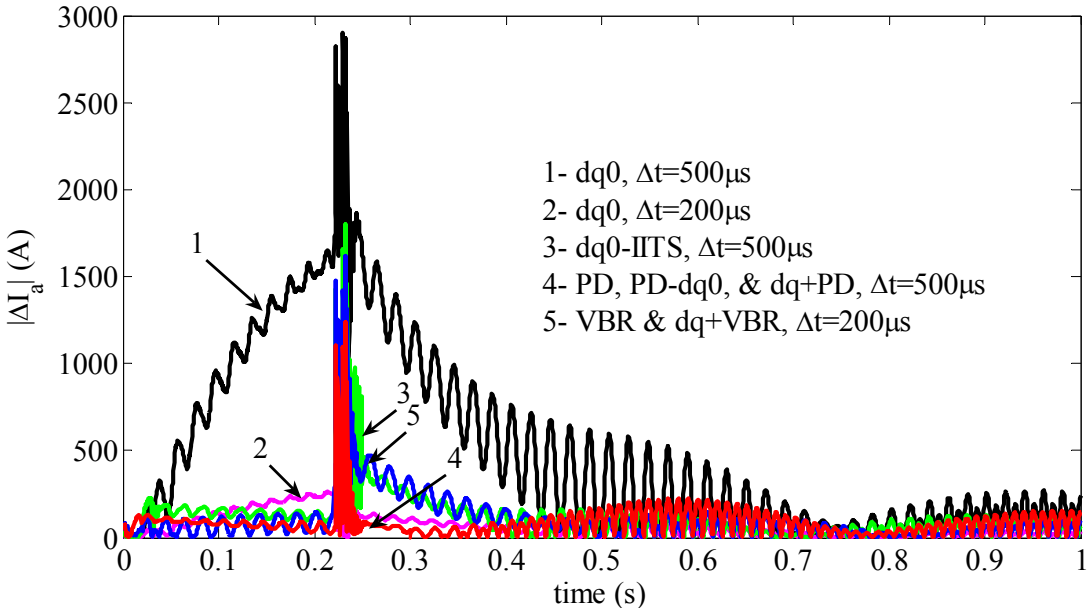

Figure 4.3 Differences between the numerical solutions and the reference waveform for phase-a currents, Test Case C1

Table 4.3 Error e%, Armature Currents, Test Case C1

Δt	dq0	dq0-IITS ($\Delta t_i = \Delta t/8$)	PD	PD-dq0	dq+PD	VBR	dq+VBR
50μs	0.0315	0.0138	0.0125	0.0125	0.0125	0.0117	0.0117
100μs	0.1264	0.0460	0.0418	0.0418	0.0421	0.0409	0.0414
200μs	0.5120	0.1313	0.1576	0.1576	0.1596	0.1497	0.1527
500μs	3.6715	0.8048	0.8081	0.8091	0.8271	0.8505	0.8680
1000μs	13.6521	2.2485	3.3525	3.3545	3.4345	3.2004	3.308

It is apparent from Figure 4.3 that both PD and VBR models are very accurate especially during the fault interval, even with large time steps. As the fault period is simulated more accurate with these models, the precision is also much better compared to dq0 model for the rest of the simulation period. As seen in Figure 4.3, when Δt is increased, classical dq0 model introduces significant errors especially in the DC component of armature currents following the fault. This error is reduced in dq0-IITS dq+PD and dq+VBR models by switching to a more accurate model or solution procedure. dq+PD and dq+VBR models utilize PD and VBR models during this period and provide similar accuracy with PD and VBR models. The accuracy of dq0-IITS depends on utilized internal intermediate time steps (Δt_i). The reduction of Δt_i improves accuracy further. On the other hand, as the stator voltages in dq0 representation obtained from the MNE solution are linearly interpolated for the intermediate time point machine equation solution, this improvement has a limit. The existence of such limit can be seen from Table 4.2. The results in Table 4.3 demonstrate that the performance of the dq0-IITS model is comparable to that of the most precise models. As this case contains a single machine and, dq0-IITS, dq+PD and dq+VBR models have same tolerance values, the more accurate model usage period is the same for those models and less than 0.3s as illustrated in Figure 4.4.

As the PD-dq0 is identical to discretized PD model, it provides similar accuracy with PD model as illustrated in Table 4.3. Like the classical dq0 model, predicting certain electrical variables in the PD-dq0 model does not deteriorate accuracy.

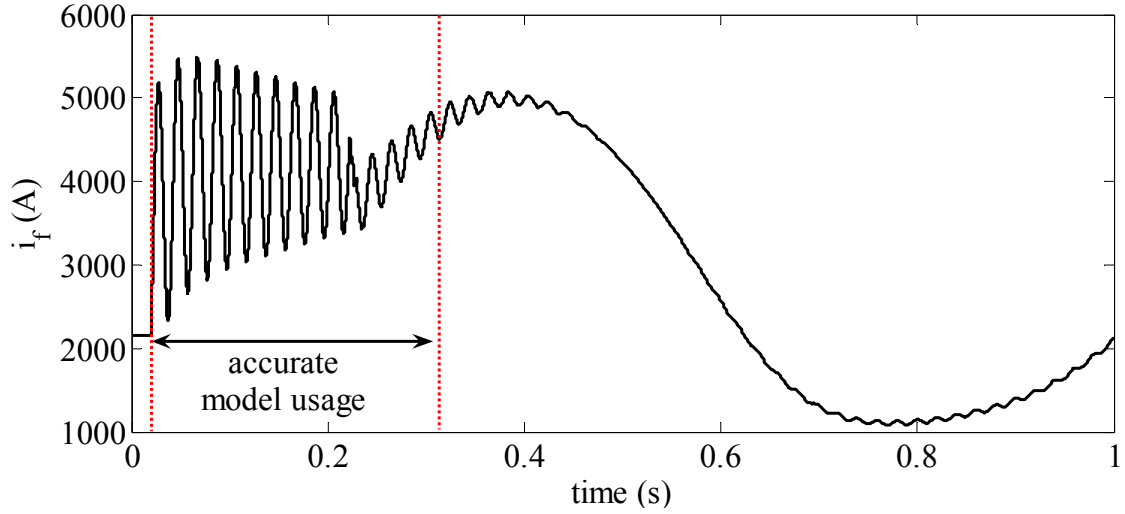

Figure 4.4 Accurate model usage period in dq0-IITS, dq+PD and dq+VBR models, Test Case C1

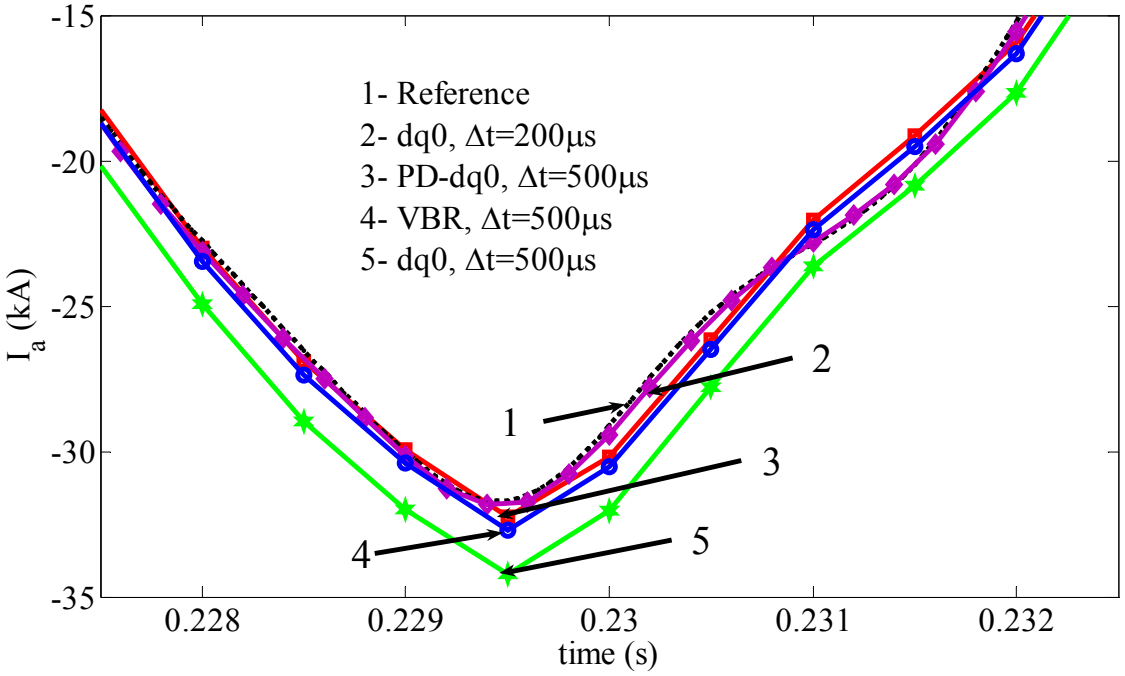

Figure 4.5 Phase-a currents during fault removal, Test Case C1

According to Figure 4.3, during the fault interval, all models with $\Delta t = 500\mu s$ are more accurate than dq0 with $\Delta t = 200\mu s$. However, the errors in the computations of

high frequency transients resulting from fault removal increase with increasing Δt and this makes dq0 with $\Delta t = 200\mu s$ more accurate for the rest of the simulation. The effect of inaccurate simulation of high frequency transients due to large Δt usage is also demonstrated in Figure 4.5. In addition, as illustrated in Figure 4.6, ideal switch based fault clearing times may introduce errors when Δt increases and may reduce the simulation accuracy further.

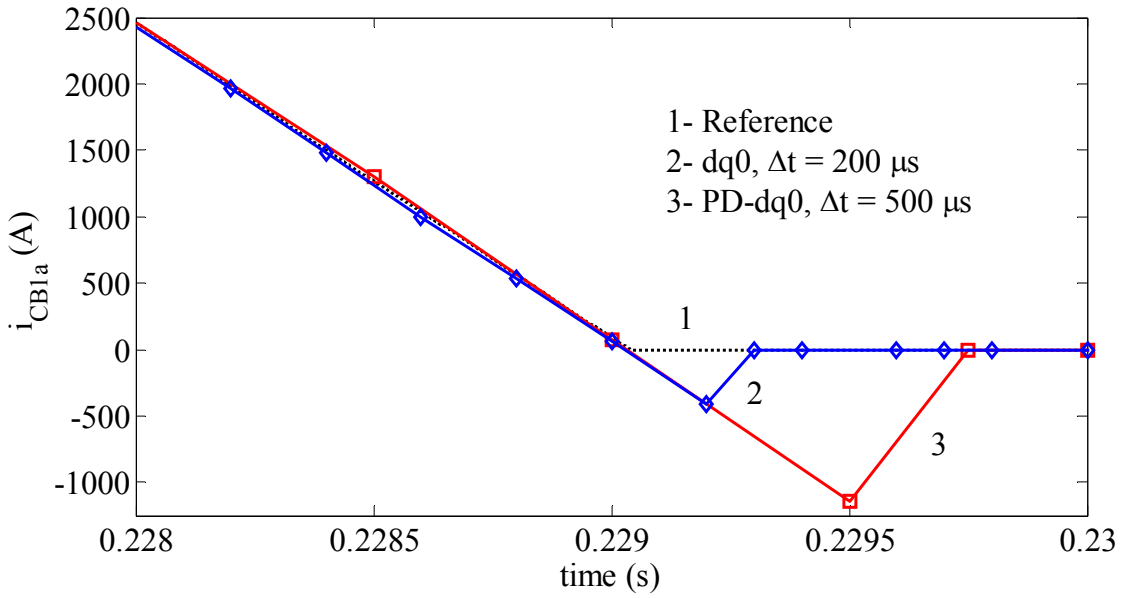

Figure 4.6 Time delay in switch opening due to large time step usage, Test Case C1

The errors for the 0 to 0.22 s interval (initialization and fault interval) are explicitly presented in Table 4.4 for dq0 and PD-dq0 models. Table 4.4 also illustrates the errors for the three-phase-to-ground fault applied directly to machine terminals (BUS1 in Figure 4.1).

Table 4.4 Error e%, Armature Currents, Test Case C1 (0 to 0.22 s only)

Δt	dq0	dq0*	PD-dq0	PD-dq0*
50μs	0.0398	0.0783	0.0046	0.0032
100μs	0.161	0.3217	0.0155	0.0107
200μs	0.646	1.3019	0.0649	0.045
500μs	4.6774	8.8309	0.3755	0.2602
1000μs	16.3618	37.243	1.9659	1.163

* Three-phase-to-ground fault at BUS1 in Figure 4.1

It is apparent from Table 4.4 that the dq0 model is significantly less accurate for faults applied directly to the machine terminals. As the impedance between the machine terminals and the fault reduces, the dq0 model requires a significantly reduced Δt to compensate for its precision deterioration. On the other hand, in practical cases the majority of faults involve the transmission system, and therefore the transmission system should be accounted for in precision assessment. However, as with PD and VBR models, the PD-dq0 model simulates the fault conditions very accurately in all cases.

Although some machine models can maintain precision with large Δt values, in EMT-type simulations the usage of such values encounters several limitations. As indicated above, when Δt increases the precision in network equations decreases and particularly when high frequencies are involved. Another important aspect is the treatment of nonlinear models. This test case does not involve nonlinear models, such as transformer saturation. In addition using more precise propagation delay based models for transmission lines instead of multi-phase pi section models impose a hard upper limit on simulation time step.

It should be noted that, large time steps also create initialization errors and discrepancies with the steady-state phasor solution. In order to eliminate the initialization error effect, the actually studied disturbance should be applied when the system is in complete steady-state. However, usual practice is to put 1 - 2 cycle time margin and this margin may not be sufficient while utilizing large time steps as illustrated in Figure 4.7.

The reference solution waveform for the electrical torque is shown in Figure 4.8. The differences between the reference solution and the solutions with $\Delta t = 500 \mu s$ for dq0, PD, VBR, dq0-IITS ($\Delta t_i = \Delta t / 8$), dq+PD, dq+VBR, PD-dq0 are presented in Figure 4.9. The waveforms of dq+PD and PD-dq0 models are superimposed with the PD model. The waveform with dq+VBR model is also practically undistinguishable from VBR model. This is also confirmed in Table 4.5. As seen from Figure 4.9 and Table 4.5,

errors in electrical torque have a similar characteristic with the errors in armature currents. It should be noted that, errors in armature currents are different for each phase and the highest errors are presented in Table 4.4. Hence, the errors in electrical torque presented in Table 4.5 are lower compared to armature current errors in Table 4.4. However, it is observed that, the errors in electrical torque are close to the average of phase armature current errors.

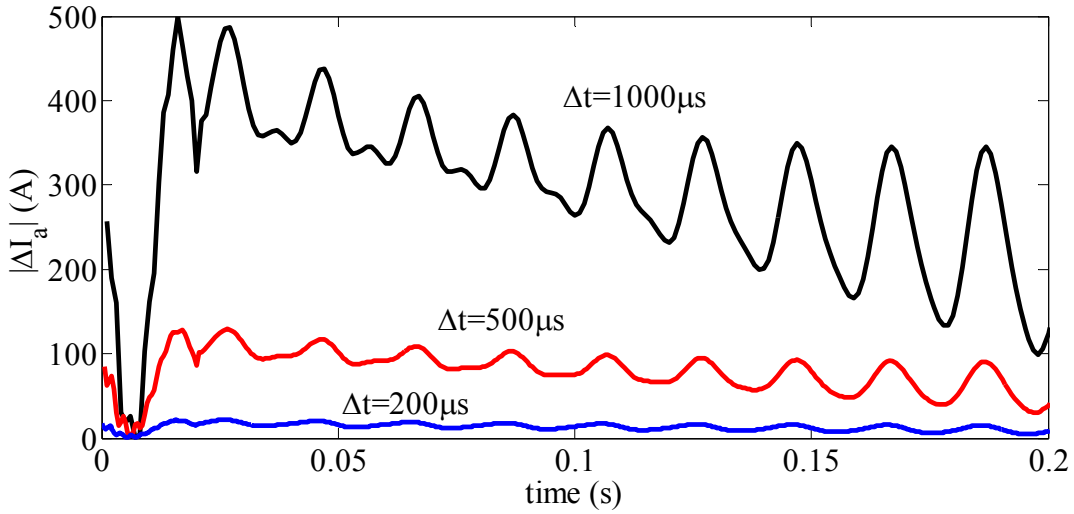

Figure 4.7 The effect of utilized time step on simulation starting transient, Test Case C1, PD-dq0 model

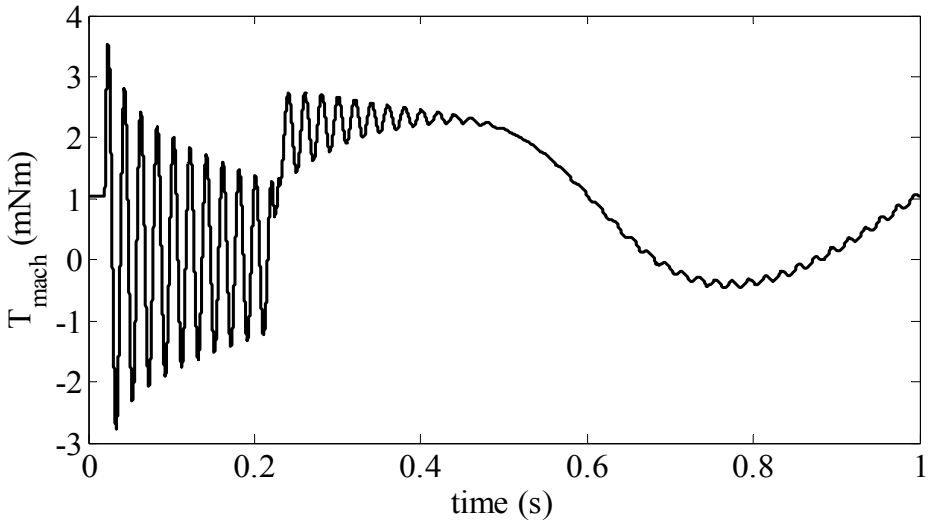

Figure 4.8 Reference waveform for electrical torque, Test Case C1

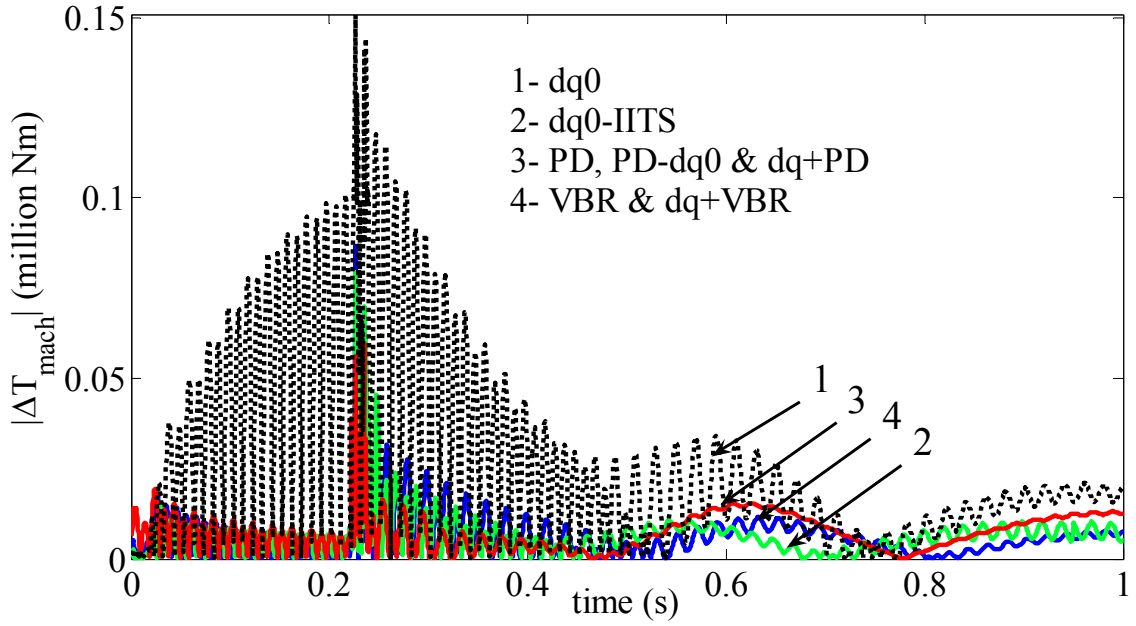

Figure 4.9 Differences between the numerical solutions and the reference waveform for electrical torque, Test Case C1

Table 4.5 Error e%, Electrical Torque, Test Case C1

Δt	dq0	dq0-IITS ($\Delta t_i = \Delta t/8$)	PD	PD-dq0	dq+PD	VBR	dq+VBR
50μs	0.0211	0.0118	0.0101	0.0101	0.0101	0.0090	0.0090
100μs	0.0846	0.0351	0.0322	0.0322	0.0323	0.0300	0.0300
200μs	0.3447	0.0903	0.1103	0.1104	0.1108	0.1083	0.1090
500μs	2.5408	0.6312	0.6319	0.6331	0.6431	0.6595	0.6711
1000μs	9.1937	2.1985	2.5886	2.5991	2.6744	2.3086	2.4108

4.1.2. Test Case C2

The errors in armature currents for the test case C2 are presented in Table 4.6. In test case C2, due to the fault location and the system model, the high frequency transients occur not only following fault removal, but also after fault occurrence, as illustrated in Figure 4.10. This causes reduced accuracy in the surrounding network solution and consequently the precisions for all models, except classical dq0, are reduced in Table 4.6. However, for the $\Delta t = 500\mu s$ and 1 ms time steps, the simulation errors in the high frequency transients following fault removal are much higher in C1 compared to C2 and this causes higher simulation errors for all models.

In the test case C2, the fault location is different and consequently the impedance between the machine terminals and the fault is different. That is why the dq0 model becomes more precise and simulates the DC component of armature currents more accurately.

Table 4.6 Error e%, Armature Currents, Test Case C2

Δt	dq0	dq0-IITS ($\Delta t_i = \Delta t/8$)	PD	PD-dq0	dq+PD	VBR	dq+VBR
50μs	0.0264	0.0191	0.0184	0.0184	0.0184	0.0181	0.0181
100μs	0.0974	0.0705	0.0671	0.0671	0.0671	0.0619	0.0619
200μs	0.3943	0.2411	0.2364	0.2364	0.239	0.2271	0.2303
500μs	2.2774	0.8771	0.9038	0.9041	0.9181	0.8225	0.8356
1000μs	7.8456	2.3810	2.9883	2.9904	3.0875	2.7429	2.8479

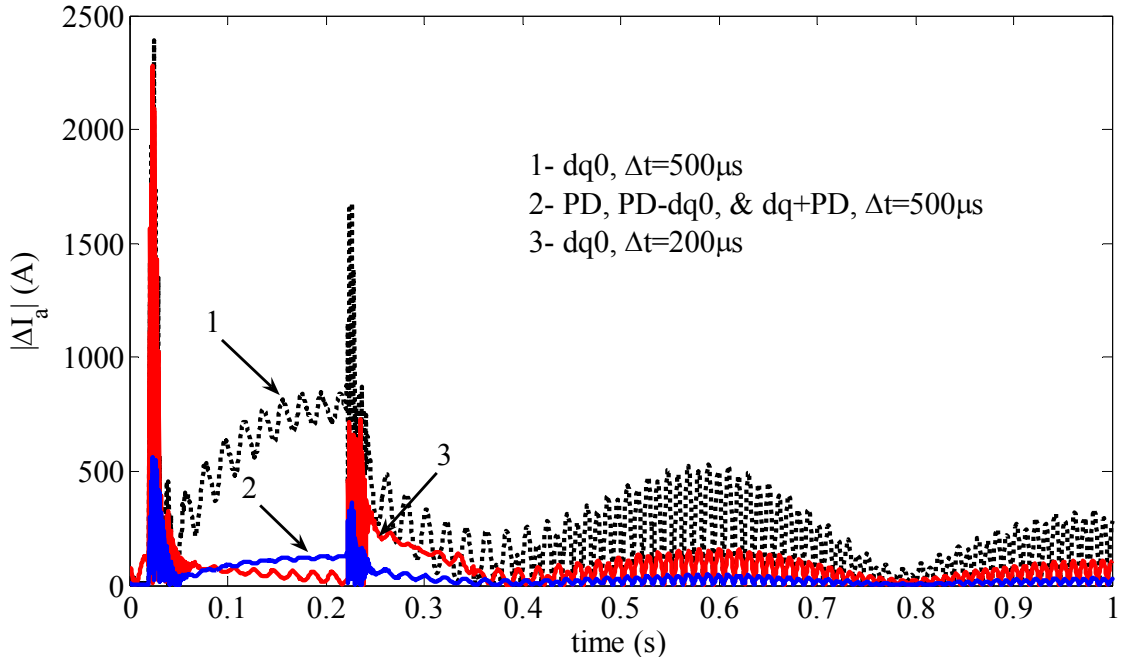

Figure 4.10 Differences between the numerical solutions and the reference waveform for phase-a currents, Test Case C2

The errors in electrical torque for the test case C2 are presented in Table 4.7. Similar to C1, the errors in electrical torque have a similar characteristic with the errors in armature currents.

Table 4.7 Error e%, Electrical Torque, Test Case C2

Δt	dq0	dq0-IITS ($\Delta t_i = \Delta t/8$)	PD	PD-dq0	dq+PD	VBR	dq+VBR
50μs	0.018	0.0147	0.0142	0.0142	0.0142	0.0137	0.0137
100μs	0.0687	0.0513	0.0508	0.0508	0.0508	0.0489	0.0489
200μs	0.2833	0.2015	0.1937	0.1937	0.1941	0.1830	0.1850
500μs	1.7246	0.6940	0.7041	0.7044	0.7065	0.6418	0.6471
1000μs	5.6758	1.7821	2.1763	2.1778	2.1831	1.9736	2.0377

4.1.3. Test Case C3

The errors in machine armature currents and electrical torque for the test case C3 are presented in Table 4.8 - Table 4.9, respectively.

Table 4.8 Error e%, Armature Currents, Test Case C3

Δt	dq0	dq0-IITS ($\Delta t_i = \Delta t/8$)	PD	PD-dq0	dq+PD	VBR	dq+VBR
50μs	0.0113	0.0113	0.0114	0.0114	0.0114	0.0113	0.0113
100μs	0.0867	0.0862	0.0865	0.0865	0.0865	0.0862	0.0862
200μs	0.3615	0.356	0.3612	0.3612	0.3612	0.3527	0.3527
500μs	1.5856	1.3132	1.136	1.1362	1.1406	1.081	1.091
1000μs	3.77	3.0173	2.6455	2.6497	2.6855	2.4167	2.4203

Table 4.9 Error e%, Electrical Torque, Test Case C3

Δt	dq0	dq0-IITS ($\Delta t_i = \Delta t/8$)	PD	PD-dq0	dq+PD	VBR	dq+VBR
50μs	0.0075	0.0075	0.0076	0.0076	0.0076	0.0074	0.0074
100μs	0.0581	0.0577	0.0579	0.0579	0.0579	0.0577	0.0577
200μs	0.2265	0.2271	0.2256	0.2256	0.2256	0.2239	0.224
500μs	1.2217	1.0068	0.8599	0.8603	0.8661	0.8324	0.8329
1000μs	2.8114	2.2488	1.8207	1.8241	1.8409	1.7621	1.7672

The errors for dq0 are now significantly smaller. The main reason is the smaller DC component in machine armature currents due to the fault occurrence time point. When this time point is shifted by 5 ms, the DC component increases as illustrated in Figure 4.11 and the accuracy of the dq0 model reduces as shown in Figure 4.12 and Figure 4.13. It should be noted that, the presence of transient DC stator currents does not

have a significant influence on the precision of the other machine models. Hence, the 5 ms shift in switching times does not affect the simulation accuracy for the other models.

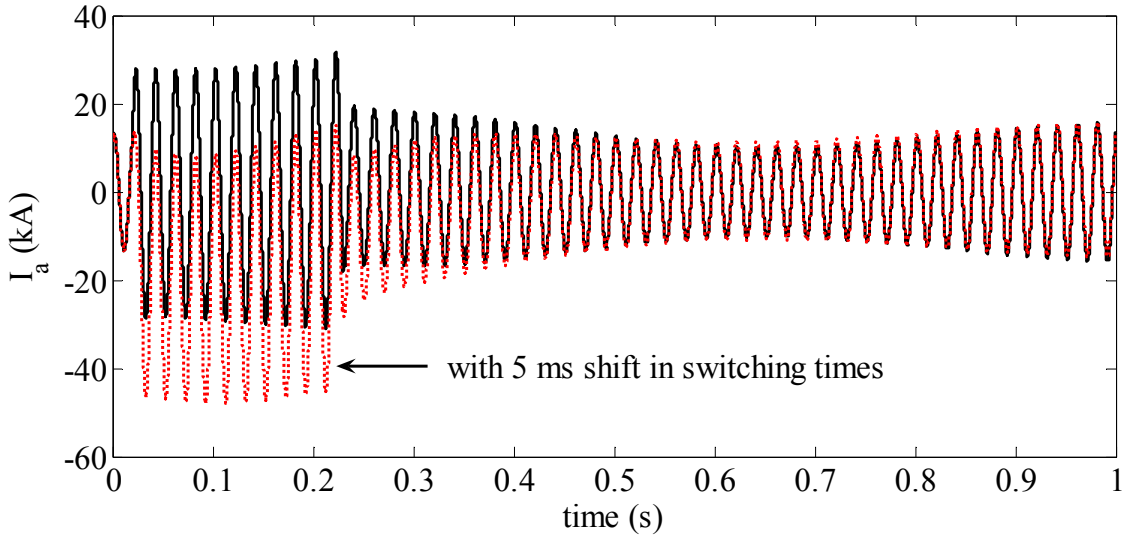

Figure 4.11 Effect of 5 ms shift in switching times on phase-a current (reference waveform) in Test Case C3

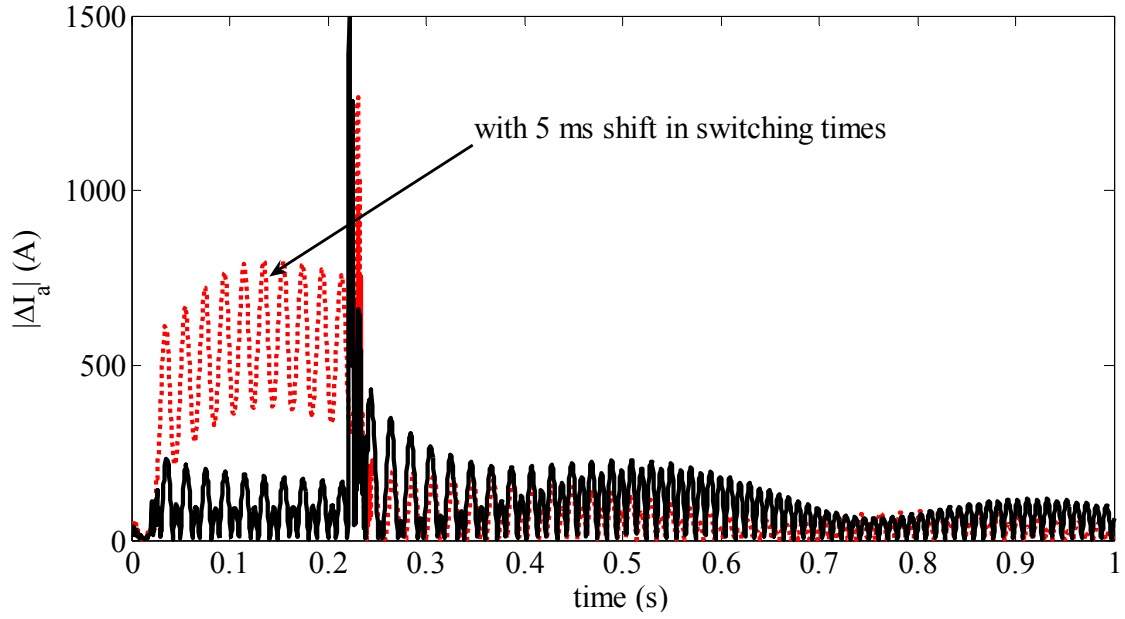

Figure 4.12 Effect of 5 ms shift in switching times on the difference between the numerical solution and the reference waveform of phase-a current for dq0 model with $\Delta t = 500\mu s$ in Test Case C3

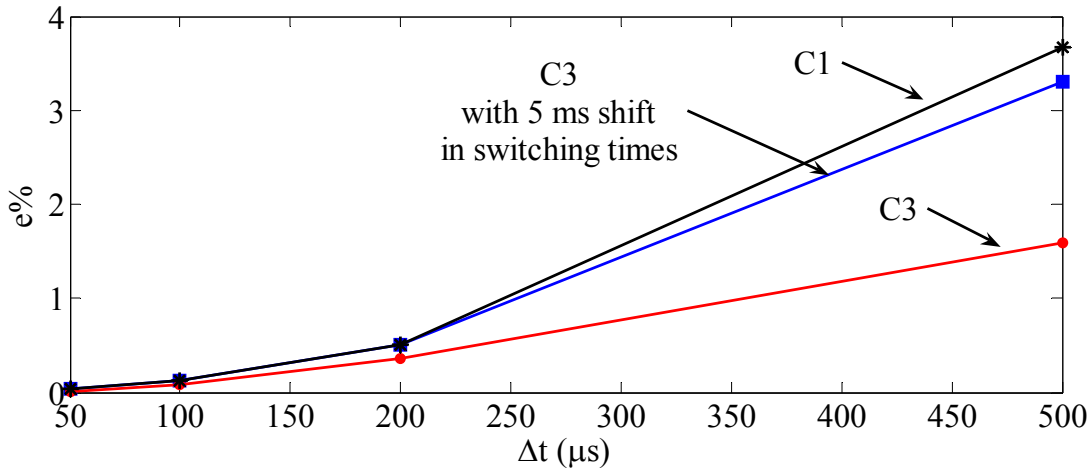

Figure 4.13 Effect of 5 ms shift in switching times on dq0 model armature current errors in Test Case C3

4.1.4. Test Case C4

The errors in armature currents and electrical torques for the test case C4 are presented in Table 4.10 and Table 4.11. The difference between the reference and the PD-dq0 model solution with $\Delta t = 500\mu s$ for the test cases C1 and C4 are presented in Figure 4.14. Operating segment changes in the saturation curve cause jumps in machine operating conditions in all machine models as illustrated in Figure 4.15.

When large time steps are used, a jump may take place far from the knee point and produce significant errors. This explains the increasing differences between error percentages given in Table 4.3 (Table 4.5) and Table 4.10 (Table 4.11) as Δt increases. In Figure 4.14, segment jump effects on simulation accuracy are more pronounced at 0.235 s, 0.605 s and 0.928 s.

It should be noted that, for a given Δt, when the saturation characteristic is represented with a larger number of linear segments, the differences between slopes of consecutive segments and between consecutive residual flux values become smaller. As a consequence, the segment jumps are expected to produce less error.

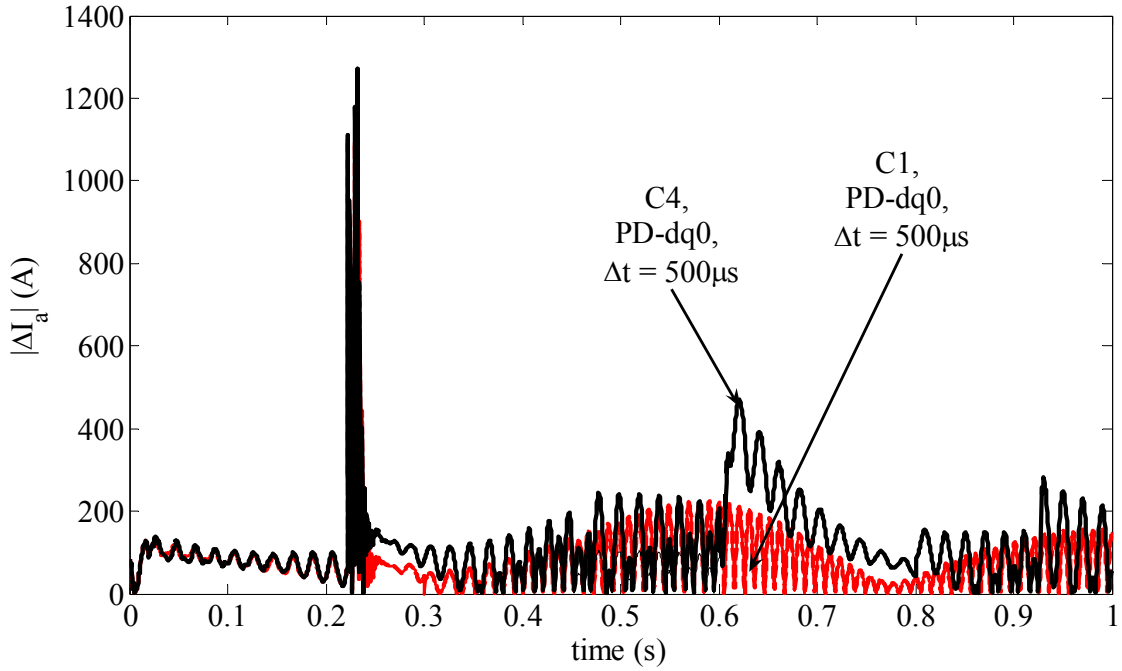

Figure 4.14 Differences between phase-a currents and the reference waveform for Test Cases C1 and C4, PD-dq0 model, $\Delta t = 500\mu s$

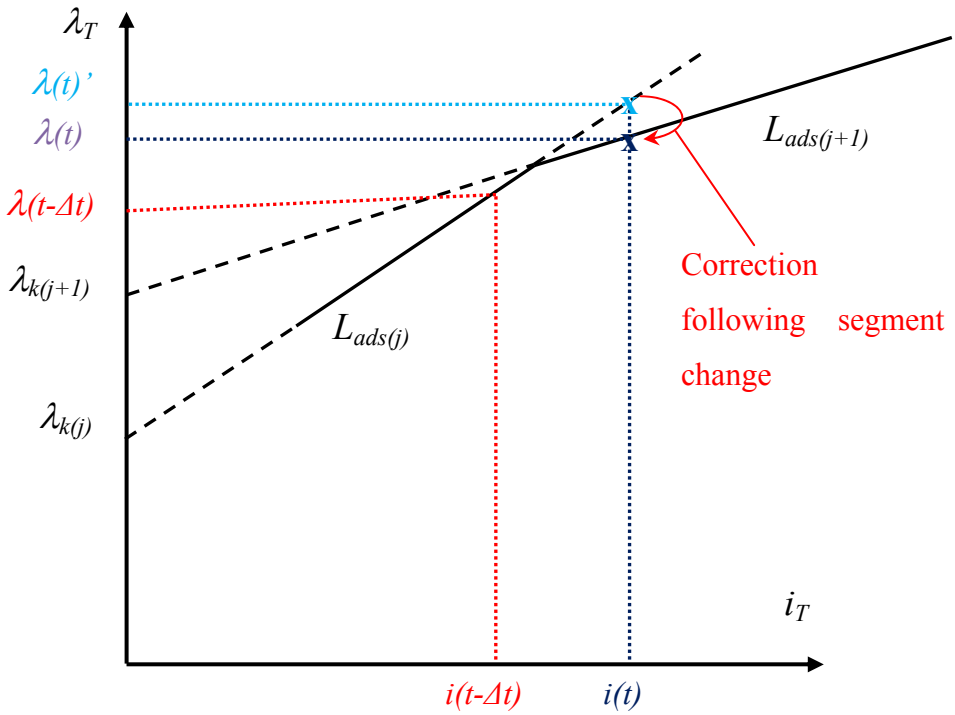

Figure 4.15 Jump in machine operating conditions due to operating segment change in the saturation curve

Table 4.10 Error e%, Armature Currents, Test Case C4

Δt	dq0	dq0-IITS ($\Delta t_i = \Delta t/8$)	PD	PD-dq0	dq+PD	VBR	dq+VBR
50μs	0.0357	0.0156	0.0141	0.0141	0.0142	0.0136	0.0136
100μs	0.1538	0.0558	0.0512	0.0512	0.0515	0.0504	0.0507
200μs	0.7008	0.1578	0.1928	0.1930	0.1959	0.1860	0.1890
500μs	4.6728	1.1303	1.1371	1.1380	1.1882	1.2216	1.2338
1000μs	17.806	3.0783	4.4426	4.4441	4.5581	4.3507	4.4793

Table 4.11 Error e%, Electrical Torque, Test Case C4

Δt	dq0	dq0-IITS ($\Delta t_i = \Delta t/8$)	PD	PD-dq0	dq+PD	VBR	dq+VBR
50μs	0.0245	0.0145	0.0134	0.0134	0.0135	0.0129	0.0129
100μs	0.1039	0.0432	0.0399	0.0399	0.0402	0.0367	0.0367
200μs	0.479	0.1125	0.1349	0.135	0.1361	0.1346	0.135
500μs	3.3558	0.8935	0.8897	0.8911	0.9239	0.9473	0.954
1000μs	12.017	2.6042	3.4371	3.4434	3.5494	3.2384	3.2844

4.1.5. Test Case C5

The errors in armature currents and electrical torques for the test case C5 are presented in Table 4.12 and Table 4.13. Distributed constant parameter model usage for transmission lines imposes a hard upper limit on Δt, therefore the simulations with $\Delta t = 500\mu s$ and $\Delta t = 1ms$ cannot be performed. The difference between the reference and the PD-dq0 model solutions with $\Delta t = 200\mu s$ for the test cases C1 and C5 are presented in Figure 4.16. As seen from Figure 4.16, the difference in error percentages given in Table 4.10 (Table 4.11) and Table 4.12 (Table 4.13) is resulting from both different segment jump effect in machine operating point on saturation curve and the selected transmission line model. In this case, the distributed constant parameter transmission line model usage slightly improves the precision as it improves the accuracy in the computation of high frequency transients resulting from fault removal.

Table 4.12 Error e%, Armature Currents, Test Case C5

Δt	dq0	dq0-IITS ($\Delta t_i = \Delta t/8$)	PD	PD-dq0	dq+PD	VBR	dq+VBR
50μs	0.0335	0.0149	0.0136	0.0136	0.0136	0.0132	0.0132
100μs	0.1421	0.0518	0.0486	0.0486	0.0488	0.0481	0.0479
200μs	0.6671	0.1475	0.1793	0.1795	0.1831	0.1751	0.1819

Table 4.13 Error e%, Electrical Torque, Test Case C5

Δt	dq0	dq0-IITS ($\Delta t_i = \Delta t/8$)	PD	PD-dq0	dq+PD	VBR	dq+VBR
50μs	0.0231	0.0139	0.013	0.013	0.013	0.0127	0.0127
100μs	0.0958	0.0411	0.0385	0.0385	0.0387	0.0355	0.0356
200μs	0.4589	0.1084	0.1286	0.1288	0.1309	0.1284	0.1296

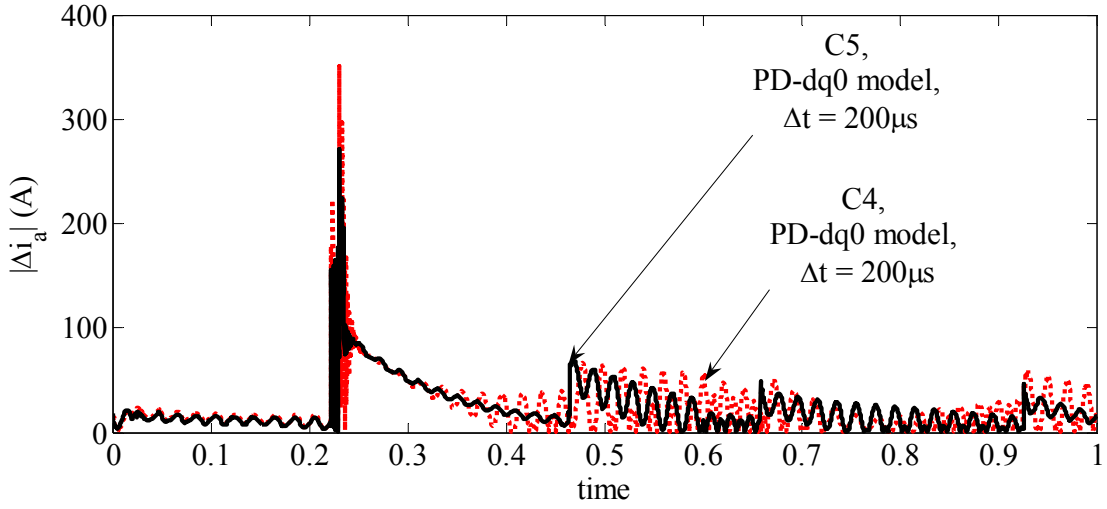

Figure 4.16 Differences between phase-a currents and the reference waveform for Test Cases C1 and C5, PD-dq0 model, $\Delta t = 200\mu s$

4.1.6. Test Case C6

The errors in armature currents and electrical torques for the test case C6 are presented in Table 4.14 and Table 4.15. As seen from Table 4.12 - Table 4.15, modeling transformer saturation causes a significant decrease in simulation precision for all models. It should be noted that, accurate simulation of transformer saturation characteristics requires small time step usage. Following fault removal, the transformer magnetizing branch enters its saturated region and the utilized time steps are not sufficiently small for accurate simulation of the saturation characteristics as illustrated in Figure 4.17 and Figure 4.18. As a result, the simulation precision decreases dramatically and independently from the machine model. This can be also seen in clearly in Figure 4.19 which presents the difference between the reference and the PD-dq0 model solutions with $\Delta t = 200\mu s$ for the test cases C5 and C6.

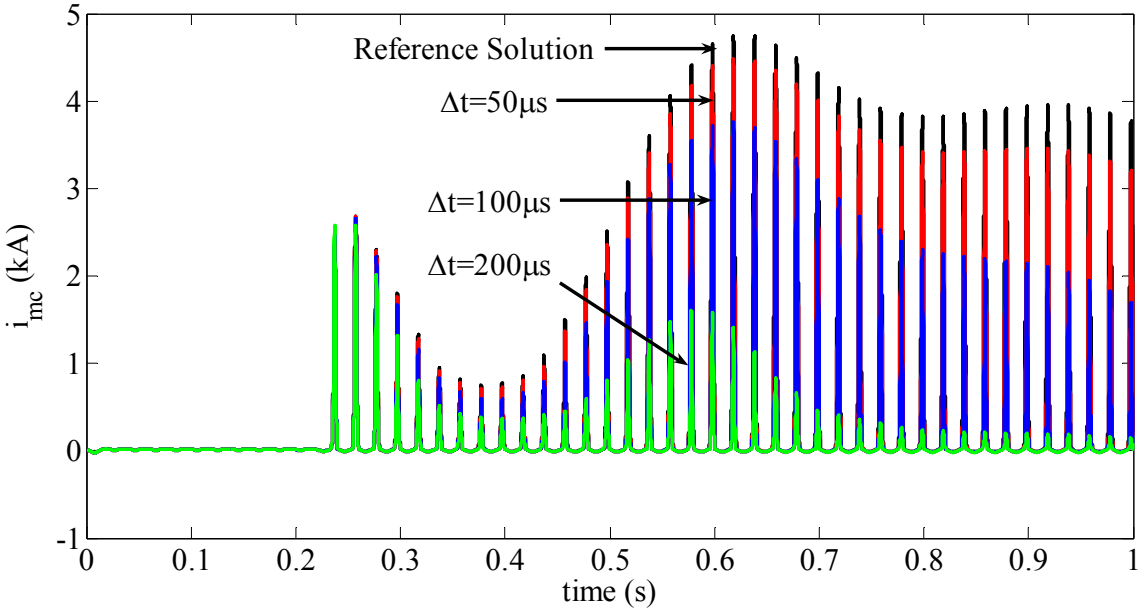

Figure 4.17 Numerical solutions with PD-dq0 model and the reference waveform for phase-c current on transformer magnetizing branch, Test Case C6,

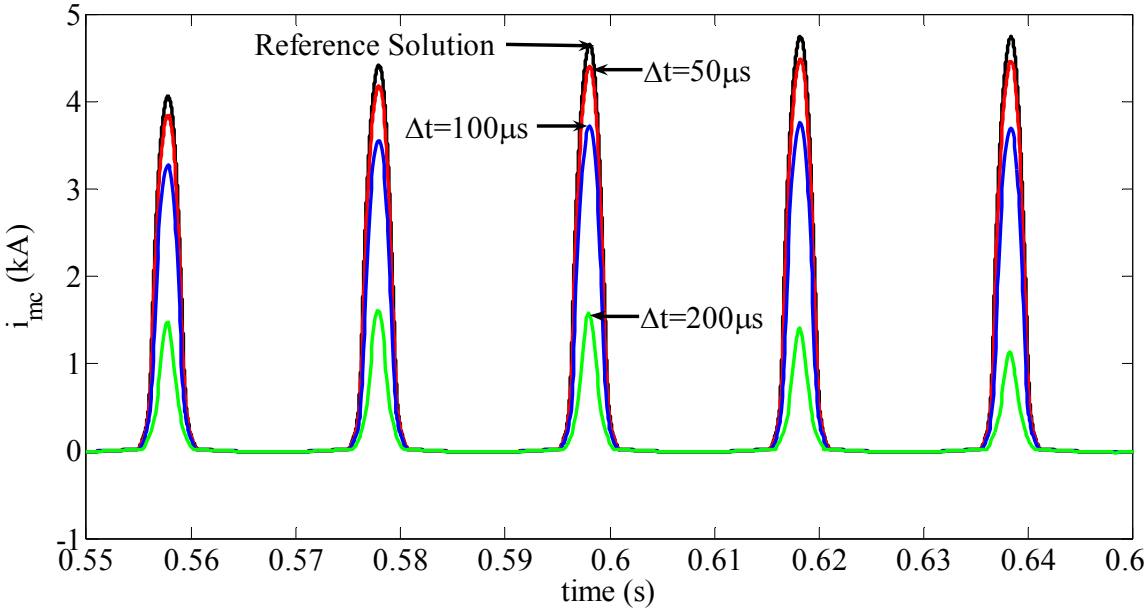

Figure 4.18 Zoomed version of Figure 4.17

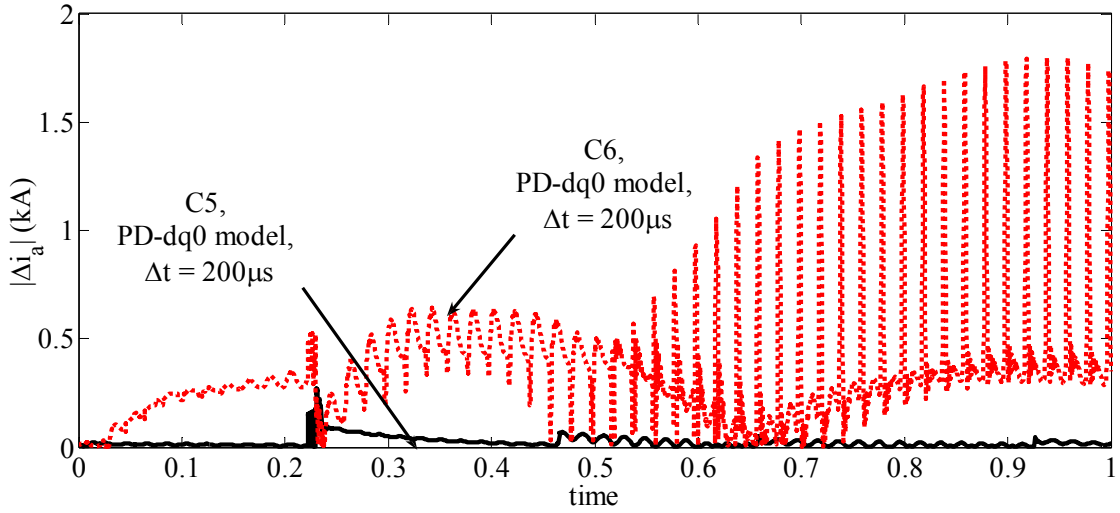

Figure 4.19 Differences between phase-a currents and the reference waveform for Test Cases C5 and C6, PD-dq0 model, $\Delta t = 200\mu s$

Table 4.14 Error e%, Armature Currents, Test Case C6

Δt	dq0	dq0-IITS ($\Delta t_i = \Delta t/8$)	PD	PD-dq0	dq+PD	VBR	dq+VBR
50μs	0.3444	0.3429	0.321	0.321	0.32	0.32	0.32
100μs	1.2539	1.2511	1.2485	1.2485	1.2451	1.2308	1.2325
200μs	3.0655	2.8716	2.9516	2.9519	2.9322	2.8822	2.8944

Table 4.15 Error e%, Electrical Torque, Test Case C6

Δt	dq0	dq0-IITS ($\Delta t_i = \Delta t/8$)	PD	PD-dq0	dq+PD	VBR	dq+VBR
50μs	0.1990	0.2010	0.1910	0.1910	0.1909	0.1852	0.1852
100μs	0.7417	0.7385	0.7422	0.7422	0.7372	0.7211	0.7229
200μs	2.0791	1.9210	1.9714	1.9711	1.9663	1.8529	1.8422

4.2. Transient Stability Case

4.2.1. System Description

The single line diagram of the simulated system (a small area located in northeastern part of Turkish Power System) [21], [44] is shown in Figure 4.20; and the power injections, total load and network losses based on the EMTP-RV load flow

simulation result are illustrated in Table 4.16. The system contains 6 synchronous machines, but 5 of them are in service in the simulated cases.

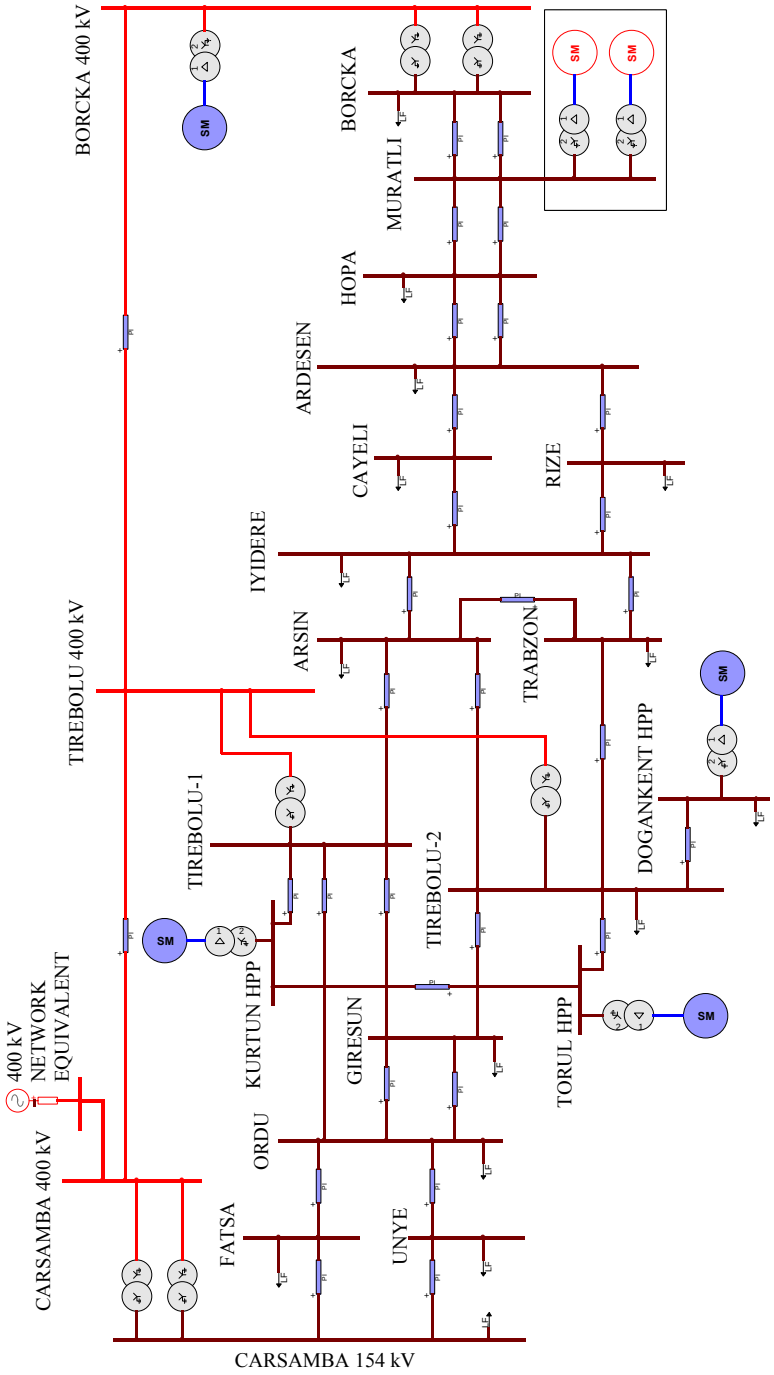

Figure 4.20 Single line EMTP-RV diagram of the transient stability case

Table 4.16 Power Injections, Total Load and Network Losses

	P (MW)	Q (MVAR)	Installed Capacity (MW)
System	82.8	12.5	-
Borcka HPP	140	2.6	157.5
Muratli HPP	50	9.7	2 x 58.5
Dogankent HPP	35	4.7	40.5
Kurtun HPP	30	3.5	40.5
Torul HPP	20	1.9	25
Total Generation	**357.8**	**34.9**	**-**
Total Load	**354.5**	**85.5**	**-**
Network Losses	**3.3**	**-50.6**	**-**

In these simulations transmission lines are represented by multiphase pi equivalent circuits and loads are presented by equivalent R-L branches connected from bus to ground at each phase. Transformers are modeled by considering their connection group. The Turkish Power System, except the modeled portion is represented with Thevenin equivalent. Synchronous machines are modeled with turbine governor and exciter controls. It should be noted that, the simulated system does not involve nonlinear models, such as machine saturation. The circuit breaker opening times are determined based on Table 4.17 provided by the Planning Department of Turkish Transmission Company (APK-TEIAS).

Table 4.17 Circuit Breaker Fault Clearing Times

	Local Breaker	Local Back-up Breakers	Remote Breaker	Remote Back-up Breakers
Primary Relay Time	< 25 ms	< 25 ms	< 25 ms	< 25 ms
Auxiliary Relay(s) Time	< 10 ms	< 10 ms	< 10 ms	< 10 ms
Communication Chanel Time	-	-	< 20 ms	< 20 ms
Breaker-tripping Module	< 5 ms	< 5 ms	< 5 ms	< 5 ms
Breaker Time (2 cycle)	< 40 ms	< 40 ms	< 40 ms	< 40 ms
Breaker Failure Timer Setting	-	< 110 ms	-	< 110 ms
TOTAL TIME	**< 80 ms**	**< 190 ms**	**< 100 ms**	**< 210 ms**

4.2.2. Simulated Cases

Cases TS-C1: A three-phase-to-ground fault is applied on the BORCKA end of the 400 kV BORCKA-TIREBOLU line at 0.02 s. The line circuit breaker at the BORCKA substation is assumed to be stuck and the fault is cleared by the local backup circuit breakers at BORCKA side illustrated in Figure 4.21, with open position following the operation of the busbar protection. The system is simulated for 3 s.

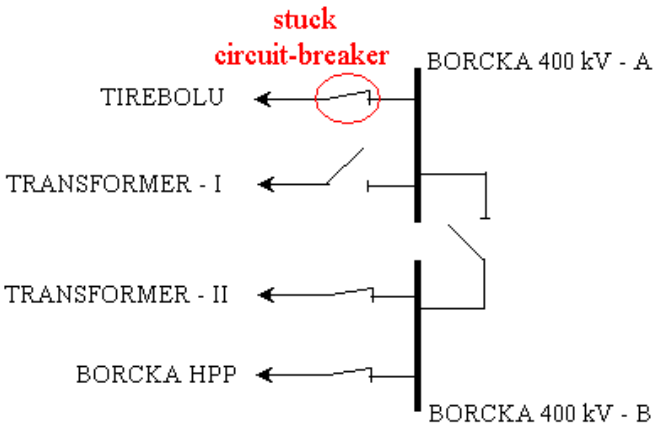

Figure 4.21 Simplified single line diagram of the BORCKA Substation

Cases TS-C2: The case TS-C1 is repeated now with a single-phase-to-ground fault by considering single phase reclosure facility. At the TIREBOLU substation the faulted phase is opened following the fault and the remaining two phases are opened after the operation of busbar protection at the BORCKA substation.

4.2.3. Simulation Results

In both cases, the network returns to stability. The worst errors in electrical torques are observed at the BORCKA HPP and presented in Table 4.18 and Table 4.19. As in the simple single machine - infinite bus test cases in Section 4.1, all models provide better accuracy when compared to the classical dq0 model. The precisions of the proposed new models dq0-IITS, PD-dq0, dq+PD and dq+VBR are comparable to PD and VBR models.

Table 4.18 Error e%, Electrical Torque, TS-C1

Δt	dq0	dq0-IITS ($\Delta t_i = \Delta t/8$)	PD	PD-dq0	dq+PD	VBR	dq+VBR
50μs	0.0171	0.0131	0.0119	0.0119	0.0119	0.0113	0.0113
100μs	0.0668	0.0356	0.0323	0.0323	0.0328	0.0329	0.0331
200μs	0.2548	0.1289	0.1039	0.1044	0.1091	0.0991	0.1051
500μs	1.738	0.9001	0.7409	0.7462	0.7621	0.7219	0.7521
1000μs	6.188	2.4533	2.319	2.366	2.4103	2.1216	2.3575

Table 4.19 Error e%, Electrical Torque, TS-C2

Δt	dq0	dq0-IITS ($\Delta t_i = \Delta t/8$)	PD	PD-dq0	dq+PD	VBR	dq+VBR
50μs	0.0133	0.0118	0.0091	0.0091	0.0096	0.0089	0.0093
100μs	0.0472	0.0411	0.0319	0.0319	0.0327	0.0321	0.0329
200μs	0.1793	0.1325	0.1106	0.1111	0.1144	0.1076	0.1139
500μs	1.1396	0.6375	0.5576	0.5605	0.5939	0.5416	0.5942
1000μs	3.3386	2.2572	1.9882	2.0499	2.168	1.8079	1.8815

It should be noted that, this network portion is closely coupled and all machines are affected from fault. Therefore, intermediate time step usage in dq0-IITS model starts for all machine models following fault within a few time steps. For illustration purposes the field currents of all active machines in Figure 4.20 are presented in Figure 4.22 for TS-C1. These currents are monitored for switching back to normal time step in dq0-IITS, and switching back to dq0 model in dq+PD or dq+VBR models. In the dq0-IITS model case, the intermediate time step usage starts at the fault instant (0.02 s) for all machines and ends at 0.258 s, 0.254 s, 0.241 s, 0.241 s and 0.240 s for the BORCKA, MURATLI, KURTUN, TORUL, and DOGANKENT machines, respectively. As both dq+PD or dq+VBR models have the same tolerance values with the dq0-IITS model, PD or VBR model usage starts at 0.02 s and ends at 0.258 s.

The usage of damping resistances (see (3.10)) for correcting numerical stability problems reduces accuracy (see Table 4.20). The error due to damping resistances is less noticeable at higher Δt due to reduced overall accuracy. It should be noted that in both dq+PD and dq+VBR models, damping resistances are present only when the machines are using the dq0 model.

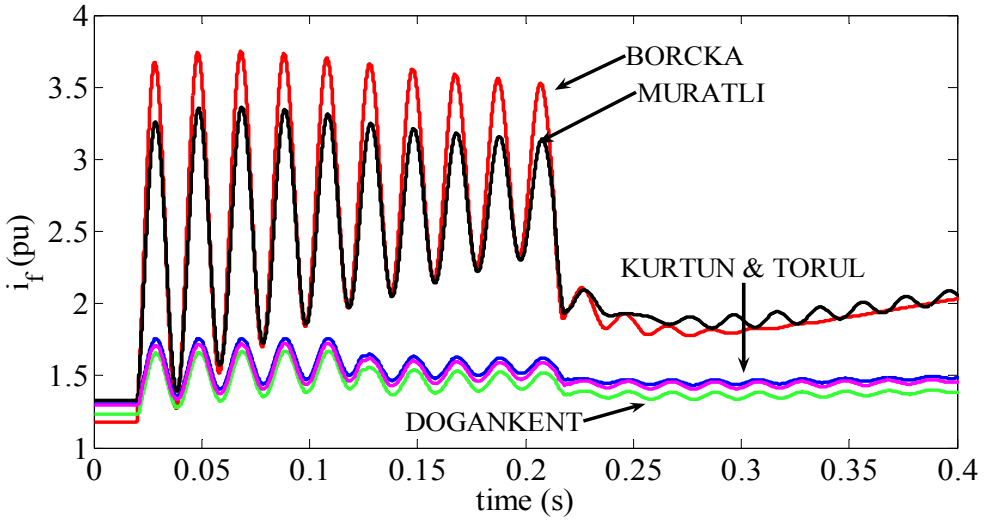

Figure 4.22 Field currents (pu) for the synchronous machines of Figure 4.20, TS-C1

Table 4.20 Error e%, Electrical Torque, TS-C1 (with Damping Resistor Usage)

Δt	dq0	dq0-IITS ($\Delta t_i = \Delta t/8$)	PD-dq0	dq+PD	dq+VBR
50µs	0.0418	0.0251	0.0222	0.0153	0.0152
100µs	0.0989	0.0481	0.0434	0.0371	0.0377
200µs	0.3136	0.1431	0.1163	0.1147	0.1106
500µs	1.935	0.9671	0.7905	0.7799	0.7679
1000µs	6.5117	2.5533	2.4597	2.4411	2.3881

It is apparent from Table 4.18 and Table 4.20 that instead of using the dq0 model with $\Delta t = 100\mu s$ and damping resistances, it is possible to achieve similar accuracy with $\Delta t = 200\mu s$ when using PD-dq0 PD, dq+PD, VBR or dq+VBR models without damping resistances. When smaller (typically equal or less than $\Delta t = 50\mu s$) time steps are used for the dq0 model, the damping resistances are not required and such comparisons become invalid. Although damping resistance usage reduces precision of PD-dq0, dq+PD and dq+VBR models, they are still comparable to PD and VBR models.

It should be noted that, damping resistances produce high errors during fault conditions due to high armature currents. The effect of damping resistances on the accuracy of the dq+PD and dq+VBR models is not significant because these models move into the PD and VBR models respectively only during the fault duration.

It is emphasized again that the presented study is not valid for all types of transients. The simulated network is linear and the pi-section representation is used for transmission lines. The representation of saturation is neglected in transformer and machine models. In a more generic case, the usage of large time steps may cause convergence problems in the iterative process with nonlinear devices or other drifts in precision. Large steps are acceptable and needed for computational performance issues when studying electromechanical transients using EMT-type methods.

The CPU timings for TS-C1 with $\Delta t = 100\mu s$ and $\Delta t = 200\mu s$ time step usage are presented in Table 4.21.

Table 4.21 CPU Timings in pu based on dq0 model, TS-C1

Δt	PD- dq0	dq+VBR	dq+PD	dq0-IITS ($\Delta t_i = \Delta t/8$)	VBR	PD
100μs	1.02	1.10	1.12	1.15	1.97	2.14
200μs	1.02	1.11	1.13	1.16	2.11	2.29

Contrary to indications in [26] and [27], the PD model implementation presented in this thesis has been found to provide precision comparable to VBR. Table 4.21 shows that, their computational speeds are also comparable. These models need to refactor the MNE at each solution time point; thus creating significant computational speed drops.

In the dq+PD and dq+VBR models, PD and VBR model usage is restricted to the transient intervals where the precision of dq0 formulation decreases. As these models are utilized for the time period less than 10% of total simulation time (see Figure 4.22), the increase in simulation time is not significant in this case. On the other hand both models provide similar to PD and VBR models (see Table 4.18 and Table 4.19).

As in the case of dq+PD and dq+VBR models, the dq0-IITS model improves simulation accuracy with intermediate time step usage where the precision of dq0 formulation decreases. As seen from Table 4.18 and Table 4.19, dq0-IITS achieves a precision comparable to PD and VBR models. However, damping resistance usage with this model reduces precision when compared to dq+PD and dq+VBR models. On the

other hand, damping resistances may be required in some cases with large time step usage and the error due to damping resistances is less noticeable at large time steps (see Table 4.20). As the simulated network is closely coupled, all the machines are affected from the fault. Hence, dq0-IITS performance is behind dq+PD and dq+VBR models. On the other hand, electromagnetic transients are local in nature and most of the machines are not expected to be affected while simulating a large scale system. In that case the performance of dq0-IITS is expected to be better when compared to dq+PD and dq+VBR models.

The PD-dq0 model was obtained by applying Park's transformation to the discretized equations of the PD model; hence it maintains the precision of the PD model (see Table 4.18 and Table 4.19). On the other hand, the computational inefficiency of the original PD model is eliminated through a constant admittance matrix. As seen from Table 4.21, constant admittance matrix usage provides similar computational speed with the classical dq0 model. The only disadvantage is the fact that the Norton currents of PD-dq0 model contain predicted stator currents. This is alike the dq0 model and may require damping resistances for correcting numerical stability in some cases with large time step usage. However, the error due to damping resistances is less noticeable at large time steps due to reduced overall accuracy as illustrated in Table 4.20.

It should be noted that, the iterative calculation for the rotor electrical speed in dq0 and PD-dq0 models has negligible influence on simulation accuracy in all simulated cases. In addition, its effect on simulation speed is also not noticeable especially for $\Delta t = 200\mu s$ and smaller simulation time steps with the default relative tolerance value (10^{-6}). As the simulation time step is increased further, this iterative calculation becomes active for longer periods for all machines and its effect on simulation speed becomes more noticeable. Disabling this iterative calculation reduces CPU timings about 1% for both cases for 1 ms simulation time step usage. On the other hand, its effect on simulation speed is expected to be more noticeable for a smaller size system.

4.3. Subsynchronous Resonance (SSR) Case

4.3.1. System Description and Simulated Cases

This case is based on a 380 kV system illustrated in Figure 4.23. Each synchronous machine subnetwork (SM) contains the machine models with controls and step-up transformers. The simulated system components are summarized in Table 4.22. Further details regarding the simulated system can be found in [45]. The test cases are given in Table 4.23. All loads are assumed to be passive at all frequencies and are represented by equivalent impedances connected from bus to ground on each phase. The series capacitors and shunt reactors are simulated by lumped circuit models. The transmission lines are represented by either distributed parameter line models or coupled pi-sections (see Table 4.23). This system contains 30 synchronous machines with governor and exciter control models.

Table 4.22 SSR System Model Summary

# of nodes	420
# of synchronous machines	30
# of single phase transformers	90
# of distributed parameter lines	102
# of multi-phase PI sections	78
# of RLC branches	342

Table 4.23 SSR Cases

Test Case	Machine Saturation	Transmission Line Model (for length > 100 km)
SSR-C1	Not modeled	Distributed Parameter
SSR-C2	Modeled	Distributed Parameter
SSR-C3	Not modeled	Multi-phase PI Section
SSR-C4	Modeled	Multi-phase PI Section

In this case, the potential for SSR transient torque amplification is investigated for the thermal unit located at KANGA Thermal Power Plant (TPP) illustrated in Figure 4.23. A three-phase-to-ground fault is applied at 0.02 s on the 380 kV KANGA bus and cleared with 140 ms delay. The system is simulated for 400 ms.

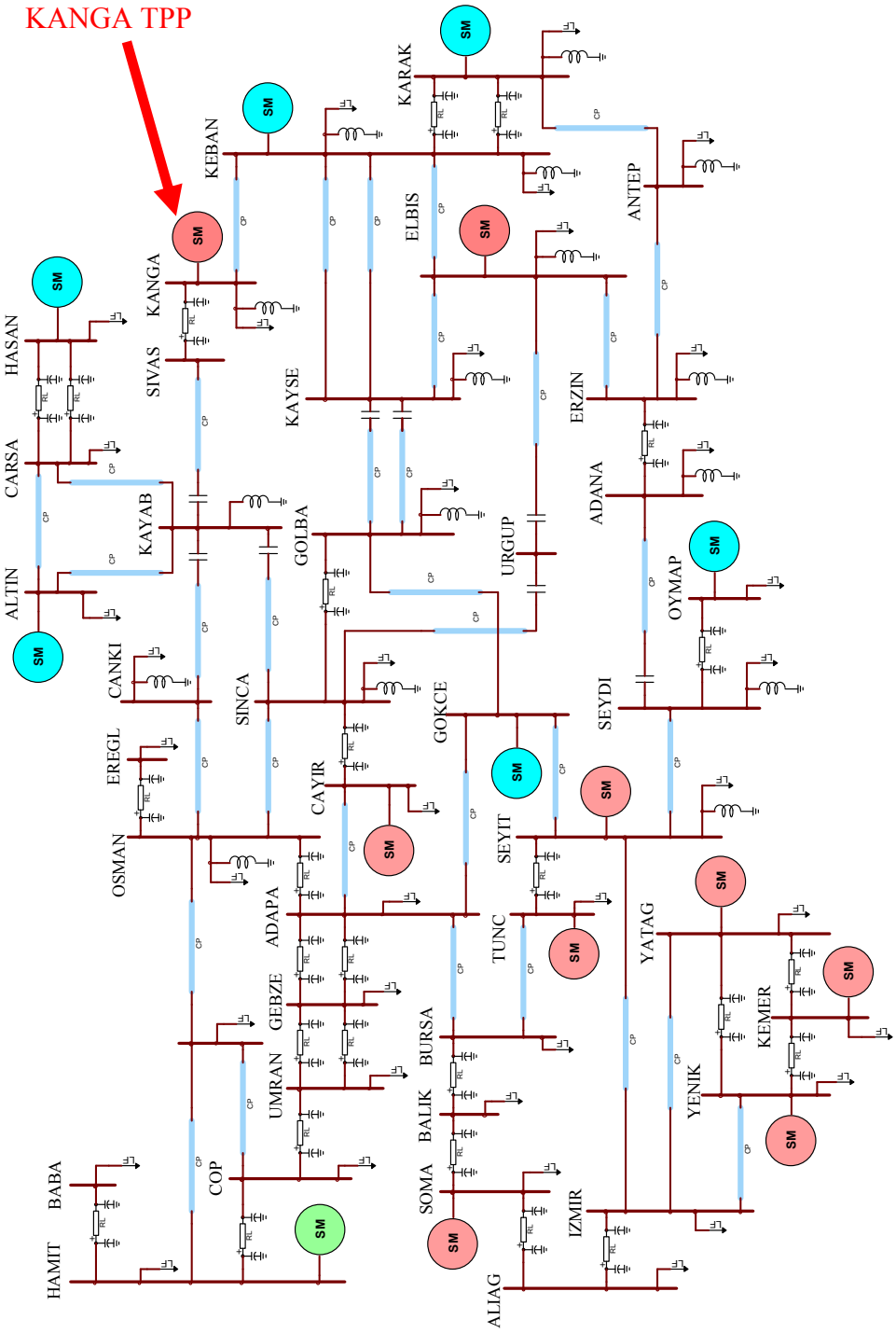

Figure 4.23 Single line EMTP-RV diagram of the SSR case

4.3.2. Simulation Results

The errors in electrical torque observed at KANGA TPP for SSR-C1 – SSR-C4 are presented in Table 4.24 - Table 4.27, respectively. It should be also noted that the worst errors in electrical torques are observed at KANGA TPP.

Table 4.24 Error e%, Electrical Torque, SSR-C1

Δt	dq0	dq0-IITS ($\Delta t_i = \Delta t/8$)	PD	PD-dq0	dq+PD	VBR	dq+VBR
50μs	0.0669	0.0652	0.0644	0.0644	0.0645	0.0632	0.0632
100μs	0.1561	0.1524	0.1469	0.1469	0.1498	0.1419	0.1441
200μs	0.6310	0.5421	0.5003	0.5003	0.5114	0.4871	0.4978

Table 4.25 Error e%, Electrical Torque, SSR-C2

Δt	dq0	dq0-IITS ($\Delta t_i = \Delta t/8$)	PD	PD-dq0	dq+PD	VBR	dq+VBR
50μs	0.0729	0.0681	0.0657	0.0661	0.0659	0.0659	0.0664
100μs	0.2144	0.1735	0.1644	0.1682	0.1702	0.1667	0.1723
200μs	0.8347	0.6175	0.5639	0.5714	0.5807	0.5791	0.5881

Table 4.26 Error e%, Electrical Torque, SSR-C3

Δt	dq0	dq0-IITS ($\Delta t_i = \Delta t/8$)	PD	PD-dq0	dq+PD	VBR	dq+VBR
50μs	0.1581	0.1580	0.1565	0.1565	0.1566	0.1564	0.1564
100μs	0.3022	0.2971	0.2881	0.2881	0.2893	0.2880	0.2887
200μs	0.7415	0.6732	0.6416	0.6417	0.6499	0.6435	0.6487
500μs	2.4497	1.059	0.8776	0.8777	0.8857	0.9519	0.9576
1000μs	8.9631	2.2145	1.6646	1.6649	1.6865	1.8306	1.8471

Table 4.27 Error e%, Electrical Torque, SSR-C4

Δt	dq0	dq0-IITS ($\Delta t_i = \Delta t/8$)	PD	PD-dq0	dq+PD	VBR	dq+VBR
50μs	0.1709	0.1694	0.1659	0.1663	0.1665	0.1682	0.1683
100μs	0.3460	0.3349	0.2971	0.2972	0.3011	0.3041	0.3058
200μs	0.8756	0.7212	0.6662	0.6671	0.6785	0.6898	0.6971
500μs	3.7077	1.3184	0.9902	0.9912	1.1093	1.1906	1.2896
1000μs	11.240	3.1844	2.9377	2.9437	3.1833	3.1241	3.2773

In the test cases SSR-C1 and SSR-C2 propagation delay based model usage for transmission lines longer than 100 km imposes a hard upper limit on Δt, therefore the

simulations with $\Delta t = 500\mu s$ and $\Delta t = 1ms$ cannot be performed. Using distributed constant parameter transmission line models instead of pi-sections improves the accuracy in the computation of high frequency transients resulting from fault removal. Hence, the errors in electrical torque values are smaller for SSR-C1 and SSR-C2 compared to SSR-C3 and SSR-C4, respectively. As SSR-C2 and SSR-C4 include machine saturation model, the simulation precision for those cases are worse compared to SSR-C1 and SSR-C3, due to segment jump effect in machine operating point on saturation curve.

Unlike the transient stability case in Section 4.2, this network is not closely coupled; hence intermediate time step usage in dq0-IITS does not become active for all machines. As illustrated in Figure 4.24, the intermediate time step usage option is triggered for the units in KEBAN, but not in HAMIT after fault. In addition it is not triggered for the units in HAMIT after switching for fault removal. In the simulated cases, the intermediate time step usage option is not triggered for 17 of 30 synchronous machines during simulation. It should be noted that, by setting t_{V-mon} to a smaller value, it is possible to reduce the number of machines triggered to intermediate time step usage. However, t_{V-mon} should be selected sufficiently long to trigger intermediate time step usage for the machines electrically close to the fault location. Unlike the dq0-IITS model in the cases of dq+PD and dq+VBR models, all machine models switch to the accurate version when any machine is subjected to a voltage excursion above the predefined tolerance after the detection of a network switching event.

For illustration purposes, the field currents of the machines at KEBAN, HAMIT and KANGA are presented in Figure 4.25. Field currents of the machines at KEBAN and KANGA are monitored for switching back to normal time step in dq0-IITS, and switching back to the dq0 model in dq+PD and dq+VBR models. In the dq0-IITS case, intermediate time step usage starts at 0.0205 s and 0.02s, and ends at 0.187 s and 0.298 s for the machines at KEBAN and KANGA, respectively. On the other hand, PD and VBR model usage starts at 0.02 s and ends at 0.298 s. As seen from Figure 4.25 the field

currents of the machines at HAMIT do not contain significant fundamental ac component. This implies that the armature currents of these machines do not contain significant dc components; hence the precision of the dq0 model is not expected to deteriorate.

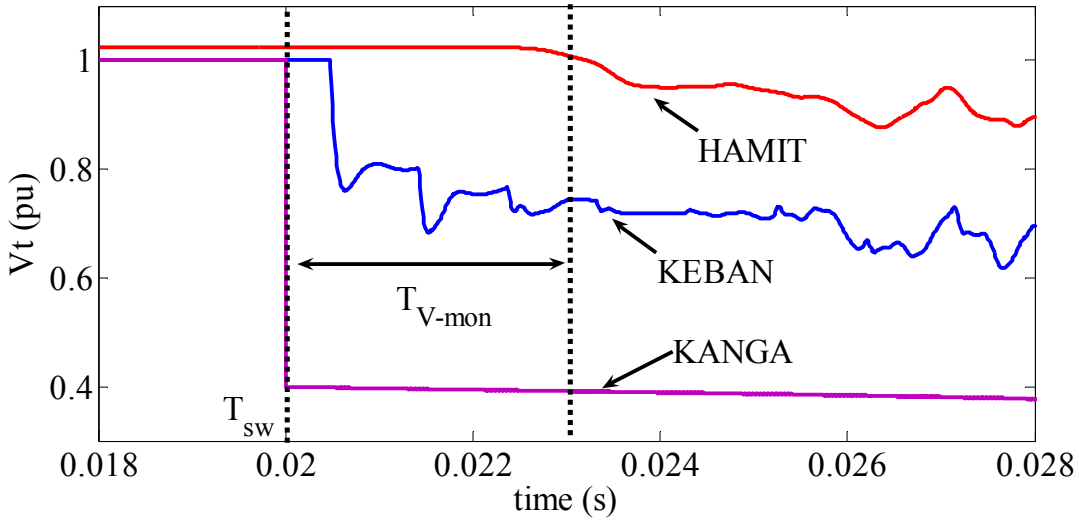

Figure 4.24 Machine terminal voltages (pu) for the synchronous machines in HAMIT, KEBAN and KANGA; SSR-C2

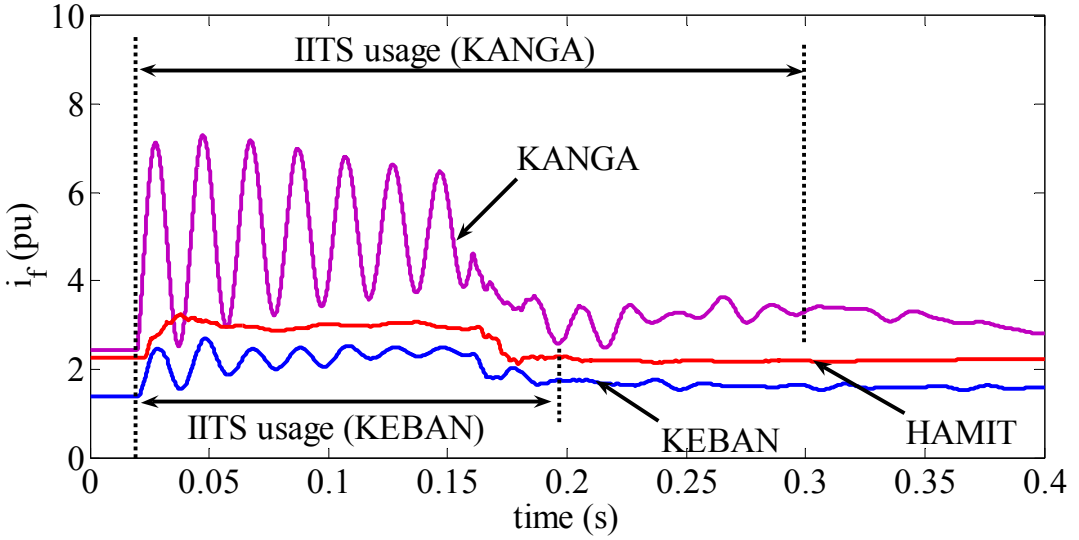

Figure 4.25 Machine field currents (pu) for the synchronous machines in HAMIT, KEBAN and KANGA; SSR-C2

CPU timings for the SSR-C2 test case with $\Delta t = 100\mu s$ and $\Delta t = 200\mu s$ time step usage are presented in Table 4.28.

Table 4.28 CPU Timings in pu based on dq0 model, SSR-C2

Δt	PD- dq0	dq0-IITS ($\Delta t_i = \Delta t/8$)	dq+VBR	dq+PD	VBR	PD
100μs	1.02	1.32	1.66	1.71	1.92	1.98
200μs	1.03	1.43	1.76	1.83	2.05	2.15

According to the error values summarized in the tables (Table 4.24 to Table 4.27), PD-dq0, dq+PD and dq+VBR models offer the same accuracy as the competing PD and VBR models. Unlike the case in Section 4.2, the precision of dq0-IITS is slightly below PD-dq0, dq+PD and dq+VBR models. The precision of the dq0 model is better in this case compared to the case in Section 4.2 due to a shorter fault period.

As seen from Table 4.21 and Table 4.28, dq+PD and dq+VBR do not provide similar improvement in computational speed as in the case of Section 4.2. Although PD and VBR usage is restricted to the transient intervals where the precision of dq0 decreases, these models are utilized for the time period of more than 70% of total simulation time (see Figure 4.25) in this case. On the other hand dq0-IITS provides better computational speed when compared to dq+PD and dq+VBR models due to the size of the simulated system. As illustrated in Figure 4.25, the intermediate time step is applied only for the machines affected from the fault or discontinuity condition. Its computational speed is expected to be better for a larger scale system.

The new PD-dq0 model offers PD model like accuracy while maintaining dq0 model like speed. Hence it is superior over the proposed dq0-IITS, dq+PD and dq+VBR models in addition to the existing machine models in the literature.

CHAPTER 5.

COMPLEMENTARY STUDIES FOR NUMERICAL EFFICIENCY ASSESSMENT

In CHAPTER 4, it was demonstrated that the new PD-dq0 offers the same accuracy as the competing PD and VBR models. In addition to accuracy this new model remains very efficient when compared to the PD and VBR models. In EMTP-RV simulations, PD-dq0 usage instead of PD or VBR models, increases the simulation speed more than twice due to the constant MNE coefficient matrix usage. On the other hand EMTP-RV uses a complete refactorization scheme and the simulation speed is expected to increase if a partial refactorization scheme is programmed for PD and VBR models. Moreover, the selected sparse matrix solver and machine representation in MANA formulation is expected to have different influence on simulation speed for PD and VBR models when compared to PD-dq0 due to their refactorization requirement. Due the fact that during the realization of this project it was not possible to access and modify the sparse matrix solver of EMTP-RV, it was decided to experiment with an available Matlab based code named MatEMTP [9]. This code is also based on MANA formulation as in EMTP-RV and it replicates many of the solution methods found in EMTP-RV.

This chapter starts by presenting two new MANA formulations for PD and VBR models. Then the KLU [35] sparse matrix approach is briefly introduced and partial refactorization implementation is demonstrated. Simulation results are presented in the last part.

5.1. Background on Modified Augmented Nodal Analysis (MANA) Formulation

The limitations in NA formulation resulting from the existence of admittance model assumption are eliminated in the MANA formulation by augmenting (1.1) to form the system equation given in (1.3) as illustrated below [9]-[11]:

$$\begin{bmatrix} \mathbf{Y_n} & \mathbf{V}_{\mathbf{adj}}^{T} & \mathbf{D_{bdepc}} & \mathbf{S}_{\mathbf{adj}}^{T} \\ \mathbf{V_{adj}} & \mathbf{0} & \mathbf{0} & \mathbf{0} \\ \mathbf{D_{bdepr}} & \mathbf{0} & \mathbf{0} & \mathbf{0} \\ \mathbf{S_{adj}} & \mathbf{0} & \mathbf{0} & \mathbf{S_0} \end{bmatrix} \begin{bmatrix} \mathbf{v_n} \\ \mathbf{i_{Vs}} \\ \mathbf{i_{Vd}} \\ \mathbf{i_S} \end{bmatrix} = \begin{bmatrix} \mathbf{i_n} \\ \mathbf{v_S} \\ \mathbf{0} \\ \mathbf{0} \end{bmatrix} \tag{5.1}$$

In (5.1) $\mathbf{V_{adj}}$ is the voltage source adjacency matrix; row and column contribution matrices $\mathbf{D_{bdepr}}$ and $\mathbf{D_{bdepc}}$ are used for holding the branch dependent relations; $\mathbf{S_{adj}}$ is the adjacency matrix of closed switch type devices; $\mathbf{S_0}$ is a diagonal and unitary matrix for open switch type devices; $\mathbf{i_{Vs}}$ is the vector of unknown voltage source currents; $\mathbf{i_{Vd}}$ is the vector of unknown currents in dependent voltage source branches; $\mathbf{i_S}$ is the vector of unknown switch currents. The above presentation is only for analysis purposes since in reality the equations can be entered in any order. It is also noticed that the matrix $\mathbf{S_0}$ is not necessarily unitary if switch resistances are used. Extra elements can be added in the switch rows for modeling various devices, such as diodes.

In the standard approach presented in the previous chapters and in EMTP-RV, the synchronous machines are incorporated by modifying the admittance matrix $\mathbf{Y_n}$ and the Norton current sources contribute to the vector $\mathbf{i_n}$.

5.1.1. MANA Formulation with Machine Thevenin Equivalents (MANA-Thevenin)

In the following formulation equation (5.1) is augmented to include extra generic equations based on the generalized nodal relations and the machine TE circuits:

$$\begin{bmatrix} \mathbf{Y_n} & \mathbf{V}_{\mathbf{adj}}^T & \mathbf{D_{bdepc}} & \mathbf{S}_{\mathbf{adj}}^T & \mathbf{SM}_{\mathbf{adj}}^T \\ \mathbf{V_{adj}} & \mathbf{0} & \mathbf{0} & \mathbf{0} & \mathbf{0} \\ \mathbf{D_{bdepr}} & \mathbf{0} & \mathbf{0} & \mathbf{0} & \mathbf{0} \\ \mathbf{S_{adj}} & \mathbf{0} & \mathbf{0} & \mathbf{S_0} & \mathbf{0} \\ \mathbf{SM_{adj}} & \mathbf{0} & \mathbf{0} & \mathbf{0} & \mathbf{A_{SM}} \end{bmatrix} \begin{bmatrix} \mathbf{v_n} \\ \mathbf{i_{Vs}} \\ \mathbf{i_{Vd}} \\ \mathbf{i_S} \\ \mathbf{x_{SM}} \end{bmatrix} = \begin{bmatrix} \mathbf{i_n} \\ \mathbf{v_S} \\ \mathbf{0} \\ \mathbf{0} \\ \mathbf{b_{SM}} \end{bmatrix} \tag{5.2}$$

where $\mathbf{SM_{adj}}$ is the machine adjacency matrix, $\mathbf{A_{SM}}$ holds the machine equivalent Thevenin resistance matrices ((3.34) and (3.50) for PD and VBR models, respectively), $\mathbf{x_{SM}}$ is the vector of machine stator currents, and $\mathbf{b_{SM}}$ is the vector of machine Thevenin voltages ((3.35) and (3.51) for PD and VBR models, respectively).

This formulation eliminates the computation of Norton equivalents for each machine at each solution time point. Moreover, the solution of (5.2) now provides the machine stator currents in addition to machine terminal voltages. Hence the calculation of stator currents following the MNE solution is also eliminated. As the PD-dq0 model uses a constant Norton admittance matrix, its calculation is not required at each solution time point. Therefore, this formulation is expected to provide improvement in simulation speed mainly for PD and VBR models. On the other hand, this formulation increases the size of the MNE coefficient matrix and may impact on the MNE solution time. Generally speaking, when the size of a sparse matrix increases, it is not necessarily true that its computational speed decreases, as this is related to the resulting sparse matrix patterns.

5.1.2. MANA Formulation with Machine Complete Electrical Equations (MANA-Complete)

In this formulation, (5.2) now includes all machine electrical equations in addition to the generalized nodal relations for the machine-network connection points. $\mathbf{x}_{\mathbf{SM}}$ becomes the vector of unknown machine electrical variables and $\mathbf{b}_{\mathbf{SM}}$ becomes the vector of history terms resulting from the trapezoidal integration method. The matrix $\mathbf{A}_{\mathbf{SM}}$ now holds the contribution of each machine electrical variable to the machine voltage equations. This formulation completely eliminates the computation of machine interfacing circuitry. Moreover, the solution of (5.2) now provides all machine electrical variables in addition to machine terminal voltages. It should be noted that, this machine representation introduces time dependent terms in (5.2) when the PD-dq0 model is utilized. As the advantage of the constant MNE coefficient matrix usage disappears, this formulation is not suitable for the PD-dq0 model.

This formulation increases both the size and the number of time varying terms in the MNE coefficient matrix. Hence, a significant increase is expected in the required time for updating and refactoring the MNE coefficient matrix. On the other hand, this increase in MNE solution time might be less when compared to the time gained from the computations regarding machine equations especially with efficient sparse matrix solvers.

5.1.2.1. Formulation for the PD Model

The MNE (5.2) is formed by inserting discretized voltage equations for the PD model given in (3.27). Hence, $\mathbf{x}_{\mathbf{SM}}$ now holds the machine stator and rotor currents. For the j^{th} machine, the related sub-matrix of $\mathbf{A}_{\mathbf{SM}}$, the related sub-vectors of $\mathbf{x}_{\mathbf{SM}}$ and $\mathbf{b}_{\mathbf{SM}}$ are given by

$$\mathbf{A}_{\mathbf{SM}}^{\mathbf{j}} = \begin{bmatrix} \mathbf{R}_{\mathbf{ss}}^{\mathbf{j}}(\theta) & \mathbf{R}_{\mathbf{sr}}^{\mathbf{j}}(\theta) \\ \mathbf{R}_{\mathbf{rs}}^{\mathbf{j}}(\theta) & \mathbf{R}_{\mathbf{rr}}^{\mathbf{j}} \end{bmatrix} \tag{5.3}$$

$$\mathbf{x}_{\mathbf{SM}}^{\mathbf{j}} = \begin{bmatrix} \mathbf{i}_{\mathbf{s}}^{\mathbf{j}} \\ \mathbf{i}_{\mathbf{r}}^{\mathbf{j}} \end{bmatrix} \tag{5.4}$$

$$\mathbf{b}_{\mathbf{SM}}^{\mathbf{j}} = \begin{bmatrix} \mathbf{h}_{\mathbf{s}}^{\mathbf{j}} - k\,\boldsymbol{\lambda}_{\mathbf{sk}} \\ \mathbf{h}_{\mathbf{r}}^{\mathbf{j}} - k\,\boldsymbol{\lambda}_{\mathbf{rk}} - \mathbf{v}_{\mathbf{r}}^{\mathbf{j}} \end{bmatrix} \tag{5.5}$$

In the solid-rotor machine case, $\boldsymbol{\lambda}_{\mathbf{sk}}$ and $\boldsymbol{\lambda}_{\mathbf{rk}}$ in (5.5) contain predicted λ_{kdj} and λ_{kqj} values (see see (2.71), (2.72) and (2.77)). Hence the iterative solution for λ_{kdj}, λ_{kqj} and $\mathbf{i}_{\mathbf{r}}$ should be performed using (2.63), (2.64), (3.21) and (3.37) for correction.

The sequence of calculation steps is briefly described below:

1. predict ω and θ (see (3.6) and (3.7)) to calculate $\mathbf{P}(\theta)$ and $\mathbf{L}(\theta)$;
2. predict λ_{kdj} and λ_{kqj} to find $\boldsymbol{\lambda}_{\mathbf{sk}}$ and $\boldsymbol{\lambda}_{\mathbf{rk}}$ (see (2.71), (2.72) and (2.77));
3. refactorize and solve the MNE to find $\mathbf{v}_{\mathbf{s}}$, $\mathbf{i}_{\mathbf{s}}$ and $\mathbf{i}_{\mathbf{r}}$;
4. find $\mathbf{i}_{\mathbf{dq0}}$ using (2.12);
5. find λ_{ad} using (2.63) and λ_{aq} using (2.64) for correcting λ_{kdj} and λ_{kqj}, hence $\boldsymbol{\lambda}_{\mathbf{sk}}$ and $\boldsymbol{\lambda}_{\mathbf{rk}}$;
6. compare predicted and corrected values for λ_{kdj} and λ_{kqj}, if no convergence correct $\mathbf{i}_{\mathbf{r}}$ using (3.37) and go to step 5;

7. check for the machine operating segment on saturation curve, if the operating segment needs to change
   - update L_{ad}, L_{aq} and all related terms in $\mathbf{L}(\theta)$ (L_{aa0}, L_{ab0} and L_{aa2} terms in $\mathbf{L_{ss}}(\theta)$; L_{aF}, L_{aD}, L_{aQ1} and L_{aQ2} terms in $\mathbf{L_{sr}}(\theta)$ and $\mathbf{L_{rs}}(\theta)$, L_{FF}, L_{FD}, L_{DD}, L_{Q1Q1}, L_{Q1Q2}, L_{Q2Q2} terms in $\mathbf{L_{rr}}$),
   - update λ_{kdj} and λ_{kqj}, hence $\boldsymbol{\lambda}_{\mathbf{sk}}$ and $\boldsymbol{\lambda}_{\mathbf{rk}}$ with updated λ_{kj} value,
   - recalculate magnetizing flux linkages λ_{ad} and λ_{aq} for the new operating segment,
   - switch solution method to Backward Euler for the next time step;
8. find flux linkages using (2.76)
9. find electromagnetic torque using (2.20) and solve the mechanical equations (3.1) and (3.2) to find $\boldsymbol{\theta}_{\mathbf{m}}$ and $\boldsymbol{\omega}_{\mathbf{m}}$;
10. return to step 1 for the next time point solution.

In the salient pole case, the solution procedure does not contain steps 2, 5 and 6.

5.1.2.2. Formulation for the VBR Model

The MNE (5.2) is formed by inserting VBR equations given by (3.38), (3.41) and (3.46). In this formulation, the unknown electrical variable vector $\mathbf{x_{SM}}$ includes the stator currents in dq coordinates ($\mathbf{i_{dq}}$), the subtransient voltages in phase and dq coordinates ($\mathbf{v''_{abc}}$ and $\mathbf{v''_{dq}}$) in addition to rotor flux linkages ($\boldsymbol{\lambda}_{\mathbf{r}}$) and stator currents in phase coordinates ($\mathbf{i_s}$). For the j^{th} machine, the related submatrix of $\mathbf{A_{SM}}$, the related sub-vectors of $\mathbf{x_{SM}}$ and $\mathbf{b_{SM}}$ are given by

$$\mathbf{A}_{\mathbf{SM}}^{\mathbf{j}} = \begin{bmatrix} \left(\mathbf{R}_{\mathbf{s}}^{\mathbf{j}} + k\,\mathbf{L}_{\mathbf{abc}}''^{\mathbf{j}}(\theta)\right) & -\mathbf{I}_{\mathbf{3x3}} & \mathbf{0}_{\mathbf{3x2}} & \mathbf{0}_{\mathbf{3x2}} & \mathbf{0}_{\mathbf{3x4}} \\ \mathbf{0}_{\mathbf{3x3}} & -\mathbf{I}_{\mathbf{3x3}} & \mathbf{0}_{\mathbf{3x3}} & \tilde{\mathbf{P}}^{\mathbf{j}}(\theta) & \mathbf{0}_{\mathbf{3x4}} \\ \left(\tilde{\mathbf{P}}^{\mathbf{j}}(\theta)\right)^{T} & \mathbf{0}_{\mathbf{2x3}} & -\mathbf{I}_{\mathbf{2x2}} & \mathbf{0}_{\mathbf{2x3}} & \mathbf{0}_{\mathbf{2x4}} \\ \mathbf{0}_{\mathbf{2x3}} & \mathbf{0}_{\mathbf{2x3}} & \mathbf{K}_{\mathbf{I}}^{\mathbf{j}} & \mathbf{I}_{\mathbf{2x2}} & \mathbf{K}_{\boldsymbol{\lambda}}^{\mathbf{j}}(\omega) \\ \mathbf{0}_{\mathbf{4x3}} & \mathbf{0}_{\mathbf{4x3}} & -\mathbf{B}_{\mathbf{I}}^{\mathbf{j}} & \mathbf{0}_{\mathbf{4x2}} & \mathbf{I}_{\mathbf{4x4}} \end{bmatrix} \tag{5.6}$$

$$\mathbf{x}_{\mathbf{SM}}^{\mathbf{j}} = \left[\left(\mathbf{i}_{\mathbf{s}}^{\mathbf{j}}\right)^{T} \quad \left(\mathbf{v}_{\mathbf{abc}}''^{\mathbf{j}}\right)^{T} \quad \left(\mathbf{i}_{\mathbf{dq}}^{\mathbf{j}}\right)^{T} \quad \left(\mathbf{v}_{\mathbf{dq}}''^{\mathbf{j}}\right)^{T} \quad \left(\boldsymbol{\lambda}_{\mathbf{r}}^{\mathbf{j}}\right)^{T} \right]^{T} \tag{5.7}$$

$$\mathbf{b}_{\mathbf{SM}}^{\mathbf{j}} = \begin{bmatrix} \mathbf{h}_{\mathbf{vbrs}}^{\mathbf{j}} \\ \mathbf{0}_{\mathbf{1x3}} \\ \mathbf{0}_{\mathbf{1x2}} \\ -\left(\left[\mathbf{K}_{\boldsymbol{\lambda}\mathbf{k}}^{\mathbf{j}}(\omega) + \mathbf{K}_{\mathbf{p}\boldsymbol{\lambda}\mathbf{k}}^{\mathbf{j}} \right] \boldsymbol{\lambda}_{\mathbf{dqk}}^{\mathbf{j}} - \mathbf{K}_{\mathbf{p}\boldsymbol{\lambda}\mathbf{k}}^{\mathbf{j}} \hat{\boldsymbol{\lambda}}_{\mathbf{dqk}}^{\mathbf{j}} + \mathbf{k}_{\mathbf{VF}}^{\mathbf{j}}\, \hat{v}_F^{j} \right) \\ \left(\mathbf{B}_{\boldsymbol{\lambda}\mathbf{k}}^{\mathbf{j}}\, \boldsymbol{\lambda}_{\mathbf{dqk}}^{\mathbf{j}} + \mathbf{b}_{\mathbf{VF}}^{\mathbf{j}}\, \hat{v}_F^{j} + \mathbf{h}_{\mathbf{vbr}\boldsymbol{\lambda}}^{\mathbf{j}} \right) \end{bmatrix} \tag{5.8}$$

where $\mathbf{I}_{\mathbf{mxm}}$ is mxm size identity matrix, $\mathbf{0}_{\mathbf{kxm}}$ is kxm size zero matrix.

In the solid rotor case, (3.41) is solved using an iterative approach with (2.85), (2.86) and (3.21) after the MNE solution for corrected values for λ_{kdj}, λ_{kqj} and rotor flux linkages $\boldsymbol{\lambda}_{\mathbf{r}}$. The rotor currents can be found by using (2.43) and (2.44). In the salient pole case, (3.41) does not contain predicted values for λ_{kdj} and λ_{kqj}, hence $\boldsymbol{\lambda}_{\mathbf{r}}$ found from the MNE solution does not need correction. The sequence of calculation steps is briefly described below:

1. predict ω and θ to calculate $\tilde{\mathbf{P}}(\theta)$, $\mathbf{L}_{\mathbf{abc}}''(\theta)$, $\mathbf{K}_{\boldsymbol{\lambda}}(\omega)$ and $\mathbf{K}_{\boldsymbol{\lambda}\mathbf{k}}(\omega)$;

2. predict λ_{kdj} and λ_{kqj};

3. refactorize and solve the MNE to find $\mathbf{v}_{\mathbf{s}}$, $\mathbf{i}_{\mathbf{s}}$, $\boldsymbol{\lambda}_{\mathbf{r}}$, $\mathbf{v}_{\mathbf{abc}}''$, $\mathbf{i}_{\mathbf{dq}}$ and $\mathbf{v}_{\mathbf{dq}}''$;

4. find magnetizing flux linkages (λ_{ad} and λ_{aq}) using (2.85) and (2.86), use (3.21) for correcting λ_{kdj} and λ_{kqj} values;

5. compare predicted and corrected λ_{kdj} and λ_{kqj} values, if no convergence find correct $\boldsymbol{\lambda}_{\mathbf{r}}$ using (3.41) and go to step 4;

6. find rotor currents using (2.43) and (2.44),

7. check for the machine operating segment on saturation curve, if the operating segment needs to change
   - update L_{ad}, L_{aq} to recalculate L''_{ad} and L''_{aq} ((2.85) and (2.86)); recalculate L''_{aa0}, L''_{ab0} and L''_{aa2} terms in $\mathbf{L''_{abc}}(\theta)$; the matrices $\mathbf{K}_{\boldsymbol{\lambda}}(\omega)$, $\mathbf{K_I}$, $\mathbf{K_{\lambda k}}(\omega)$, $\mathbf{K_{p\lambda k}}$, $\mathbf{k_{VF}}$, $\mathbf{A}_{\boldsymbol{\lambda}}$, $\mathbf{B_I}$ and $\mathbf{B_{\lambda k}}$ (see Appendix III);
   - update λ_{kdj} and λ_{kqj} with updated λ_{kj} value,
   - recalculate λ_{ad} and λ_{aq} using (2.63) and (2.64) with the calculated rotor currents for the new operating segment,
   - recalculate $\boldsymbol{\lambda}_{\mathbf{r}}$ using (2.29) and (2.30),
   - switch solution method to Backward Euler for the next time step;

8. find electromagnetic torque using (2.20) and solve the mechanical equations (3.1) and (3.2) to find $\boldsymbol{\theta}_{\mathbf{m}}$ and $\boldsymbol{\omega}_{\mathbf{m}}$;

9. return to step 1 for the next time point solution.

In the salient pole case, the solution procedure does not contain steps 2, 4 and 5.

5.2. Solution of Main Network Equations

The solution of the linear equation system in (1.3) can be found by solving two triangular systems derived from LU factorization, i.e.

$$\mathbf{A_n}\ \mathbf{x_n} = \left(\mathbf{L}\ \mathbf{U}\right)\mathbf{x_n} = \mathbf{L}\ (\mathbf{U}\ \mathbf{x_n}) = \mathbf{L}\ \mathbf{y_n} = \mathbf{b_n} \tag{5.9}$$

$$\begin{aligned} \mathbf{L}\ \mathbf{y_n} &= \mathbf{b_n} \\ \mathbf{U}\ \mathbf{x_n} &= \mathbf{y_n} \end{aligned} \tag{5.10}$$

where $\mathbf{U}$ and $\mathbf{L}$ are the upper and lower triangular matrices, respectively.

By utilizing special ordering techniques to generate the row and column permutations, it is possible to reduce the fill-in (new non-zeros in $\mathbf{U}$ and $\mathbf{L}$ that are not present in $\mathbf{A_n}$) during factorization.

$$\mathbf{P_R}\ \mathbf{A_n}\ \mathbf{P_C} = \mathbf{L}\ \mathbf{U} \tag{5.11}$$

Here $\mathbf{P_C}$ is the column and $\mathbf{P_R}$ is the row permutation matrices chosen to reduce fill-in. It should be noted that the permutation $\mathbf{P_R}$ has a dual role of reducing fill-in and maintaining numerical accuracy via partial pivoting and row interchanges. Minimum degree orderings such as AMD [33], [34] or COLAMD [31], [32] orderings can be applied to obtain sparser $\mathbf{U}$ and $\mathbf{L}$ matrices.

The KLU [35] solver uses Block Triangular Factorization (BTF) before ordering for calculating the block triangular form of the matrix $\mathbf{A_n}$ as illustrated in equation (5.12). Ordering and factorization of the block triangular form provides the following advantages:

- The part of the matrix below the block diagonal does not require factorization ;

- The diagonal blocks are independent, hence only these blocks require to be factorized, for instance, the system $\mathbf{A_{33}\ x_3 = b_3 - A_{34}\ x_4}$ is solved for $\mathbf{x_3}$ after solving $\mathbf{A_{44}\ x_4 = b_4}$ for $\mathbf{x_4}$;
- The off-diagonal non-zeros do not contribute to any fill-in.

$$\begin{bmatrix} \mathbf{A_{11}} & \mathbf{A_{12}} & \mathbf{A_{13}} & \mathbf{A_{14}} \\ \mathbf{0} & \mathbf{A_{22}} & \mathbf{A_{23}} & \mathbf{A_{24}} \\ \mathbf{0} & \mathbf{0} & \mathbf{A_{33}} & \mathbf{A_{34}} \\ \mathbf{0} & \mathbf{0} & \mathbf{0} & \mathbf{A_{44}} \end{bmatrix} \begin{bmatrix} \mathbf{x_1} \\ \mathbf{x_2} \\ \mathbf{x_3} \\ \mathbf{x_4} \end{bmatrix} = \begin{bmatrix} \mathbf{b_1} \\ \mathbf{b_2} \\ \mathbf{b_3} \\ \mathbf{b_4} \end{bmatrix} \tag{5.12}$$

KLU employs AMD or COLAMD (user option) for ordering before factorizing of each diagonal block. In [35], AMD is found to provide better results on circuit matrices. KLU performs factorization based on Gilbert-Peierls' left-looking algorithm [46]. Ordering and factoring each block is performed sequentially although parallelism is possible. The reader should refer to [35] for details. The KLU Matrix solver package for MATLAB is available in [47] and factorizes the matrix $\mathbf{A_n}$ as

$$\mathbf{R^{-1}\left(P_R\ A_n\ P_C\right) = L\ U + F} \tag{5.13}$$

where $\mathbf{F}$ contains the entries above the diagonal blocks and $\mathbf{R}$ is the scaling matrix.

5.3. Partial Refactorization

For PD or VBR equations, $\mathbf{A_n}$ in (1.3) becomes time varying due to the time varying self and mutual inductances of these models. Therefore, it is necessary to update and refactor $\mathbf{A_n}$ at each time-step. The simulation speed can be improved with refactoring only the time varying part of $\mathbf{A_n}$. In the proposed formulations only the sub-matrix $\mathbf{A_{SM}}$ contains the time varying terms and it is located at the right bottom corner of $\mathbf{A_n}$ (see (5.2)); hence (1.3) can be written as

$$\begin{bmatrix} \mathbf{A_{n11}} & \mathbf{A_{n12}} \\ \mathbf{A_{n21}} & \mathbf{A_{n22}} \end{bmatrix} \begin{bmatrix} \mathbf{x_{n1}} \\ \mathbf{x_{n2}} \end{bmatrix} = \begin{bmatrix} \mathbf{b_{n1}} \\ \mathbf{b_{n2}} \end{bmatrix} \tag{5.14}$$

where $\mathbf{A_{n22}} = \mathbf{A_{SM}}$, $\mathbf{x_{n2}} = \mathbf{x_{SM}}$ and $\mathbf{b_{n2}} = \mathbf{b_{SM}}$.

In the classical MANA formulation (see (5.1)), the row and columns of the MNE coefficient matrix should be first permuted to relocate the time varying terms at the right bottom corner for partial refactorization. After permutation, i.e. putting (5.1) into the form given in (5.14), the vectors $\mathbf{x_{n2}}$ and $\mathbf{b_{n2}}$ will contain the machine terminal voltages and the known current quantities modified with the machine equivalent Norton currents, respectively. The sub-matrix $\mathbf{A_{n22}}$ will contain the terms modified with the machine equivalent Norton admittances at each solution time point.

In case $\mathbf{x_{n2}}$ in (5.14) is known, other unknowns can be found by solving,

$$\mathbf{A_{n11}}\ \mathbf{x_{n1}} = \mathbf{b_{n1}} - \mathbf{A_{n12}}\ \mathbf{x_{n2}} \tag{5.15}$$

In (5.15), $\mathbf{A_{n11}}$ is needed to be re-factorized only following a discontinuity if the network model does not contain a time dependent component and/or a nonlinear network component that requires network iterative solution. By factoring $\mathbf{A_{n11}}$ (see (5.11)) and after some algebraic manipulations, (5.14) can be rewritten as

$$\begin{bmatrix} \mathbf{U} & \mathbf{L^{-1}}\ \mathbf{P_R}\ \mathbf{A_{n12}} \\ \mathbf{A_{n21}}\ \mathbf{P_C} & \mathbf{A_{n22}} \end{bmatrix} \begin{bmatrix} \mathbf{y_{n1}} \\ \mathbf{x_{n2}} \end{bmatrix} = \begin{bmatrix} \mathbf{L^{-1}}\ \mathbf{P_R}\ \mathbf{b_{n1}} \\ \mathbf{b_{n2}} \end{bmatrix} \tag{5.16}$$

where

$$\mathbf{y_{n1}} = \mathbf{P_C}^T\ \mathbf{x_{n1}} \tag{5.17}$$

$\mathbf{L^{-1}}$ in (5.16) can be obtained by Gaussian elimination. Let $\mathbf{K}$ be a matrix satisfying the equation

$$\mathbf{K}\ \mathbf{U} = -\mathbf{A}_{\mathbf{n21}}\ \mathbf{P}_{\mathbf{C}} \tag{5.18}$$

The matrix $\mathbf{K}$ can be found by eliminating the terms in $\mathbf{A}_{\mathbf{n21}}\ \mathbf{P}_{\mathbf{C}}$ using the upper triangular matrix $\mathbf{U}$. It should be noted that, in the proposed MANA formulations, $\mathbf{U}$ will not contain necessary pivots for the elimination of the terms in $\mathbf{A}_{\mathbf{n21}}\ \mathbf{P}_{\mathbf{C}}$ unless the admittance matrix $\mathbf{Y}_{\mathbf{n}}$ contains shunt branches at the nodes where the machines are connected. This problem can be avoided by modeling machine stray capacitances or adding high value grounding resistances to these nodes. Using (5.16) and (5.18), the equation system for $\mathbf{x}_{\mathbf{n2}}$ can be found as

$$\mathbf{A}'_{\mathbf{n22}}\ \mathbf{x}_{\mathbf{n2}} = \mathbf{b}'_{\mathbf{n2}} \tag{5.19}$$

where

$$\mathbf{A}'_{\mathbf{n22}} = \mathbf{A}_{\mathbf{n22}} + \mathbf{K}\ \mathbf{L}^{-1}\mathbf{P}_{\mathbf{R}}\ \mathbf{A}_{\mathbf{n12}} \tag{5.20}$$

$$\mathbf{b}'_{\mathbf{n2}} = \mathbf{b}_{\mathbf{n2}} + \mathbf{K}\ \mathbf{L}^{-1}\mathbf{P}_{\mathbf{R}}\ \mathbf{b}_{\mathbf{n1}} \tag{5.21}$$

The matrix $\mathbf{A}'_{\mathbf{n22}}$ is needed to be updated and re-factorized at each time-step to solve (5.19) for $\mathbf{x}_{\mathbf{n2}}$. $\mathbf{x}_{\mathbf{n1}}$ can be found using (5.15) after solving (5.19) for $\mathbf{x}_{\mathbf{n2}}$. As $\mathbf{A}'_{\mathbf{n22}}$ is re-factorized instead of $\mathbf{A}_{\mathbf{n}}$ at each time step, a significant improvement is expected in simulation speed. When the KLU matrix-solve package is utilized, (5.18), (5.20) and (5.21) become

$$\mathbf{K}\ \left(\mathbf{U} + \mathbf{L}^{-1}\mathbf{F}\right) = -\mathbf{A}_{\mathbf{n21}}\ \mathbf{P}_{\mathbf{C}} \tag{5.22}$$

$$\mathbf{A}'_{\mathbf{n22}} = \mathbf{A}_{\mathbf{n22}} + \mathbf{K}\ \mathbf{L}^{-1}\mathbf{R}^{-1}\mathbf{P}_{\mathbf{R}}\ \mathbf{A}_{\mathbf{n12}} \tag{5.23}$$

$$\mathbf{b}'_{\mathbf{n2}} = \mathbf{b}_{\mathbf{n2}} + \mathbf{K}\ \mathbf{R}^{-1}\mathbf{L}^{-1}\mathbf{P}_{\mathbf{R}}\ \mathbf{b}_{\mathbf{n1}} \tag{5.24}$$

5.4. MatEMTP Simulations

The subsynchronous resonance case SSR-C2 presented in Section 4.3 is simulated for numerical efficiency evaluation. The only difference is that MatEMTP simulations do not include the machine controls (excitation control and governor). The simulation codes, utilized machine models, sparse matrix solvers, MANA refactorization schemes are presented in Table 5.1. It should be noted that, MatEMTP and EMTP-RV give identical results. In addition, as expected, MANA formulation has no influence on simulation accuracy. As the accuracy assessment has been already performed in CHAPTER 4, only the CPU timings are presented for each simulation for $\Delta t = 100\mu s$.

As explained in Section 1.3, total simulation time (t_{sim}) of MatEMTP is decomposed into five parts: the CPU time for steady state solution, system component initialization and preparation for time-domain simulation (t_{ss}), the CPU time for updating $\mathbf{A_n}$ and $\mathbf{b_n}$ in (1.3) ($t_{update-A\&b}$), the CPU time for refactoring MNE coefficient matrix (1.3) ($t_{refactor-MNE}$), the CPU time for solving the factorized version of (1.3) ($t_{solve-MNE}$) and the CPU time for updating network equivalents of each system component for MNE solution and solving their equations following MNE solution (t_{comp}). The expected total CPU time (t_{sim}) of EMTP-RV in relation to various sparse matrix solvers, partial refactorization scheme for PD and VBR models, and the proposed MANA formulations are determined using the percentage changes in $t_{update-A\&b}$, $t_{refactor-MNE}$, $t_{solve-MNE}$ and t_{comp} of MatEMTP simulations. t_{ss}, $t_{update-A\&b}$, $t_{refactor-MNE}$, $t_{solve-MNE}$ and t_{comp} of EMTP-RV simulations for PD-dq0, PD and VBR models are presented in Table 5.2. The EMTP-RV model also includes the machine controls and the related CPU time is shown in Table 5.2 as t_{cont}. It should be noted that EMTP-RV uses classical MANA formulation, LU factorization with Multiple Minimum Degree (MMD) ordering, and a complete refactorization scheme for PD and VBR models. As the MNE coefficient matrix is constant for PD-dq0 and refactorization is

required only following a discontinuity, $t_{refactor-MNE}$ is negligible for the simulated case and is not presented in Table 5.2 and also the following tables.

Table 5.1 Simulation Codes, Utilized Machine Models, Sparse Matrix Solvers, MANA Refactorization Schemes

Simulation Code	MANA Formulation	Machine Model	Refactorization Scheme	Sparse Matrix Solver
S1	Classical	PD-dq0	-	LU with COLAMD
S2	Classical	PD-dq0	-	LU with AMD
S3	Classical	PD-dq0	-	KLU
S4	Classical	VBR	Complete	LU with COLAMD
S5	Classical	VBR	Complete	LU with AMD
S6	Classical	VBR	Complete	KLU
S7	Classical	PD	Complete	KLU
S8	Classical	VBR	Partial	LU with COLAMD
S9	Classical	VBR	Partial	LU with AMD
S10	Classical	VBR	Partial	KLU
S11	Classical	PD	Partial	KLU
S12	MNA-Thevenin	PD-dq0	-	KLU
S13	MNA-Thevenin	VBR	Partial	KLU
S14	MNA-Thevenin	PD	Partial	KLU
S15	MNA-Complete	VBR	Partial	KLU
S16	MNA-Complete	PD	Partial	KLU

Table 5.2 Detailed CPU Timings in EMTP-RV Simulation

	PD-dq0	PD	VBR
t_{ss}	0.121 s	0.121 s	0.121 s
$t_{update-A\&b}$	0.289 s	0.313 s	0.313 s
$t_{refactor-MNE}$	-	4.002 s	4.002 s
$t_{solve-MNE}$	1.281 s	1.281 s	1.281 s
t_{comp}	1.628 s	1.811 s	1.558 s
t_{cont}	0.959 s	0.959 s	0.959 s
t_{sim}	**4.278 s**	**8.487 s**	**8.234 s**

The timings t_{ss}, $t_{update-A\&b}$, $t_{refactor-MNE}$, $t_{solve-MNE}$ and t_{comp} of MatEMTP simulations are shown in Table 5.3. The $t_{solve-MNE}$ of MatEMTP simulations for S1 - S3 demonstrates the impact of the sparse matrix solver on solution speed of the MNE for

the PD-dq0 model usage. The performance difference between AMD and COLAMD is due to fill-in during factorization. Using AMD instead of COLAMD reduces fill-in as illustrated in Table 5.4, i.e. provides sparser **U** and **L** matrices. As a result, AMD provides better solution speed for (5.10) as compared to COLAMD.

Table 5.3 Detailed CPU Timings in MatEMTP Simulations

Simulation Code	t_{ss} (s)	$t_{update-A\&b}$ (s)	$t_{refactor-MNE}$ (s)	$t_{solve-MNE}$ (s)	t_{comp} (s)	t_{sim} (s)
S1	0.178	11.621	-	2.390	45.198	59.387
S2	0.178	11.621	-	2.072	45.198	59.069
S3	0.178	11.621	-	0.281	45.198	57.278
S4	0.178	12.279	4.652	2.390	43.842	63.347
S5	0.178	12.279	4.110	2.072	43.842	62.481
S6	0.178	12.279	3.211	0.281	43.842	59.791
S7	0.178	12.279	3.211	0.281	51.978	67.927
S8	0.178	12.279	1.889	2.145	43.842	60.333
S9	0.178	12.279	1.664	2.126	43.842	60.089
S10	0.178	12.279	1.521	0.715	43.842	58.535
S11	0.178	12.279	1.521	0.715	51.978	66.671
S12	0.178	12.279	0	0.290	43.681	55.770
S13	0.178	12.279	1.623	0.746	40.173	54.999
S14	0.178	12.279	1.623	0.746	48.309	63.135
S15	0.178	13.014	2.021	0.812	30.251	46.276
S16	0.178	12.718	1.891	0.788	38.877	54.452

As explained above, in KLU, first the block triangular form of the MNE coefficient matrix is obtained with BTF before ordering and factorization. The block triangular form coefficient matrix of the simulated system has 28 blocks and the size of the largest block is 69. The MNE coefficient matrix and its block triangular form are illustrated in Figure 5.1 and Figure 5.2, respectively. Each independent diagonal block is factorized after ordering with AMD and the solution is obtained using block-back substitution. This block-back substitution process takes significantly less time compared to the back substitution process in LU factorization with AMD or COLAMD. As a result, KLU usage provides 86.4% and 88.2% decrease in $t_{solve-MNE}$ compared to LU factorization with AMD and COLAMD, respectively.

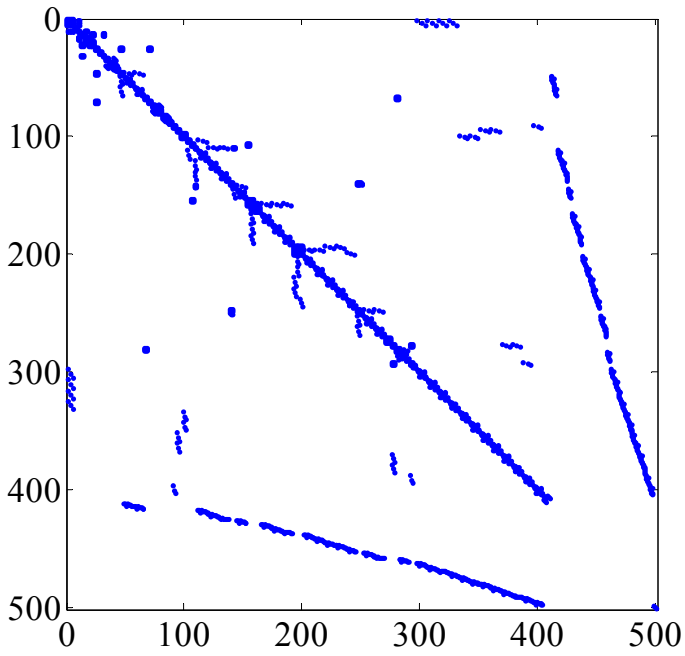

Figure 5.1 MNE coefficient matrix (number of non-zeros = 2187)

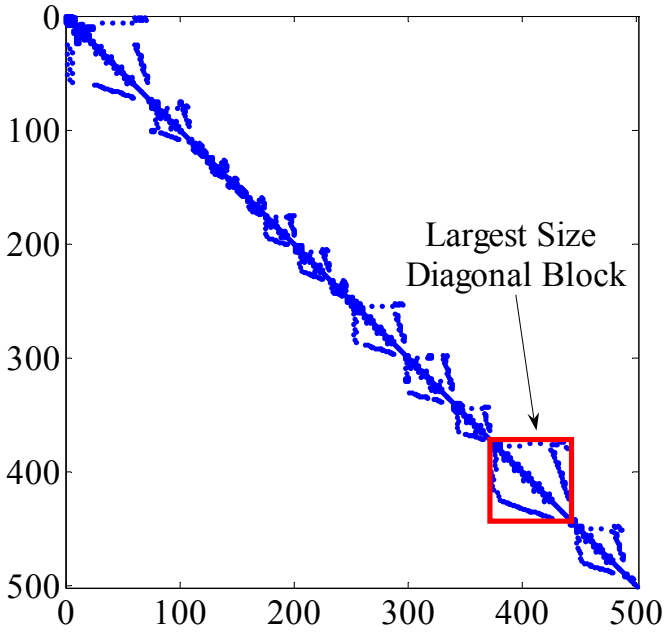

Figure 5.2 Block triangular form of MNE coefficient matrix (number of non-zeros = 2187)

Table 5.4 Ordering Quality Comparison

Fill in COLAMD	Fill in AMD	Fill in BTF+AMD
4094	3868	3855

It should be noted that AMD and MMD find similar ordering quality [33]. By considering 86.4% decrease in $t_{solve-MNE}$ of MatEMTP, t_{sim} of EMTP-RV is expected to reduce to 3.171 s from 4.278 s (i.e. 25.9% decrease in t_{sim}) with KLU sparse matrix usage instead of LU factorization with MMD.

Unlike the PD-dq0 model, both VBR and PD models use time varying machine admittance matrices; hence the MNE coefficient matrix needs to be refactorized at each solution time point. This causes a significant increase in MNE solution time (see $t_{refactor-MNE}$ in Table 5.2 and Table 5.3). As shown in Table 5.3, LU factorization with AMD is slightly faster compared to LU factorization with COLAMD due to better quality ordering. On the other hand KLU is the most efficient as the small size independent diagonal blocks are refactorized. In the simulated case, KLU provides 21.8% and 31.0% decrease in $t_{refactor-MNE}$ compared to LU factorization with AMD and COLAMD, respectively. As KLU is also fastest during the back substitution process, it provides 43.5% and 50.4% in total MNE solution time ($t_{refactor-MNE} + t_{solve-MNE}$) compared to LU factorization with AMD and COLAMD, respectively.

By considering the $t_{refactor-MNE}$ and $t_{solve-MNE}$ of MatEMTP simulations in Table 5.3, the decrease in t_{sim} of EMTP-RV simulations with KLU usage instead of LU factorization with MMD can be expected to be about 24.1% and 23.4% for VBR and PD respectively. KLU usage instead of LU factorization with MMD provides better improvement in total MNE solution time ($t_{refactor-MNE} + t_{solve-MNE}$) for PD-dq0 model compared to both PD and VBR. However, the expected improvement in simulation speed of EMTP-RV due to KLU usage is similar for all models as illustrated in Table

5.5. It should be noted that, further improvement can be achieved for all models with parallelism in KLU.

Table 5.5 Expected CPU Timings in EMTP-RV Simulation with KLU usage (based on MatEMTP simulations)

	PD-dq0	**VBR**	**PD**
$t_{refactor-MNE}$	-	3.127	3.127
$t_{solve-MNE}$	0.174	0.174	0.174
t_{sim}	**3.171**	**6.251**	**6.504**

In the partial refactorization case (see S7 - S11 in Table 5.3) $t_{refactor-MNE}$ is now the CPU time for refactoring the matrix $\mathbf{A'_{n22}}$ in (5.19), and $t_{solve-MNE}$ is the CPU time for solving the factorized versions of both (5.15) and (5.19). Refactoring $\mathbf{A'_{n22}}$ (Figure 5.3) instead of $\mathbf{A_n}$ (Figure 5.1) at each time step, provides significant improvement in $t_{refactor-MNE}$, consequently in the total MNE solution time ($t_{refactor-MNE} + t_{solve-MNE}$) for all sparse matrix solvers, as expected. By considering the $t_{refactor-MNE}$ and $t_{solve-MNE}$ of MatEMTP simulations in Table 5.3, t_{sim} of EMTP-RV is expected to decrease by 27.7% for VBR and 28.5% for PD with partial refactorization implementation. KLU usage with partial refactorization is expected to improve the simulation speed further. The expected CPU timing with partial refactorization implementation is summarized in Table 5.6 for both LU factorization with MMD and KLU usage as sparse matrix solver. As shown in Table 5.6 the computational performances of both VBR and PD models are not expected to become comparable with PD-dq0 in EMTP-RV even with partial factorization implementation.

Table 5.6 Expected CPU Timings in EMTP-RV Simulation with Partial Refactorization Scheme (based on MatEMTP simulations)

	LU with MMD			**KLU**		
	PD-dq0	**VBR**	**PD**	**PD-dq0**	**VBR**	**PD**
$t_{refactor-MNE}$	-	1.620	1.620	-	1.481	1.481
$t_{solve-MNE}$	1.281	1.314	1.314	0.174	0.461	0.461
t_{sim}	**4.278 s**	**5.885**	**6.138**	**3.171**	**4.874**	**5.127**

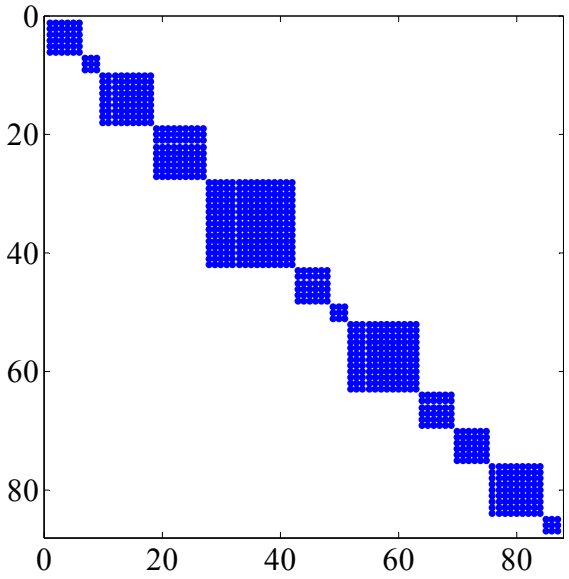

Figure 5.3 Continuously refactorized matrix in partial refactorization scheme ($\mathbf{A'_{n22}}$, number of non-zeros = 783)

The proposed MANA formulations improve t_{comp} at the expense of an increase in $t_{solve-MNE}$ and $t_{refactor-MNE}$ as shown in Table 5.3. The proposed MANA-Thevenin formulation eliminates Norton equivalent calculation from the Thevenin equivalent of the machine for the MNE solution and also the machine stator current calculations following the MNE solution at each solution time point. As VBR and PD have time-varying Thevenin resistance matrices, the improvement in t_{comp} is more noticeable when compared to PD-dq0. By considering the percentage changes in t_{comp}, $t_{refactor-MNE}$ and $t_{solve-MNE}$ of MatEMTP simulations in Table 5.3, the expected CPU timings for EMTP-RV with partial refactorization scheme, KLU and MANA-Thevenin formulation usage are found as presented in Table 5.7. Unlike MatEMTP results, it can be seen from Table 5.6 and Table 5.7, that the expected improvement in simulation speed of EMTP-RV by using MANA-Thevenin formulation is negligible. On the other hand, in MANA-Thevenin formulation, only the sub-matrix $\mathbf{A_{SM}}$ contains the time varying terms and it is located at the right bottom corner of $\mathbf{A_n}$ (see (5.2)). Therefore, partial refactorization

implementation is easier for the proposed MANA-Thevenin formulation compared to the classical MANA formulation.

Table 5.7 Expected CPU Timings in EMTP-RV Simulation with partial refactorization scheme, KLU and MNA-Thevenin usage (based on MatEMTP simulations)

	PD-dq0	VBR	PD
t_{comp}	1.573 s	1.428 s	1.683 s
$t_{refactor-MNE}$	-	1.580 s	1.580 s
$t_{solve-MNE}$	0.179 s	0.461 s	0.461 s
t_{sim}	**3.122 s**	**4.862 s**	**5.118 s**

The proposed MANA-Complete formulation eliminates the calculations to form the machine interfacing circuit for MNE and the calculations to find machine electrical variables following MNE solution. However, both the size and the number of time varying terms in the MNE coefficient matrix increase. Hence, t_{comp} is improved at the expense of an increase in $t_{update-A\&b}$, $t_{solve-MNE}$ and $t_{refactor-MNE}$. Although this formulation provides a significant improvement in total simulation time of MatEMTP (see Table 5.3), it may even reduce simulation efficiency when transposed into EMTP-RV as illustrated in Table 5.8.

Table 5.8 Expected CPU Timings in EMTP-RV Simulation with partial refactorization scheme, KLU and MNA-Complete usage (based on MatEMTP simulations)

	VBR	PD
$t_{update-A\&b}$	0.324 s	0.324 s
$t_{refactor-MNE}$	1.968 s	1.841 s
$t_{solve-MNE}$	0.502 s	0.487 s
t_{comp}	1.075 s	1.355 s
t_{sim}	**4.957 s**	**5.087 s**

CHAPTER 6.

CONCLUSIONS

In this thesis, new discrete time models, solution procedures and MANA formulations are developed for the simulation of synchronous machines in an EMT-type program. The proposed modeling approaches and solution procedures are compared for practical cases and conditions. The numerical efficiency assessment studies account for sparse matrix solvers and refactorization.

In CHAPTER 3, four new models, dq0 model with internal intermediate time step usage (dq0-ITTS), combination of dq0 model with VBR model (dq+VBR), combination of dq0 model with PD model (dq+PD) and dq0 model derived from discrete-time PD model (PD-dq0) are proposed to improve the precision of the classical dq0 model while maintaining its efficiency. In dq0-ITTS, dq+VBR, dq+PD models, the classical dq0 model is used with a more accurate solution algorithm or model, i.e. internal intermediate time step usage in dq0 model, VBR model and PD model, respectively. In order to maintain efficiency, the accurate solution algorithm or model usage is restricted to the transient intervals where the precision of dq0 decreases. The combination is achieved by implementing a network switching detection and machine terminal voltage monitoring algorithm for the startup of the transient interval and a field current monitoring algorithm for the decision process of moving back to classical dq0. These models are convenient for typical transient stability cases where accurate model usage is needed for a small portion of the complete simulation interval.

The proposed PD-dq0 model is obtained by applying Park's transformation to the discretized equations of the PD model. This idea emanates from the discretized PD model and consequently provides similar accuracy. As for the classical dq0 model, PD-dq0 uses a prediction-correction scheme for interfacing with the MNE through a constant admittance matrix for computational efficiency. In short, this model inherits

precision and performance from the PD and dq0 models, respectively. It is the best model in the generic sense.

In CHAPTER 4, performances of the proposed models are compared with the existing machine models in literature. The proposed models provide comparable accuracy with PD and VBR models for all cases. In addition, they also provide comparable simulation speed with the classical dq0. However, the numerical efficiencies of dq+VBR and dq+PD models deteriorate in the SSR case as the accurate model part usage is needed for a large portion of the complete simulation interval. Unlike dq+VBR and dq+PD models, the decrease in dq0-ITTS model efficiency is less noticeable due to the simulated system size. As the electromagnetic transients are local by nature, they limit the number of machines with intermediate time point solutions in the SSR case. However, as for dq+VBR and dq+PD models, the numerical efficiency of the dq0-ITTS model is expected to deteriorate when all machines in the system are closely coupled. On the other hand, the proposed PD-dq0 model provides PD model like accuracy while maintaining classical dq0 model like speed in all cases. Therefore, it is superior over the proposed dq0-ITTS, dq+VBR and dq+PD models in addition to the existing models in literature including PD and VBR.

It should be noted that, the PD-dq0 model inherits damping resistances for correcting numerical stability in some cases with large time step usage. However, the error due to damping resistances is less noticeable at large time steps due to reduced overall accuracy and the PD-dq0 model with damping resistances still offers the same accuracy as the competing PD and VBR models.

Despite its accuracy, the PD-dq0 model remains very efficient when compared to the PD and VBR models. In EMTP-RV simulations, PD-dq0 model usage instead of PD or VBR models increases the simulation speed more than twice due to constant MNE coefficient matrix usage.

In CHAPTER 5, partial refactorization implementation is demonstrated for various sparse matrix solvers and tested for the SSR case including 30 synchronous machines using MatEMTP. The CPU timings of MatEMTP simulations are correlated with CPU timings of EMTP-RV in order to investigate the effects of selected sparse matrix solvers and refactorization schemes on simulation efficiency in addition to machine models. Simulation results show that, the total simulation time of EMTP-RV is expected to reduce by 28.5% for VBR and 27.7% for PD model with partial refactorization scheme. However, even with partial refactorization, the simulation efficiency is still very poor with PD or VBR when compared to the proposed PD-dq0 model.

The effect of the sparse matrix solver on simulation efficiency strongly depends on the machine model, as expected. The simulation results shows that the KLU sparse matrix solver usage in EMTP-RV instead of LU factorization with MMD is expected to reduce the total simulation time by 25.9% for PD-dq0 and 16.5% for PD and 17.2% VBR models with partial refactorization scheme. As a result the computational difference between PD-dq0 and PD (or VBR) models is expected to become more significant.

CHAPTER 5 also presents two new machine representations in MANA formulation. In the first formulation, the Thevenin equivalents of the machines are inserted into the MNE to eliminate Norton equivalent calculation from machine Thevenin equivalent and stator current calculation following the MNE solution. In the second formulation, all machine equations are inserted into the MNE to eliminate interfacing circuitry and machine electrical variable calculation following MNE solution. As the second formulation introduces time dependent terms in the MNE coefficient matrix for both classical dq0 and PD-dq0 models, it is developed only for the PD and VBR machine models. These formulations are tested in MatEMTP with the KLU sparse matrix solver and a partial refactorization scheme for PD and VBR models. The expected improvement in the simulation speed of EMTP-RV is negligible for the first formulation. In addition the simulation speed of EMTP-RV is expected to reduce

with the second formulation. However, both formulations demonstrate the modeling flexibility of MANA.

As a conclusion, this thesis contributes to the establishment of more efficient and more precise synchronous machine modeling approaches and solution algorithms. Numerical integration time step size is a key factor in both aspects. The capability to use larger time steps in EMT-type simulation methods also contributes to the extension of such methods into the efficient simulation of electromechanical transients. This thesis also contributes to better assessment of both numerical precision and efficiency for researched machine models in this thesis and in recent literature.

This study can be extended for asynchronous and permanent magnet synchronous machines. Future research can also target parallelizing synchronous machine equation solutions and parallelism for the KLU sparse matrix solver in EMT-type programs.

.

REFERENCES

[1] J. Mahseredjian, J. L. Naredo, U. Karaagac, J. A. Martinez–Velasco: "Off-line Simulation Methods and Tools for Electromagnetic Transients in Power Systems: Overview and Challenges", IEEE/PES Tutorial on Electromagnetic Transients in Power Systems. IEEE Catalog Nr. 11TP255E, ISBN 978-1-4577-1501-3, July 2010.

[2] J. Mahseredjian, V. Dinavahi and J.A. Martinez "Simulation Tools for Electromagnetic Transients in Power Systems: Overview and Challenges", IEEE Transactions on Power Delivery, Vol. 24, Issue 3, pp. 1657-1669, July 2009.

[3] DCG-EMTP (Development coordination group of EMTP) Version EMTP-RV 2.1, Electromagnetic Transients Program. Available: http://www.emtp.com.

[4] Electromagnetic Transient Programs (EMTP96) Rule Book I, EMTP Development Coordination Group (DCG) and Electric Power Research Institute (EPRI), Inc., 1999.

[5] Alternative Transients Programs, ATP-EMTP, ATP User Group, 2007. Available: http://www.emtp.org.

[6] EMTDC User's Guide. Winnipeg, MB, Canada: Manitoba HVDC Research Center Inc., 2004.

[7] http://www.mathworks.com.

[8] C.W. Ho, A.E. Ruehli and P.A. Brennan, "The modified nodal approach to network analysis", Proceedings of the International Symposium on Circuits and Systems, San Francisco, April (1974), pp. 505–509.

[9] J. Mahseredjian and F. Alvarado, "Creating an Electromagnetic Transients Program in MATLAB: MatEMTP", IEEE Transactions on Power Delivery, January 1997, Vol. 12, Issue 1, pages 380-388.

[10] J. Mahseredjian, S. Dennetière, L. Dubé, B. Khodabakhchian and L. Gérin-Lajoie: "On a new approach for the simulation of transients in power systems". Electric Power Systems Research, Volume 77, Issue 11, September 2007, pp. 1514-1520.

[11] J. Mahseredjian: “Simulation des transitoires électromagnétiques dans les réseaux électriques”, Édition ‘Les Techniques de l'Ingénieur’, February 10, 2008, Dossier D4130. 2008, 12 pages.

[12] T. A. Davis, Direct Methods for Sparse Linear Systems, Philadelphia: SIAM, 2006.

[13] L. Wang, J. Jatskevich, V. Dinavahi, H. W. Dommel, J. A. Martinez, K. Strunz, M. Rioual, G. W. Chang, and R. Iravani, “Methods of Interfacing Rotating Machine Models in Transient Simulation Programs,” IEEE Transactions on Power Delivery, Vol. 25, Issue 2, pp. 891-903, April 2010.

[14] R. H. Park, “Two-reaction theory of synchronous machines-generalized method of analysis”, AIEE Trans., vol. 48, pp. 716–727, July 1929.

[15] V. Brandwajn, “Synchronous Generator Models for the Simulation of Electromagnetic Transients.”, Ph. D. Thesis, Univ. of British Columbia (Vancouver, B.C., Canada), 121 pages, April 1977.

[16] H. K. Lauw and W. S. Meyer, “Universal machine modeling for the representation of rotating electrical machinery in an electromagnetic transients program,” IEEE Trans. Power App. Syst., vol. PAS-101, pp. 1342–1351, 1982.

[17] J. Mahseredjian, S. Lefebvre and X. D. Do: “A new method for time-domain modelling of nonlinear circuits in large linear networks”. 11th Power Systems Computation Conference (PSCC), Proceedings Vol. 2, August 1993, pp. 915-922.

[18] A. M. Gole, R. W. Menzies, D. A. Woodford, and H. Turanli, “Improved interfacing of electrical machine models in electromagnetic transient programs,” IEEE Trans. Power App. Syst., vol. PAS-103, no.9, pp. 2446–2451, Sep. 1984.

[19] S. Dennetière and J. Mahseredjian, “Synchronous machine device”, *EMTP-RV documentation*, February 2005.

[20] H. W. Dommel, Electromagnetic Transients Program Reference Manual (EMTP Theory Book), Portland, Oregon, 1986.

[21] U. Karaagac, J. Mahseredjian, O. Saad and S. Dennetière, "Synchronous machine modeling precision and efficiency in electromagnetic transients", IEEE Transactions on Power Delivery, Vol. 26, Issue 2, pp. 1072-1082, April 2011.

[22] P. Subramaniam and O. P. Malik, "Digital simulation of a synchronous generator in the direct-phase quantities," Proc. Inst. Elect. Eng., vol 118, no. 1, pp. 153–160, Jan. 1971.

[23] J. R. Marti and K. W. Louie, "A phase-domain synchronous generator model including saturation effects," IEEE Trans. Power Syst., vol. 12, no. 1, pp. 222–229, Feb. 1997.

[24] X. Cao, A. Kurita, H. Mitsuma, Y. Tada, and H. Okamoto, "Improvements of numerical stability of electromagnetic transient simulation by use of phase-domain synchronous machine models," Elect. Eng. Japan., vol. 128, no. 3, pp. 53–62, Apr. 1999.

[25] A. B. Dehkordi, A. M. Gole, and T. L. Maguire, "Permanent magnet synchronous machine model for real-time simulation," in Proc. International Conf. Power Systems Transients, Montreal, QC, Canada, Jun.2005.

[26] L. Wang and J. Jatskevich, "A voltage-behind-reactance synchronous machine model for the EMTP-type solution," IEEE Trans. Power Syst., vol. 21, no. 4, pp. 1539–1549, Nov. 2006.

[27] L. Wang, J. Jatskevich, and H. W. Dommel, "Re-examination of synchronous machine modeling techniques for electromagnetic transient simulations," IEEE Trans. Power Syst., vol. 22, no. 3, pp. 516–527, Aug.2007.

[28] New S.M. Model from Tokyo Electric. Available: http://www.jaug.jp/~atp/index-e.htm.

[29] S. D. Pekarek, O. Wasynczuk, and H. J. Hegner, "An efficient and accurate model for the simulation and analysis of synchronous machine/converter systems," IEEE Trans. Energy Conversion, vol. 13, no.1, pp. 42–48, Mar. 1998.

[30] W. Gautchi, *Numerical Analysis: An Introduction*. Boston, MA: Birkhauser, 1997.

[31] T. A. Davis , J. R. Gilbert , S. I. Larimore , E. G. Ng, "A column approximate minimum degree ordering algorithm", ACM Transactions on Mathematical Software, no.3, pp. 353-376, Sep. 2004.

[32] T. A. Davis , J. R. Gilbert , S. I. Larimore , E. G. Ng, "Algorithm 836: COLAMD, a column approximate minimum degree ordering algorithm," ACM Transactions on Mathematical Software, vol. 30, no.3, pp. 377-380, Sep. 2004.

[33] P. R. Amestoy, T. A. Davis, and I. S. Du, "An approximate minimum degree ordering algorithm," SIAM J. Matrix Anal. Applic., vol. 17, no. 4, pp. 886-905, 1996.

[34] P.R. Amestoy, T.A. Davis, and I.S. Du_, "Algorithm 837: AMD, an approximate minimum degree ordering algorithm," ACM Transactions on Mathematical Software, vol.30 no. 3 pp. 381-388, 2004.

[35] Natarajan, "KLU A high performance sparse linear solver for circuit simulation problems," Master's Thesis, University of Florida, 2005.

[36] U. Karaagac, J. Mahseredjian and J. A. Martinez-Velasco: "Synchronous machines", CRC Press, Taylor & Francis Group, Chapter for Book "Power System Transients: Parameter Determination", Chapter 5, 103 pages, October 2009.

[37] M.R. Harris, P.J. Lawrenson, and J.M. Stephenson, *Per-Unit Systems with Special Reference to Electric Machines*, IEE Monograph, Cambridge University Press, 1970.

[38] U. Karaagac, J. Mahseredjian and O. Saad, "An efficient synchronous machine model for electromagnetic transients", IEEE Transactions on Power Delivery, Vol. 26, Issue 4, pp. 2456-2465, Oct. 2011.

[39] J.R. Marti and T. O. Myers, "Phase-domain induction motor model for power system simulators," IEEE Conference Communications, Power, and Computing, vol. 2, pp. 276–282, May 1995.

[40] K. A. Corzine, B. T. Kuhn, S. D. Sudhoff, H. J. Hegner, "An improved method for incorporating magnetic saturation in the q-d synchronous machine model," IEEE Trans. Energy Conversion, vol. 13, no. 3, pp. 270–275, Sept. 1998.

[41] R.G. Ramey, A.C. Sismour, and G.C.Kung, “Important parameters in considering transient torques on turbine-generator shaft systems”, *IEEE Trans. on Power Apparatus and Systems*, vol. 99, no.1, pp. 311-317, January/February, 1980.

[42] J. Lin, J. Mahseredjian, S. Lefebre, “Improvement of Synchronous Machine Saturation Simulation in the EMTP,” *IEEE TENCON’93 Proceedings*, Vol.5, pp.127-132, 1993.

[43] J. Mahseredjian: “Simulation des transitoires électromagnétiques dans les réseaux électriques”, *Édition ‘Les Techniques de l'Ingénieur’*, February 10, 2008, Dossier D4130. 2008, 12 pages.

[44] U. Karaagac, J. Mahseredjian, S. Dennetière, “EMTP simulation of synchronous machine from standstill to synchronization”, *Proc. of IEEE Power Engineering Society General Meeting*, 26-30 July 2009, Calgary.

[45] N. Ozay, A. N. Guven, “Investigation of subsynchronous resonance risk in the 380 kV Turkish electric network,” *IEEE International Symposium on Circuits and Systems*, June 1988, Espoo.

[46] J. Gilbert and T. Peierls, “Sparse spatial pivoting in time proportional to arithmetic operations,” *SIAM Journal on Scientific and Statistical Computing*, vol. 9, no. 5, pp. 862–874, 1988.

[47] http://www.cise.ufl.edu/research/sparse/klu/current.

[48] I.M. Canay, “Extended synchronous machine model for the calculation of transient processes and stability”, *Electric Machines and Electromagnetics*, vol. 1, pp. 137-150, 1977.

[49] I.M. Canay, “Causes of discrepancies on calculation of rotor quantities and exact equivalent diagrams of the synchronous machine”, *IEEE Trans. on Power Apparatus and Systems*, vol. 88, no. 7, pp1114-1120, July 1969.

[50] http://www.energy.siemens.com.

Appendix I

Input Data Conversion

All models presented in CHAPTER 2 require the inductances and resistances of the stator and rotor circuits as parameters. The classical dq0 model parameters are called fundamental or basic parameters, and are identified as the elements of the equivalent circuits shown in Figure I.1and Figure I.2. Fundamental parameters cannot be directly determined from test/field measurements. The parameters usually provided by the manufacturer are obtained by means of standardized procedures and they need to be converted to fundamental parameters. A wide range of test methods have been proposed and used in order to obtain derived parameters that characterize the synchronous machine. Therefore, depending on the performed tests, each machine might have different type of data sets in terms of the derived parameters. This part summarizes the techniques which are used to obtain fundamental parameters from the different type of data sets. The reader should refer [36] for details.

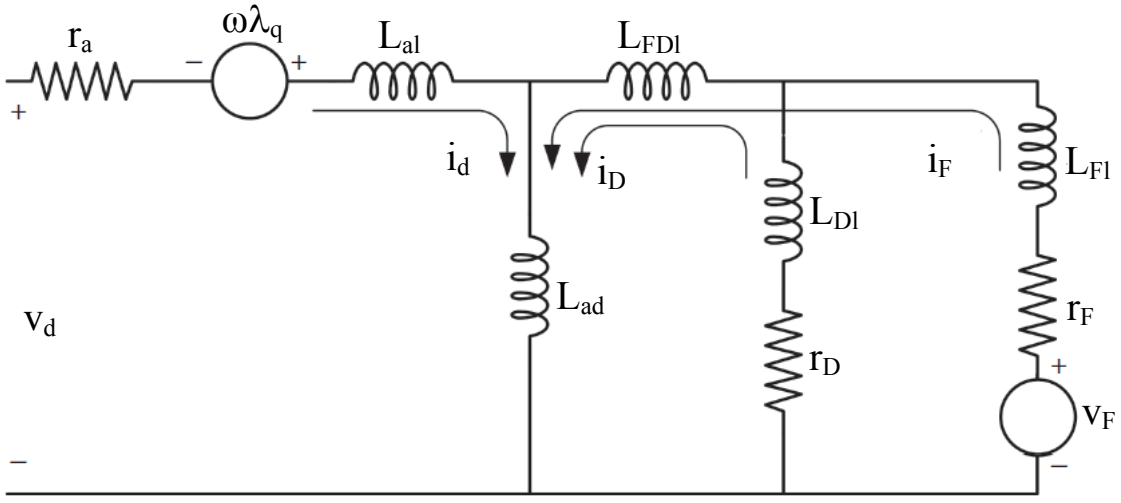

Figure I.1. *d* -axis equivalent circuit representing the complete characteristic

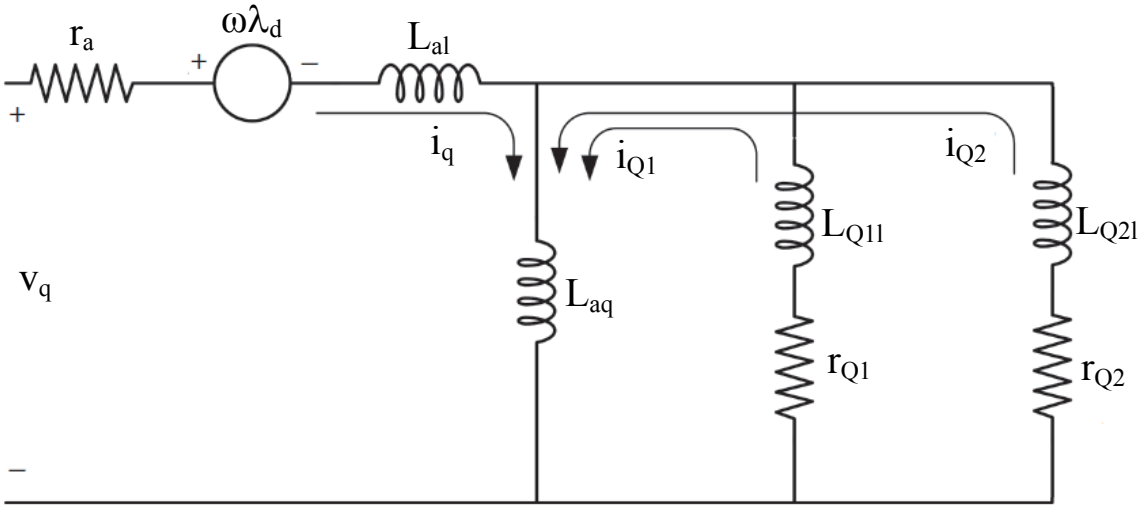

Figure I.2. q -axis equivalent circuit representing the complete characteristic

Determination of Fundamental Parameters from Operational Parameters

If a synchronous machine has been subjected to a parameter determination study based on frequency response tests, the operational parameters of synchronous machine are expected to be available in addition to leakage inductance L_{al} [36].

$$\begin{aligned} \lambda_d(s) &= G(s)\, v_F(s) + L_d(s)\, i_d(s) \\ \lambda_q(s) &= L_q(s)\, i_q(s) \end{aligned} \tag{I.1}$$

where $G(s)$ is armature to field transfer function, $L_d(s)$ and $L_q(s)$ are the d and q -axis operational inductances, respectively.

$$G(s) = \frac{L_{ad}}{r_F} \frac{\left(1 + sT_{kd}\right)}{1 + \left(T'_{do} + T''_{do}\right)s + \left(T'_{do}\, T''_{do}\right)s^2} \tag{I.2}$$

$$L_d(s) = L_d \frac{1 + \left(T'_d + T''_d\right)s + \left(T'_d\, T''_d\right)s^2}{1 + \left(T'_{do} + T''_{do}\right)s + \left(T'_{do}\, T''_{do}\right)s^2} \tag{I.3}$$

$$L_q(s) = L_q \frac{1 + \left(T'_q + T''_q\right)s + \left(T'_q\, T''_q\right)s^2}{1 + \left(T'_{qo} + T''_{qo}\right)s + \left(T'_{qo}\, T''_{qo}\right)s^2} \tag{I.4}$$

In above equations, T_d' and T_d'' are the d-axis transient and subtransient short circuit time constants, T_{d0}' and T_{d0}'' are the d-axis transient and subtransient open circuit time constants, T_q' and T_q'' are the q-axis transient and subtransient short circuit time constants, T_{q0}' and T_{q0}'' are the q-axis transient and subtransient open circuit time constants, and T_{kd} is given by

$$T_{kd} = \frac{L_{Dl}}{r_D} \tag{I.5}$$

Fundamental parameters of d-axis equivalent circuit can be found from $G(s)$ and $L_d(s)$ using the algorithm below [19], [36]:

1. Find L_{ad} using

$$L_{ad} = L_d - L_{al} \tag{I.6}$$

2. Calculate intermediate parameters:

$$R_p = \frac{L_{ad}^2}{L_d\left[\left(T_{d0}'' + T_{d0}'\right) - \left(T_d'' + T_d'\right)\right]} \tag{I.7}$$

$$a = \frac{L_d\left(T_d'' + T_d'\right) - L_{al}\left(T_{d0}'' + T_{d0}'\right)}{L_{ad}} \tag{I.8}$$

$$b = \frac{L_d\ T_d''\ T_d' - L_{al}\ T_{d0}''\ T_{d0}'}{L_{ad}} \tag{I.9}$$

$$c = \frac{T_{d0}''\ T_{d0}' - T_d''\ T_d'}{\left(T_{d0}'' + T_{d0}'\right) - \left(T_d'' + T_d'\right)} \tag{I.10}$$

3. Calculate fundamental parameters:

$$L_{Fdl} = R_p \frac{b - a\,T_{kd} + T_{kd}^2}{c - T_{kd}} \tag{I.11}$$

$$r_F = R_p \frac{L_{Fdl} + R_p\left(2T_{kd} - a\right)}{L_{Fdl} + R_p\left(T_{kd} + c - a\right)} \tag{I.12}$$

$$r_D = \frac{r_F\ R_p}{r_F - R_p} \tag{I.13}$$

$$L_{Fl} = r_F\left(a - T_{kd}\frac{L_{Fdl}}{R_p}\right) \tag{I.14}$$

$$L_{Dl} = r_D\ T_{kd} \tag{I.15}$$

When $G(s)$ is not available, it is not possible to extract the parameters of the equivalent circuit shown in Figure I.1, unless the so-called Canay's characteristic inductance is provided. In that case, only the parameters of the simplified equivalent circuit, in which L_{FDl} is omitted, can be obtained. The omission of L_{FDl} brings the assumption that all d-axis rotor circuits link a single ideal mutual flux represented by L_{ad}. Fundamental parameters of the simplified d-axis equivalent circuit can be found from $L_d(s)$ using the algorithm below [19], [36]:

1. Find L_{ad} using (I.6);
2. Calculate intermediate parameters R_p, a, b and c using (I.7), (I.8), (I.9) and (I.10), respectively;
3. Calculate fundamental parameters of the rotor windings:

$$R_{w1} = \frac{2R_p\sqrt{a^2-4b}}{a-2c+\sqrt{a^2-4b}} \tag{I.16}$$

$$L_{w1} = \frac{R_{w1}\left(a+\sqrt{a^2-4b}\right)}{2} \tag{I.17}$$

$$R_{w2} = \frac{2R_p\sqrt{a^2-4b}}{2c-a+\sqrt{a^2-4b}} \tag{I.18}$$

$$L_{w2} = \frac{R_{w2}\left(a-\sqrt{a^2-4b}\right)}{2} \tag{I.19}$$

4. Identify the field and damper windings:

   If $\left(T_{w1} = \frac{L_{ad}+L_{w1}}{R_{w1}} > T_{w2} = \frac{L_{ad}+L_{w2}}{R_{w2}}\right)$

   then $r_F = R_{w1}, L_{Fl} = L_{w1}, r_D = R_{w2}, L_{Dl} = L_{w2}$

   else $r_F = R_{w2}, L_{Fl} = L_{w2}, r_D = R_{w1}, L_{Dl} = L_{w1}$

As seen from Figure I.1 and Figure I.2, d and q-axis equivalent circuits become similar with the omission of L_{FDl}. Hence, the above algorithm can be utilized for fundamental parameters of the q-axis equivalent circuit by replacing L_d, L_{ad}, T'_d, T''_d, T'_{d0}, T''_{d0}, r_F, r_D, L_{Fl} and L_{Dl} with L_q, L_{aq}, T'_q, T''_q, T'_{q0}, T''_{q0}, r_{Q1}, r_{Q2}, L_{Q1l} and L_{Q2l}, respectively. It should be noted that for a laminated salient pole machine having one damper winding on q-axis, transient time constants (T'_q and T'_{q0}) are not defined and subtransient time constants become

$$T_q'' = \frac{1}{R_{Q1}}\left[L_{Q1Q1} - \frac{L_{aq}^2}{L_q} \right] \tag{I.20}$$

$$T_{q0}'' = \frac{L_{Q1Q1}}{R_{Q1}} \tag{I.21}$$

Determination of Fundamental Parameters with Canay's Characteristic Impedance

Leakage inductance L_{al} is usually chosen in such a way that it represents the leakage flux not crossing the air-gap. However, its choice is arbitrarily and can be chosen equal to Canay's characteristic inductance denoted by L_C which transforms the equivalent circuit given in Figure I.1 to the form illustrated in Figure I.3 [48], [49].

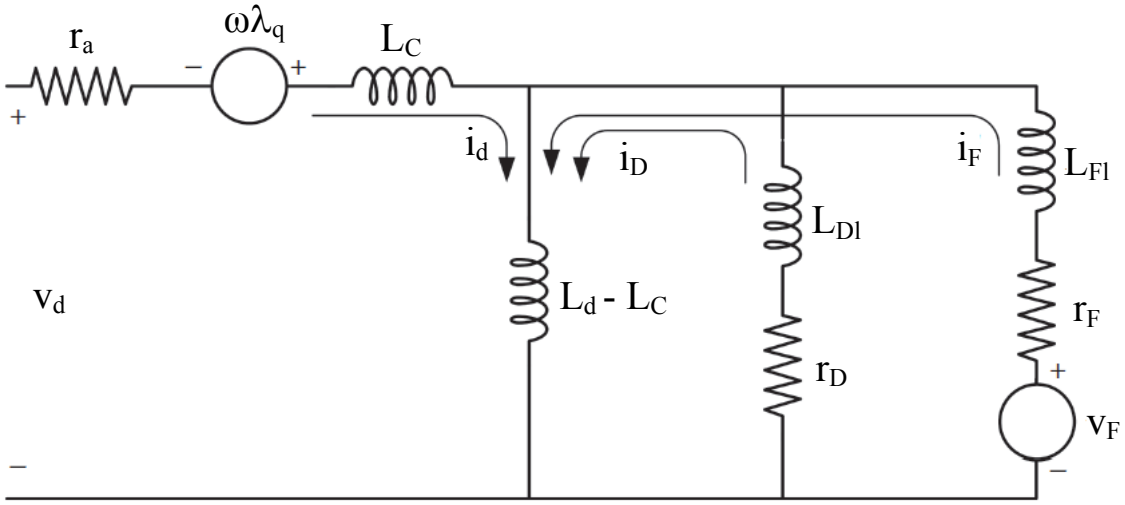

Figure I.3. d -axis equivalent circuit after transformation

Due to the new leakage inductance L_C, the real flux common to the fictitious d, field and d-axis amortisseur windings modifies. Therefore, the ratio of the number of turns changes resulting the change of real electrical quantities of the rotor referred to the stator.

The relationship between Canay's characteristic inductance and the inductance L_{FDl}, which represents the flux linking both the field and the amortisseur but not the d-axis winding, is as follows:

$$\frac{1}{L_C - L_{al}} = \frac{1}{L_{ad}} + \frac{1}{L_{FDl}} \tag{I.22}$$

In case Canay's characteristic inductance is available in addition to $L_d(s)$ and L_{al}, it is possible to find the equivalent circuit parameters illustrated in Figure I.1. The following algorithm can be utilized to find the fundamental parameters of d-axis equivalent circuit [19], [36]:

1. Find L_{ad} using (I.6);

2. Find L_{FDl} using

$$L_{FDl} = \frac{L_{ad}\left(L_C - L_{al}\right)}{L_{ad} - L_C + L_{al}} \tag{I.23}$$

3. Calculate intermediate parameters R_p, a, b and c using (I.7), (I.8), (I.9) and (I.10), respectively;

4. Calculate intermediate parameters A and B using

$$A = a - \frac{L_{FDl}}{R_p} \tag{I.24}$$

$$B = b - L_{FDl}\frac{c}{R_p} \tag{I.25}$$

5. Calculate fundamental parameters of the rotor windings:

$$R_{w1} = \frac{2R_p\sqrt{A^2-4B}}{A-2c+\sqrt{A^2-4B}} \tag{I.26}$$

$$L_{w1} = \frac{R_{w1}\left(A+\sqrt{A^2-4B}\right)}{2} \tag{I.27}$$

$$R_{w2} = \frac{2R_p\sqrt{A^2-4B}}{2c-A+\sqrt{A^2-4B}} \tag{I.28}$$

$$L_{w2} = \frac{R_{w2}\left(A-\sqrt{A^2-4B}\right)}{2} \tag{I.29}$$

6. Identify the field and damper windings:

If $\left(T_{w1} = \frac{L_{ad}+L_{FDl}+L_{w1}}{R_{w1}} > T_{w2} = \frac{L_{ad}+L_{FDl}+L_{w2}}{R_{w2}}\right)$

then $r_F = R_{w1}, L_{Fl} = L_{w1}, r_D = R_{w2}, L_{Dl} = L_{w2}$

else $r_F = R_{w2}, L_{Fl} = L_{w2}, r_D = R_{w1}, L_{Dl} = L_{w1}$

Determination of Fundamental Parameters from Transient and Subtransient Impedances and Time Constants

If a synchronous machine has been subjected to parameter determination studies other than the tests based on frequency response, data set of the machine regarding the stability studies may contain the parameters listed in Table I.1 in addition to synchronous and leakage inductances based on the standard tests [36].

As illustrated above, simplified second order d-axis model can be found from d-axis operational inductance $L_d(s)$ i.e. the d-axis open and short circuit time constants, T'_{d0}, T''_{d0}, T'_d, T''_d with L_d (see (I.3)). Moreover, if Canay's characteristic inductance is

also provided, all the parameters in the equivalent circuit representing the complete characteristic (see Figure I.1) can be found. It should be noted that, if d-axis subtransient and transient inductance of the machine, L'_d and L''_d are provided in addition to either d-axis open circuit time constants T'_{d0}, T''_{d0} or short circuit time constants T'_d, T''_d, it is possible to calculate d-axis operational inductance $L_d(s)$. Hence the data sets illustrated in Table I.2 are equivalent.

Table I.1 Transient and Subtransient Inductances and Time Constants

Transient and Subtransient Inductances	
d-axis parameters	***q-axis parameters***
L'_d	L'_q
L''_d	L''_q
Transient and Subtransient Short Circuit Time Constants	
d-axis parameters	***q-axis parameters***
T'_d	T'_q
T''_d	T''_q
Transient and Subtransient Open Circuit Time Constants	
d-axis parameters	***q-axis parameters***
T'_{d0}	T'_{q0}
T''_{d0}	T''_{q0}

Table I.2 Equivalent Data Sets

First Data Set	T'_{d0}, T''_{d0}, T'_d, T''_d
Second Data Set	L'_d, L''_d, T'_{d0}, T''_{d0}
Third Data Set	L'_d, L''_d, T'_d, T''_d

When second data set is available, T'_d, T''_d in the first data set can be obtained by finding the roots of the equation [19], [36]:

$$\frac{L_d^2}{L'_d\,L''_d}T^2+\frac{L_d}{L''_d}\left(T'_{d0}+T''_{d0}\right)T+\left(1-\frac{L_d}{L'_d}+\frac{L_d}{L''_d}\right)T'_{d0}\,T''_{d0}=0 \qquad \text{(I.30)}$$

T'_d and T''_d are the roots of (I.30) and the greater root is T'_d.

When third data set is available, T'_{d0}, T''_{d0} in the first data set can be obtained by finding the roots of the equation [19], [36]:

$$T^2 + \left(\frac{L_d}{L'_d} T'_d + \left(1 - \frac{L_d}{L'_d} + \frac{L_d}{L''_d} \right) T''_d \right) T + \frac{L_d}{L''_d} T'_d \, T''_d = 0 \qquad \text{(I.31)}$$

T'_{d0} and T''_{d0} are the roots of (I.31) and the greater root is T'_{d0}.

Per-Unit System and Calculation of Real Values

Both the derived machine parameters provided by the manufacturer and obtained fundamental parameters using the above algorithms are based on per unit values. Hence real values should be calculated for machine simulation model using the base quantities given below [19]:

$$Z_{Base-Stator} = \frac{\left(rated\ line\ to\ line\ rms\ voltage \right)^2}{rated\ VA} \qquad \text{(I.32)}$$

$$Z_{Base-Mutual} = \frac{Z_{Base-Stator}}{\left(N_F / N_d \right)} \qquad \text{(I.33)}$$

$$Z_{Base-Rotor} = \frac{Z_{Base-Stator}}{\left(N_F / N_d \right)^2} \qquad \text{(I.34)}$$

In above equations, $Z_{Base-Stator}$ is the base impedance for stator circuits, $Z_{Base-Mutual}$ is the base impedance for stator to rotor mutual inductances and $Z_{Base-Rotor}$ is the base impedance for rotor circuits. N_F / N_d is the turns ratio of field winding to d-axis fictitious winding and can be found using open circuit characteristics (OCC) of the machine.

$$N_F / N_d = \frac{\left(rated\ line\ to\ line\ rms\ voltage\right) / \left(I_{f-NL(ag)}\right)}{\left(X_d - X_{al}\right)} \qquad \text{(I.35)}$$

where $I_{f-NL(ag)}$ is the field current at base voltage on the air gap line; X_d and X_{al} are in Ω.

In the synchronous machine models presented in this thesis, the rotor structure quantities are rescaled by changing the number of turns to provide $N_F / N_d = 1$, Hence, the field voltage input v_F and rotor current output $\mathbf{i_r}$ are rescaled accordingly.

Appendix II

Linear Predictors

Due to the usage of the Backward Euler (EBA) method with $\Delta t/2$, the uniform spacing along the time axis is disturbed as illustrated in Figure 3.1. Therefore, both the two-point linear predictor given in (3.6) and the linear three-point predictor given in (3.20) should be modified depending on the solution method for the next time point and the method used for the previous solution.

Two-Point Linear Predictor

For any variable x, the utilized two-point linear predictors are as follows.

- Next time step solution is TRAP and previous solution is obtained by TRAP,

$$x(t+\Delta t) = 2\,x(t) - x(t-\Delta t) \tag{II.1}$$

- Next time step solution is TRAP and previous solution is obtained by EBA,

$$x(t+\Delta t) = 3\,x(t) - 2x(t-\Delta t/2) \tag{II.2}$$

- Next time step solution is EBA and previous solution is obtained by TRAP,

$$x(t+\Delta t/2) = \frac{3}{2}\,x(t) - \frac{1}{2}x(t-\Delta t) \tag{II.3}$$

- Next time step solution is EBA and previous solution is obtained by EBA;

$$x(t+\Delta t/2) = 2\,x(t) - x(t-\Delta t/2) \tag{II.4}$$

Three-Point Linear Predictor with smoothing

For any variable x, the utilized three-point linear predictors are as follows.

- Next time step solution is TRAP and previous two solutions are obtained by TRAP,

$$x(t+\Delta t)=\frac{5}{4}x(t)+\frac{1}{2}x(t-\Delta t)-\frac{3}{4}x(t-2\Delta t) \qquad \text{(II.5)}$$

- Next time step solution is TRAP and previous two solutions are obtained by TRAP and EBA,

$$x(t+\Delta t)=\frac{3}{2}x(t)+\frac{1}{2}x(t-\Delta t)-x(t-3\Delta t/2) \qquad \text{(II.6)}$$

- Next time step solution is TRAP and previous two solutions are obtained by EBA,

$$x(t+\Delta t)=\frac{7}{4}x(t)+\frac{1}{2}x(t-\Delta t/2)-\frac{5}{4}x(t-\Delta t) \qquad \text{(II.7)}$$

- Next time step solution is EBA and previous two solutions are obtained by TRAP,

$$x(t+\Delta t/2)=x(t)+\frac{1}{2}x(t-\Delta t)-\frac{1}{2}x(t-2\Delta t) \qquad \text{(II.8)}$$

- Next time step solution is EBA and previous two solutions are obtained by EBA and TRAP,

$$x(t+\Delta t/2)=x(t)+\frac{1}{2}x(t-\Delta t/2)-\frac{1}{2}x(t-3\Delta t/2) \qquad \text{(II.9)}$$

Appendix III

A_λ, B_I, $B_{\lambda k}$, b_{VF}, $K_\lambda(\omega)$, K_I, $K_{\lambda k}(\omega)$, $K_{p\lambda k}$ and k_{VF} in Discrete-Time VBR Machine Model

For trapezoidal integration, $\mathbf{A_\lambda}$, $\mathbf{B_I}$, $\mathbf{B_{\lambda k}}$ and $\mathbf{b_{VF}}$ are as follows:

$$\mathbf{A}_\lambda = \left(\frac{2}{\Delta t}\mathbf{I} - \mathbf{A}\right)^{-1}\left(\frac{2}{\Delta t}\mathbf{I} + \mathbf{A}\right) \tag{III.1}$$

$$\mathbf{A} = \begin{bmatrix} \frac{r_F}{L_{lF}}\left(\frac{L''_{ad}}{L_{lF}} - 1\right) & \frac{r_F}{L_{lF}}\frac{L''_{ad}}{L_{lD}} & 0 & 0 \\ \frac{r_D}{L_{lD}}\frac{L''_{ad}}{L_{lF}} & \frac{r_D}{L_{lD}}\left(\frac{L''_{ad}}{L_{lD}} - 1\right) & 0 & 0 \\ 0 & 0 & \frac{r_{Q1}}{L_{lQ1}}\left(\frac{L''_{aq}}{L_{lQ1}} - 1\right) & \frac{r_{Q1}}{L_{lQ1}}\frac{L''_{aq}}{L_{lQ2}} \\ 0 & 0 & \frac{r_{Q2}}{L_{lQ2}}\frac{L''_{aq}}{L_{lQ1}} & \frac{r_{Q2}}{L_{lQ2}}\left(\frac{L''_{aq}}{L_{lQ2}} - 1\right) \end{bmatrix} \tag{III.2}$$

$$\mathbf{B_I} = \left(\frac{2}{\Delta t}\mathbf{I} - \mathbf{A}\right)^{-1}\mathbf{B} \tag{III.3}$$

$$\mathbf{B} = \begin{bmatrix} \frac{r_F}{L_{lF}} & \frac{r_D}{L_{lD}} & 0 & 0 \\ 0 & 0 & \frac{r_{Q1}}{L_{lQ1}} & \frac{r_{Q2}}{L_{lQ2}} \end{bmatrix}^T \tag{III.4}$$

$$\mathbf{B_{\lambda k}} = \left(\frac{2}{\Delta t}\mathbf{I} - \mathbf{A}\right)^{-1}\mathbf{C} \tag{III.5}$$

$$\mathbf{C} = \begin{bmatrix} \dfrac{r_F}{L_{lF}}\dfrac{L''_{ad}}{L_{ad}} & \dfrac{r_D}{L_{lD}}\dfrac{L''_{ad}}{L_{ad}} & 0 & 0 \\ 0 & 0 & \dfrac{r_{Q1}}{L_{lQ1}}\dfrac{L''_{aq}}{L_{aq}} & \dfrac{r_{Q2}}{L_{lQ2}}\dfrac{L''_{aq}}{L_{aq}} \end{bmatrix}^T \tag{III.6}$$

$$\mathbf{b_{VF}} = \left(\frac{2}{\Delta t}\mathbf{I} - \mathbf{A}\right)^{-1}\mathbf{d} \tag{III.7}$$

$$\mathbf{d} = \begin{bmatrix} 1 & 0 & 0 & 0 \end{bmatrix}^T \tag{III.8}$$

For the Backward Euler solution with $\Delta t/2$ simulation time step, the matrix $\mathbf{A_\lambda}$ and history term $\mathbf{h_{VBR\lambda}}$ in (3.42) become:

$$\mathbf{A_\lambda} = \frac{2}{\Delta t}\left(\frac{2}{\Delta t}\mathbf{I} - \mathbf{A}\right)^{-1} \tag{III.9}$$

$$\mathbf{h_{VBR\lambda}} = \mathbf{A_\lambda}\,\hat{\boldsymbol{\lambda}}_\mathbf{r} \tag{III.10}$$

$\mathbf{K_\lambda}(\omega)$, $\mathbf{K_I}$, $\mathbf{K_{\lambda k}}(\omega)$, $\mathbf{K_{p\lambda k}}$ and $\mathbf{k_{VF}}$ are as follows:

$$\mathbf{K_\lambda}(\omega) = \begin{bmatrix} \left(\dfrac{L''_{ad}\,r_F}{L_{Fl}^2}\left(\dfrac{L''_{ad}}{L_{Fl}}-1\right)+\dfrac{L''^2_{ad}\,r_D}{L_{Dl}^2\,L_{Fl}}\right) & -\omega\dfrac{L''_{ad}}{L_{Fl}} \\ \left(\dfrac{L''^2_{ad}\,r_F}{L_{Dl}\,L_{Fl}^2}+\dfrac{L''_{ad}\,r_D}{L_{Dl}^2}\left(\dfrac{L''_{ad}}{L_{Dl}}-1\right)\right) & -\omega\dfrac{L''_{ad}}{L_{Dl}} \\ \omega\dfrac{L''_{aq}}{L_{Q1l}} & \left(\dfrac{L''_{aq}\,r_{Q1}}{L_{Q1l}^2}\left(\dfrac{L''_{aq}}{L_{Q1l}}-1\right)+\dfrac{L''^2_{aq}\,r_{Q2}}{L_{Q2l}^2\,L_{Q1l}}\right) \\ \omega\dfrac{L''_{aq}}{L_{Q2l}} & \left(\dfrac{L''^2_{aq}\,r_{Q1}}{L_{Q2l}\,L_{Q1l}^2}+\dfrac{L''_{aq}\,r_{Q2}}{L_{Q2l}^2}\left(\dfrac{L''_{aq}}{L_{Q2l}}-1\right)\right) \end{bmatrix}^T \tag{III.11}$$

$$\mathbf{K_I} = \begin{bmatrix} \left(\frac{r_F}{L_{Fl}^2} + \frac{r_D}{L_{Dl}^2}\right) L_{ad}''^2 & 0 \\ 0 & \left(\frac{r_{Q2}}{L_{Q2l}^2} + \frac{r_{Q1}}{L_{Q1l}^2}\right) L_{aq}''^2 \end{bmatrix} \tag{III.12}$$

$$\mathbf{K_{\lambda k}}(\omega) = \begin{bmatrix} \left(\frac{r_F}{L_{Fl}^2} + \frac{r_D}{L_{Dl}^2}\right) \frac{L_{ad}''^2}{L_{ad}} & \omega \frac{L_{aq}''}{L_{aq}} \\ -\omega \frac{L_{ad}''}{L_{ad}} & \left(\frac{r_{Q2}}{L_{Q2l}^2} + \frac{r_{Q1}}{L_{Q1l}^2}\right) \frac{L_{aq}''^2}{L_{aq}} \end{bmatrix} \tag{III.13}$$

$$\mathbf{K_{p\lambda k}} = \begin{bmatrix} \frac{L_{ad}''}{L_{ad}} & 0 \\ 0 & \frac{L_{aq}''}{L_{aq}} \end{bmatrix} \tag{III.14}$$

$$\mathbf{k_{VF}} = \begin{bmatrix} \frac{L_{ad}''}{L_{Fl}} & 0 \end{bmatrix}^T \tag{III.15}$$

Appendix IV

Single Machine - Infinite Bus System Data

Synchronous Machine Parameters:

382.22 MVA, 20 kV, 50 Hz, 2 poles, H = 4.15 s,

R_s = 0.002 pu, L_{al} = 0.184 pu, L_0 = 0.184 pu,

L_d = 2.03 pu, L'_d = 0.309 pu, L''_d = 0.225 pu, T'_{d0} = 7.32 s, T''_{d0} = 0.022 s,

L_q = 1.97 pu, L'_q = 0.471 pu, L''_q = 0.225 pu, T'_{q0} = 0.67 s, T''_{q0} = 0.032 s,

Table I.3 Open Circuit Saturation Data in Per Unit

Field Current	0.75	1	1.25	1.5	2	3
Armature Voltage	0.75	0.95	1.075	1.15	1.225	1.3

Excitation system parameters (in PSS/E data file format [50]):

'EXST1', TR, V_{IMAX}, V_{IMIN}, T_C, T_B, K_A, T_A, V_{RMAX}, V_{RMIN}, K_C, K_F, T_F/

'EXST1', 0.02, 999, -999, 1, 10, 200, 0.01, 4.55, -3.867, 0, 0, 1/

Turbine governor parameters (in PSS/E data file format [50]):

'IEESGO', T_1, T_2, T_3, T_4, T_5, T_6, K_1, K_2, K_3, P_{MAX}, P_{MIN}/

'IEESGO', 0, 0, 0.25, 0.1, 9, 0.5, 25, 0.75, 0.4, 0.9, 0/

Line parameters (PI-1 & PI-2):

R_1 = 0.0208946800 Ω/km, L_1 = 0.2659992400 Ω/km, C_1 = 2.64523E-06 S/km,

R_0 = 0.3029945200 Ω/km, L_0 = 0.9910027600 Ω/km, C_0 = 4.32910E-06 S/km,

Length = 144 km

Step-up Transformer:

400 MVA, 20/400 kV, 50 Hz, DYn-11

R = 0.002 pu, X = 0.15 pu.

Equivalent System Impedance (Zs):

R_1 = 1.165 Ω, L_1 = 2.225 Ω, R_0 = 2.955 Ω, L_0 = 5.385 Ω